

EXPERIMENTAL AND THEORETICAL EXPLORATIONS OF ANION PHOTOELECTRON  
SPECTROSCOPY AND PHOTOIONIZATION

By  
Sara A. Marquez

A dissertation submitted to Johns Hopkins University in conformity with the  
requirement for the degree of Doctor of Philosophy

Baltimore, Maryland  
August, 2018

© 2018 Sara A. Marquez  
All Rights Reserved

## Abstract

Negatively charged ions were investigated in the gas phase using anion photoelectron spectroscopy. These experiments were conducted using a unique time-of-flight (TOF) mass spectrometer coupled with a magnetic bottle photoelectron spectrometer (PES). The apparatus was fitted with an additional ion source, a novel electrostrpay ionization (ESI) source, leading to necessary modifications to the vacuum system, TOF spectrometer region, and the light baffles. The ESI source generates intact ions in the gas phase from nonvolatile, liquid samples. Since the ESI source is inherently continuous, it must be integrated into the pulsed environment of the TOF mass spectrometer and magnetic bottle PES. A 3D Paul trap was utilized for this purpose, which stores the ions for a variable amount of time before extraction, significantly improving the duty cycle. Mounting the ion trap to the cold head of a liquid nitrogen cooled cryostat creates cold ions resulting in better resolved photoelectron spectra due to the elimination of vibrational hot bands. Furthermore, the low energy photoionization spectrum of propyne was simulated, revealing the consequences of the Jahn-Teller effect and the spin-orbit interaction. Experimental photoionization studies reporting the spectrum of the propyne cation have been published, though there are discrepancies in the conclusions. Such discrepancies are addressed and resolved.

Research Advisor: Dr. Kit H. Bowen

Readers: Dr. John Toscano

Dr. Craig Townsend

Dedicated to my Parents

## TABLE OF CONTENTS

<b>CHAPTER 1: Introduction</b>	<b>1</b>
I. Introduction	2
II. Experimental	3
A. General Apparatus Overview	7
B. Time-of-Flight (TOF) Mass Spectrometer	7
C. Mass Gate & Momentum Decelerator	10
D. Magnetic Bottle Photoelectron Spectrometer	12
III. Theory	15
A. Nonadiabatic Interactions	17
B. Adiabatic to Diabatic Basis	19
C. Intersection Adapted Coordinates	20
D. Locating Conical Intersections	22
E. Simulating Spectra	23
F. Relativistic Contribution	28
<b>CHAPTER 2: Experimental Anion Photoelectron Spectroscopy</b>	<b>36</b>
I. Introduction	37
II. Sources	39
A. Laser Vaporization	40
B. PACIS	42
C. Electrospray Ionization Source	43
1. Cryostat	56
2. Purge Chamber	66
III. Modification to the Vacuum System	69
IV. Time-of-Flight Mass Spectrometer	75
A. Deflectors	77
B. First Einzel Lens	79
C. Second Einzel Lens	82

V. Interaction Region	87
A. Light Baffles	91
<b>CHAPTER 3: On the Photoionization Spectrum of Propyne</b>	<b>98</b>
I. Introduction	100
II. Theoretical Approach	101
A. Simulating a Photoionization Spectrum: Nonrelativistic Treatment.	102
B. Simulating a Photoionization Spectrum: Relativistic Effects, Intensity Borrowing.	106
III. Photoionization Spectrum of Propyne	108
A. Electronic Structure Calculations.	108
B. Extrema.	110
C. Jahn-Teller Parameters.	113
D. Representing the Coupled Potential Energy Surfaces.	114
E. Parameters Defining the Nonrelativistic Vibronic Wave Function for the Cation.	116
F. Photoionization Spectra.	117
IV. Summary and Conclusions	123
<b>CURRICULUM VITAE</b>	<b>133</b>

## LIST OF TABLES

<b>Table 2.1.</b> Table of base pressures and working pressures of both the ESI source side with buffer gas added and the laser vaporization source with helium in chamber 0. _____	86
<b>Table 3.1.</b> Energies in $\text{cm}^{-1}$ and Structures of Extrema for $\text{C}_3\text{H}_4$ and $\text{C}_3\text{H}_4^+$ . _____	111
<b>Table 3.2.</b> Harmonic Frequencies in $\text{cm}^{-1}$ . _____	113
<b>Table 3.3.</b> Hybrid Basis: $M = 3,2,3,2,2; 3,4,6,3,4; 3,4,6,3,4, (2,2,3,2,2; 2,3,5,2,4; 2,3,5,2,4)$ ; $N^{\text{vib}}N^{\text{state}} = 107,495,424 (5,529,600)$ ; $O_{\text{v}}(0) = 0.992042(0.992013)$ ; Reduced Basis Parameters Given Parenthetically; in $M$ , the Modes Are in the Order $(1 - 5a_1; 1 - 5e_x; 1 - 5e_y)$ ; Reported Rel-Reduced Simulation Based on $N^{\text{eig}} = 100$ ; Energies in $\text{cm}^{-1}$ . _____	118
<b>Table 3.4.</b> Neutral Basis: $M = 2,2,6,3,3; 3,4,6,3,4; 3,4,6,3,4 (2,1,4,3,3; 2,4,4,3,4; 2,4,4,3,4)$ ; $N^{\text{vib}}N^{\text{state}} = 322,486,272 (21,233,664)$ ; in $M$ the Modes Are in the Order $(1 - 5a_1; 1 - 5e_x; 1 - 5e_y)$ ; Reduced Basis Parameters Given Parenthetically; Reported Rel-Reduced Simulation Based on $N^{\text{eig}} = 100$ ; Energies in $\text{cm}^{-1}$ . _____	119

## LIST OF FIGURES

- Figure 1.1:** Photodetachment process with mass selected anions. \_\_\_\_\_ 4
- Figure 1.2:** Schematic of photoelectron spectroscopy; detachment from the anion probes the neutral ground and excited state potential energy surfaces. \_\_\_\_\_ 5
- Figure 1.3:** General schematic of PIPES apparatus before renovations and additions.  
\_\_\_\_\_ 7
- Figure 1.4:** This schematic reflects the linear time-of-flight mass spectrometer. \_\_ 8
- Figure 1.5:** Schematic of the Mass Gate (MG) and Momentum Decelerator (MD). \_ 12
- Figure 2.1:** Schematic of the overall apparatus from a top view. Chamber 1 has been drawn as if the top were removed so that chamber 2, also referred to as the internal box can be seen. The ion trap, which is located in chamber 1 and can be thought of as the terminal point of the ESI source, is shown. \_\_\_\_\_ 39
- Figure 2.2:** Schematic of the two source sides of the machine from a top view. The shaded enclosed area is shown to the side and portrays how the two sources are both aligned to transport ions to the center of the extraction plates. The enclosed area does not include the shutter, which is closed when the chamber 0 sources are running to protect the trap. When it is closed, ions fabricated in the ESI source will never make it to the extraction region. \_\_\_\_\_ 40
- Figure 2.3:** Schematic of the laser vaporization source. \_\_\_\_\_ 42
- Figure 2.4:** Schematic of the pulsed arc cluster ionization source (PACIS). \_\_\_\_\_ 43
- Figure 2.5:** This illustrates the general schematic of the electrospray ionization source in which the imperative components are labeled. \_\_\_\_\_ 45
- Figure 2.6: A)** This schematic depicts the copper block with the heated capillary. The copper block is held in the copper block holder and there is a spacer in between made of Teflon. The back view shows the holes in which the cartridge heaters are placed. **B)** This schematic depicts the copper block in the desolvation flange and the three other flanges, two spacer flanges and the skimmer 1 flange, that are used to hold the copper block in place. The entire assembly bolts on the first quadrupole chamber. \_\_\_\_\_ 47
- Figure 2.7:** This schematic depicts a top view, close up of the ESI source before the ion beam is bent 90° towards the ion trap. \_\_\_\_\_ 49

**Figure 2.8:** This schematic depicts a top view of the ion trap and ion optics after the ion beam is bent 90° towards the ion trap. \_\_\_\_\_ 51

**Figure 2.9:** This schematic depicts an exploded view of the ion trap so the individual components are clear. It is run in a closed configuration so ceramic rings are used. \_\_\_\_\_ 52

**Figure 2.10:** This schematic is a top view of the ESI source. The top port of chamber 1 that the cryostat is mounted on is shown. While the ion trap is located just below this port, it is clear that it is not quite center, resulting in the machining of an adapter ASA flange with a bore that is not centered. \_\_\_\_\_ 58

**Figure 2.11:** This schematic is a side view of the apparatus illustrating how the ion trap mounts to the bottom of the cold head of the liquid nitrogen cooled LT-4B cryostat. In this schematic, the heat shield and two apertures are not present. \_\_\_\_ 59

**Figure 2.12:** This is a schematic of the heat shield assembly. The heat shield adapter plate is connected directly to the LT-4B cryostat assembly by mounting onto the custom radiation shield mount. Two tunable, stainless steel apertures mount onto the heat shield bottom. There is a place to mount a pulse valve on the heat shield bottom. \_\_\_\_\_ 61

**Figure 2.13:** This is a schematic of the cryostat assembly. The LT-4B cryostat is mounted on top of a port aligner, which facilitates positional adjustments necessary when the ion trap is cryo-cooled, which bolts to the cluster flange housing the electrical and buffer gas connections. The cryostat heat shield is shown as mounted to the custom radiation shield mount and has apertures mounted on the bottom assembly. \_\_\_\_\_ 63

**Figure 2.14:** This schematic illustrates the existing pulse valve mount on the bottom of the heat shield assembly. \_\_\_\_\_ 64

**Figure 2.15:** This schematic is an exploded view of all the components of the cryostat, including all necessary pieces for mounting and the heat shield assembly. \_\_\_\_\_ 65

**Figure 2.16:** This is a schematic of the purge chamber designed and fabricated to accommodate air sensitive samples. Its assembling involves securing the polycarbonate tube in between the four support rods, the needle mounting flange, and the mounting flange. A needle mounting flange, which holds the fused silica tip assembly, is bolted onto the end of the threaded adapter flange. The threaded adapter flange is bolted onto the mounting flange using oversized washers for positional adjustments in all directions. O-rings are used to ensure all surfaces seal. \_\_\_\_\_ 68



**Figure 2.17:** This schematic demonstrates how the purge chamber is connected to the external part of the copper block holder. \_\_\_\_\_ 69

**Figure 2.18:** This is a schematic of chamber 1. The ports labeled **A**, **B**, and **C** represent where modifications were made to the vacuum system. On ports **A** and **B**, turbomolecular pumps were added in a 180° orientation. On port **C**, another turbomolecular pump was added in a 90° orientation. \_\_\_\_\_ 70

**Figure 2.19:** This is a schematic of the flight tube in both a top view and a bottom view to show the ports where vacuum modifications were made. On port **D**, a turbomolecular pump was added in a 90° orientation. On port **E**, a turbomolecular pump was added in a 180° orientation. On port **F**, an ion pump was moved and replaced with a larger turbomolecular pump. \_\_\_\_\_ 71

**Figure 2.20:** This is a schematic of the interaction region in a side view to show the port where vacuum modifications were made. On port **G**, a broken ion pump was removed and replaced with the working ion pump that used to be on port **F** of the flight tube. Note, there is also a cryopump in this region, but it is not shown here so that port **G** is visible. \_\_\_\_\_ 72

**Figure 2.21:** This is a schematic of the vacuum wall assembly added to the flight tube. **A)** This is a schematic of the flight tube such that the vacuum walls added are shown. **B)** This shows the all of the pieces of the vacuum wall together, including both the conductance plate and plate adapter. \_\_\_\_\_ 74

**Figure 2.22:** This is a schematic of the TOF mass spectrometer region. Here, the ion trap is used to indicate the ESI source side. As depicted, the extraction plates and deflectors are located inside the internal box (chamber 2). \_\_\_\_\_ 76

**Figure 2.23:** This schematic depicts the previous setup of the internal box (chamber 2), which includes the extraction plates and a box deflector. \_\_\_\_\_ 77

**Figure 2.24:** This is schematic of the new setup of the internal box (chamber 2). Now, the deflectors are separated with the horizontal deflector mounted first, followed by the vertical deflector. There are three grounded plates in this setup, one in the front, one in between, and one at the back. \_\_\_\_\_ 78

**Figure 2.25:** This is a schematic of the modified deflectors. Now, the horizontal and vertical deflection units are separate. The ions encounter the horizontal deflector first then the vertical deflector. There are grounded plates in front, in between, and at the end of the deflections units. The +U/-U is such that there is 0V on the middle axis. The deflection electrode plates are wider than before, so the ions encounter a uniform deflection field. \_\_\_\_\_ 79

<b>Figure 2.26:</b> This is a schematic of the first Einzel lens. <b>A)</b> The stainless steel spacers in between the second and third elements were made transparent to show the ceramic rods underneath. <b>B)</b> The lens tubes were mounted in the lens mounts via high temperature silver braze. _____	81
<b>Figure 2.27:</b> This is a schematic of the second Einzel lens stack. _____	83
<b>Figure 2.28:</b> This is a schematic illustrating how the second Einzel lens stack is mounted off the mass gate/momentum decelerator assembly and how it is supported in the chamber. _____	84
<b>Figure 2.29:</b> This schematic reflects the new design modifications that have been executed in the TOF mass spectrometer region. _____	85
<b>Figure 2.30:</b> This schematic depicts the general setup with the new design modifications implemented. _____	86
<b>Figure 2.31:</b> This schematic show the interaction region of the apparatus from a top view. In this schematic the cryopump is shown attached for completeness. _____	89
<b>Figure 2.32:</b> This is a schematic of the input light baffle. _____	90
<b>Figure 2.33:</b> This is the schematic of the output light baffle. <b>A)</b> This is a schematic of the ring mounts inside the vacuum chamber. <b>B)</b> This is a schematic of the outer cylindrical tube, which holds the internal apertures and spacers in place, mounted in the ring mounts. _____	90
<b>Figure 2.34:</b> Schematic of the old light baffle that used to be in the machine. Note that the output baffle is symmetric to the input baffle. <b>A)</b> This shows the orientation of the internal apertures, which vary in the diameter size of the center hole. Apertures A1 and A3 are threaded whereas A2 is not. The diameters of the apertures were: A1 (.52"), A2 (.275"), and A3 (.236"). <b>B)</b> Here, the spacers are shown, and since aperture A2 is not threaded, the spacers hold it in place. The lengths of the spacers were: SP1 (2.196") and SP2 (14.825"). _____	93
<b>Figure 2.35:</b> This is a schematic of the new light baffle where NAP1 is the input aperture. <b>A)</b> This shows the design of the new apertures used. The diameter of the center hole is 0.18" and is the same on all three apertures. NAP1 and NAP3 are threaded whereas NAP2 is not. The location of the apertures is the same in both the input and output baffle. <b>B)</b> This shows the spacers on the output baffle side. The spacers are identical with each having an outer diameter of 1.479", and inner diameter of 1.4", and a total length of 8". They are made from stainless steel <b>C)</b> This shows the spacers on the input light baffle. The inner diameter of the stainless steel tubes is the same. The outer diameter of most of the tube is 1.497", identical to the output baffle side; the length of that portion is 6.25". The other, smaller region has an outer diameter of 1.474" and a length of 1.75". _____	95

**Figure 3.1.** Propyne cation **g** (a) and **h** (b) vectors, with atom numbering used in this work. \_\_\_\_\_ 109

**Figure 3.2.** Three-dimensional plot of the coupled potential energy surfaces used in this work in the **g-h** plane, including the spin-orbit interaction. \_\_\_\_\_ 112

## **CHAPTER 1: INTRODUCTION**

## I. Introduction

The overlying theme of this experimental research is to obtain photoelectron spectra, which is accomplished by crossing a mass-selected beam of ions or clusters with a fixed-frequency photon beam then energy analyzing the resultant photodetached electrons. Two primary sources were utilized, an electrospray ionization source (ESI) and a laser vaporization source, reflecting the two sides of the apparatus. Both these sources are attached to the time-of-flight mass spectrometer and a magnetic bottle photoelectron spectrometer.

My time here was spent finishing the novel ESI source along with adding a cryostat to cool the ion trap and a purge chamber for air sensitive samples; modifying the time-of-flight mass spectrometer region by changing the two Einzel lenses and the deflectors; modifying the vacuum system; redesigning and installing new light baffles in the interaction region. All of these modifications made to the apparatus are detailed in Chapter 2.

Nonadiabatic processes, although ubiquitous in nature, are difficult to describe computationally due to the necessity to consider more than one potential energy surface. Chapter 3 focuses on propyne, which plays an important role in combustion processes, along with its cation. The ground electronic state of neutral propyne has an  $\sigma$  orbital as the highest occupied molecular orbital (HOMO) and corresponds to the  $\pi$ -orbitals of the C-C triple bond. The cation is a doubly degenerate  $^2E$  state subject to a first order Jahn-Teller distortion and spin-orbit induced splitting of the  $^2E$  state into Kramers' doublets.

Within the literature, two works on propyne photoionization reach fundamentally different conclusions concerning the importance of the Jahn-Teller effect in the electronic structure of the propyne cation. Pulsed-field ionization measurements, by Matsui et al.,<sup>1</sup> resolved spin-orbit structure in the rotational profile of the origin band in the nonresonant two-photon threshold photoionization. Using the spin-orbit splitting of the acetylene cation ( $A=-30.9\text{ cm}^{-1}$ ), a propyne cation structure is proposed to be very close to that of the neutral ground state, which implies a minimal impact of the Jahn-Teller interaction. More recently, Xing et al.<sup>2</sup> obtained rotational spectra for the cation and found the spin-orbit constant to be  $A=-13\text{ cm}^{-1}$  and the ratio of photoionization cross-sections to be  $E_{1/2}/E_{3/2}=4:1$ . The contradiction arises since the observed  $A=-13\text{ cm}^{-1}$  implies significant Ham reduction and implies a consequential Jahn-Teller effect.

In order to address these discrepancies, the ground electronic state of propyne and the  $1,2^2A$  states of the propyne cation were determined along with the minimum energy conical intersection of the  $1,2^2A$  states. The results were used to simulate the photoionization spectrum of propyne using the vibronic coupling model. Spin-orbit effects were included within the Breit-Pauli approximation using an intensity borrowing approach. The effect of the spin-orbit interaction on the relative intensity and spacing of the two lowest energy levels in the spectrum were also considered.

## **II. Experimental**

The overlying theme of this research is anion photoelectron spectroscopy (PES), which is accomplished by crossing a mass-selected beam of ions with a fixed-

frequency photon beam and then energy analyzing the resultant photodetached electrons. The photodetachment process is governed by the energy conservation relationship

$$h\nu = EBE + EKE + NKE \quad (1.1)$$

where  $h\nu$  is the photon energy,  $EBE$  is the electron binding energy,  $EKE$  is the measured electron kinetic energy, and  $NKE$  is the neutral recoil kinetic energy. The  $NKE$  is miniscule compared to  $EKE$ , and much smaller than the resolution of the magnetic bottle photoelectron spectrometer and so it is ignored. This process is schematically shown in figure 1.

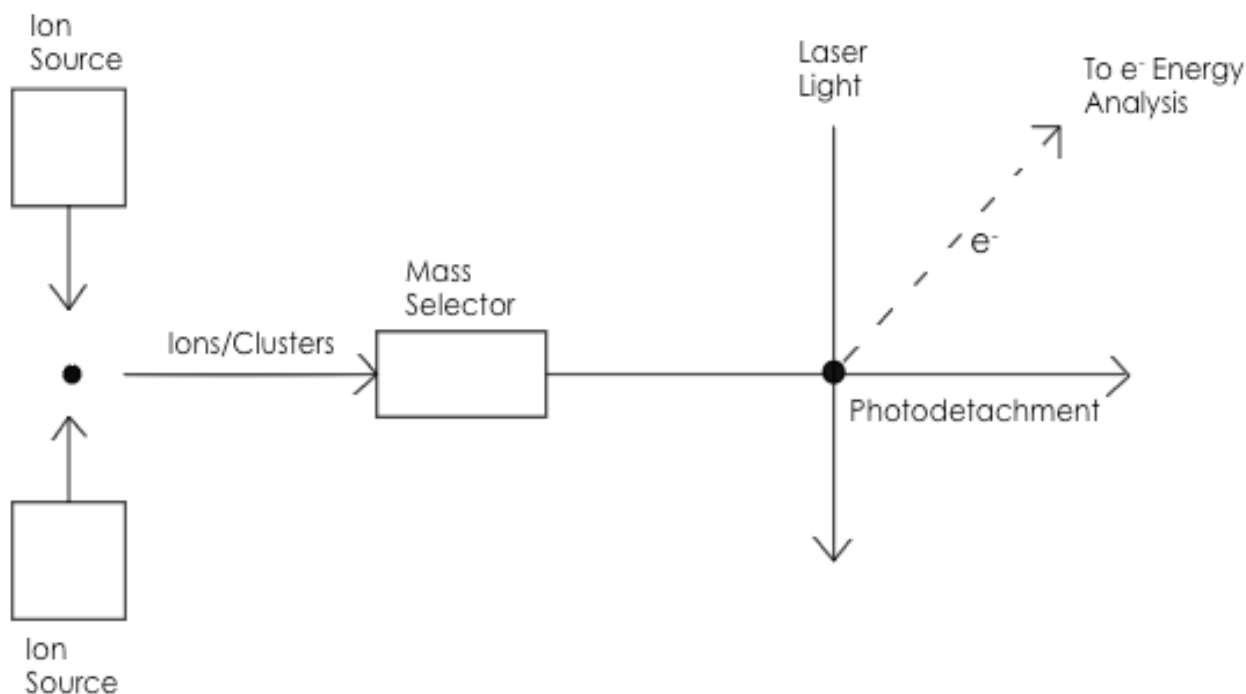


Figure 1.1: Photodetachment process with mass selected anions.

Detachment from the anion probes the neutral ground and excited state potential energy surfaces. The photoelectron spectrum collected provides a wealth of information. The adiabatic electron affinity of the neutral cluster, which is

equivalent to the energy difference between the ground state of the neutral and the anion, is obtained. The adiabatic detachment energy, which is the energy difference between an anion and the corresponding neutral at its minimum, is also obtained. The vertical detachment energy, which is the energy difference between the anion and the neutral at the geometry of the anion can also be evaluated. These experiments, along with complementary theoretical calculations, facilitate elucidating other valuable information such as geometric structures.

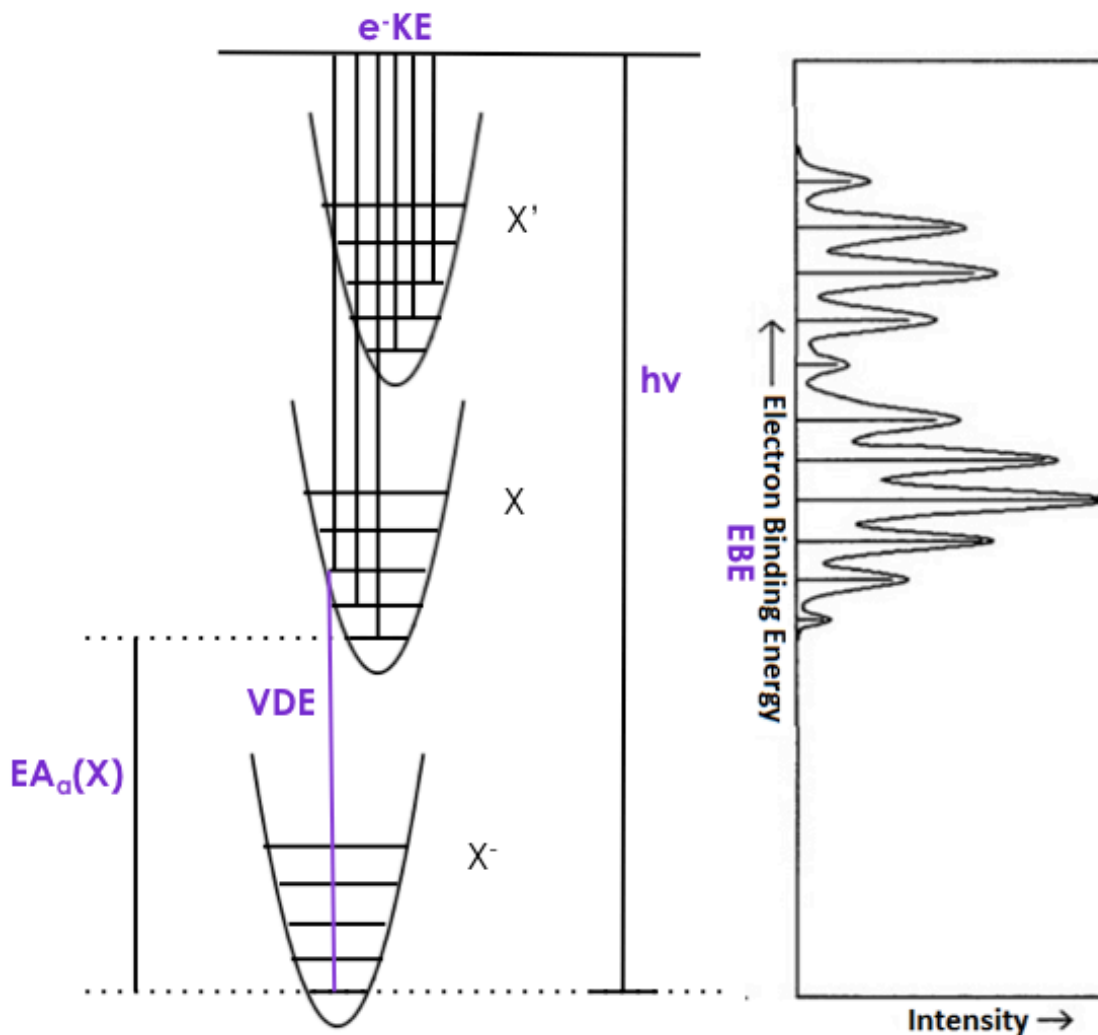


Figure 1.2: Schematic of photoelectron spectroscopy; detachment from the anion probes the neutral ground and excited state potential energy surfaces.



An ancillary focus of this research is to create and investigate clusters. Investigating atomic and molecular cluster allows the physical properties of matter as a function of size to be analyzed.<sup>44</sup> Using negative ion photoelectron spectroscopy allows for the exploration of the electronic states of these species providing insight on electron affinities and vibrational frequencies. The coupling of mass spectroscopy with photoelectron spectroscopy to investigate cluster anions reveals magic number effects and information about cluster evolution towards bulk material. Such information will develop a molecular level description that will lead to a “ground up” understanding of complex bulk phenomena.<sup>45</sup> While it has been well established that molecular clusters exhibit fluid-like behavior, providing experimental evidence of fluidity in atomic clusters is less convincing.<sup>44</sup> Recently, there is great interest in systems where the clusters are fluid, or exhibit fluid-like behavior. Helium clusters, which have proven to be fluid, have gained considerable theoretical and experimental attention. It was found that a droplet containing 270 helium atoms exhibits properties similar to the bulk.<sup>44</sup> Methods have been developed to dope helium clusters with atoms or molecules and then use spectroscopy to probe the local microscopic environment.<sup>46</sup> Furthermore, there is considerable interest in cooling ions and clusters, which refers to collisional damping to reduce ion or cluster temperatures below room temperature. This results in better resolved spectra since rotational and vibrational cooling is accomplished and is exploited in the ESI source.

## A. General Apparatus Overview

The apparatus used can be thought of as having two separate source sides. The figure below is a general schematic of the apparatus before major renovations and modifications were performed.

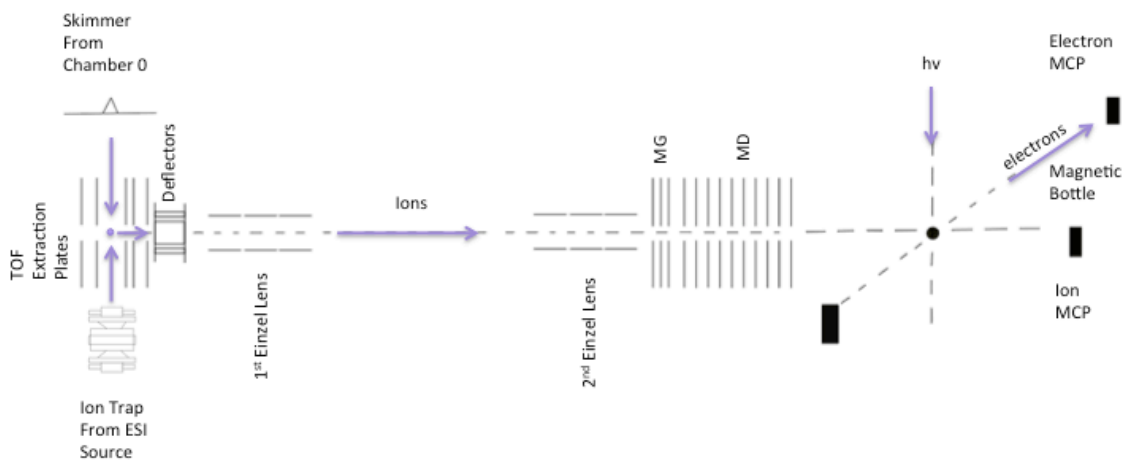


Figure 1.3: General schematic of PIPES apparatus before renovations and additions.

## B. Time-of-Flight (TOF) Mass Spectrometer

The time-of-flight mass spectrometer determines the mass of ions by measuring the ion arrival times at the detector after they have been simultaneously accelerated by a potential difference. The linear time-of-flight mass spectrometer on the apparatus is a modified Wiley-McLaren arrangement for ion extraction<sup>3</sup> first described by de Heer and Milani<sup>4</sup>, then by Wang and coworkers<sup>5</sup>.

To understand the basic principle of a time-of-flight mass spectrometer, first assume that the electrostatic field within the acceleration region and the length of the region are both zero. The mass spectrometer then simply consists of an extraction region, a drift region, and an ion detector. Figure 1.4 illustrates these regions.

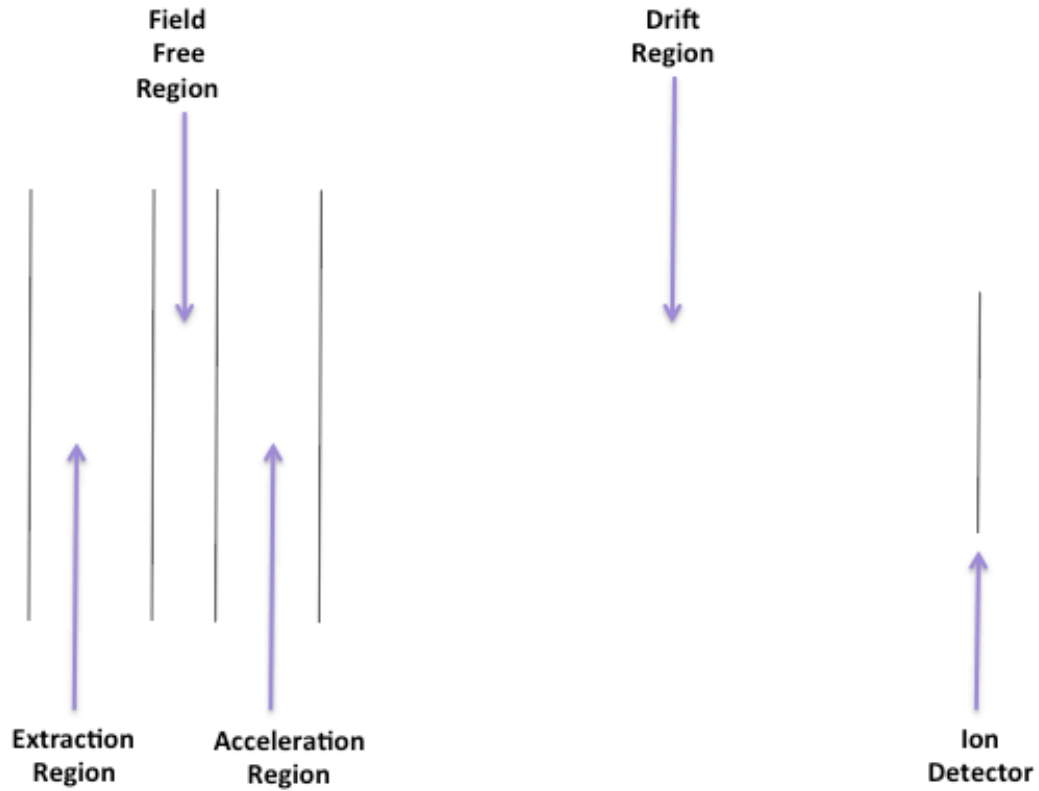


Figure 1.4: This schematic reflects the linear time-of-flight mass spectrometer.

The ions of varying masses enter the extraction region, where they are accelerated by an electrostatic field that is defined by two parallel grids towards the ion detector. The kinetic energy imparted to the ion by the applied field is given by

$$KE = qV \quad (1.2)$$

where  $q$  is the charge of the ion and  $V$  is the voltage for acceleration.

Ions that have the same charge but different masses are accelerated at different velocities. Using the definition of the kinetic energy, equation 1.2 becomes

$$qV = \frac{mv^2}{2} \quad (1.3)$$

where  $m$  is the mass of the ion and  $v$  is the velocity leaving the extraction region.

This can be rearranged in terms of the velocity as

$$v = \sqrt{\frac{2qV}{m}} \quad (1.4)$$

The time that an ion will take to reach the detector a distance D is given by the equation

$$time = \frac{D}{v} = D \sqrt{\frac{m}{2qV}} \quad (1.5)$$

It is obvious from equation 1.5 that the ion flight time from the extraction region to the detector is proportional to the square root of the mass. Since the electric fields remain essentially constant and the distance to the detector is constant, the mass is proportional to the square of the ion flight time:  $m = Xt^2$  where X are just the relevant constants. The measured flight time must account for experimental factors, such as trigger delays; therefore, accounting for those factors, the resulting equation is

$$t + b = a\sqrt{m - c} \quad (1.6)$$

where a, b, and c are empirically determined constants; t is the measured ion flight time, and m is the measured ion mass. Rearranging in terms of mass gives

$$m = \frac{(t + b)^2}{a^2} + c \quad (1.7)$$

Equation 1.7 is especially important for mass calibration. The a, b, and c constants are readily determined by knowing three data points of ion masses with the corresponding flight times.

At the core of the linear TOF mass spectrometer, there are four plate electrodes, or extraction plates. In the actual experimental setup, a -1500V pulsed

voltage is applied to the first extraction plate, a -1390V pulsed voltage is applied simultaneously to the second and third extraction plates, and the fourth extraction plate is grounded. The voltage applied to the second and third extraction plates slightly varies due to experimental conditions and is optimized to achieve the best mass resolution ( $m/\Delta m$ ), where  $m$  is the mass of the ion of interest and  $\Delta m$  is the full width at half maximum (FWHM). Since the source generated ions have an initial velocity perpendicular to the extraction field, deflectors were utilized. Two Einzel lenses were also used to focus the ion beam towards the ion microchannel plate (MCP) detector. These elements will be discussed in greater detail in chapter two along with their associated modifications.

### **C. Mass Gate & Momentum Decelerator**

In order to minimize the contributions of other close mass ions, a gated mass filter is often employed in studies involving mass-selected ions and is referred to as a mass gate. Since ions of different masses will arrive at the mass gate at different times, the mass gate can allow only an ion packet of a selected mass to reach the photoelectron spectrometer while filtering out the other ions. The mass gate consists of three closely spaced parallel grids. The spaces between the grids are kept as close as possible, about 2mm, in order to achieve optimal mass selection resolution.<sup>6,7</sup> The end grids are held at ground and a negative voltage is applied to the middle grid. The voltage applied is more negative than the one applied to the first extraction plate so that no ions will be able to pass. The voltage is then briefly dropped to zero when the ions of interest enter the mass gate region and leave it before the voltage returns, allowing those particular ions to pass through.

A momentum decelerator is utilized to improve the photoelectron spectrometer resolution. The most crucial limitation stems from the anion velocity,  $v_a$ . Since the photodetached electrons are collected from nearly a  $4\pi$  solid angle, the velocity of the electron  $v_e$ , in the laboratory frame of reference ranges between  $v_e + v_a$  and  $v_e - v_a$ . The resultant velocity spread,  $2v_a$ , leads to a broadened distribution of the electrons initial kinetic energy, which is expressed as

$$\Delta E = 4\sqrt{\frac{m_e}{m}} \cdot \sqrt{E_{KE} \cdot E_a} \quad (1.7)$$

where  $E_a$  is the ions kinetic energy. This is called Doppler broadening and leads to poorer resolution and peak distortions.

The scheme of the mass gate and the momentum decelerator in the apparatus is very similar to Wang's design.<sup>5</sup> To decelerate the anions of interest, a positive voltage pulse is applied to the first plate of the momentum decelerator. The degree of deceleration is optimized by adjusting the voltage and duration of the deceleration pulse.

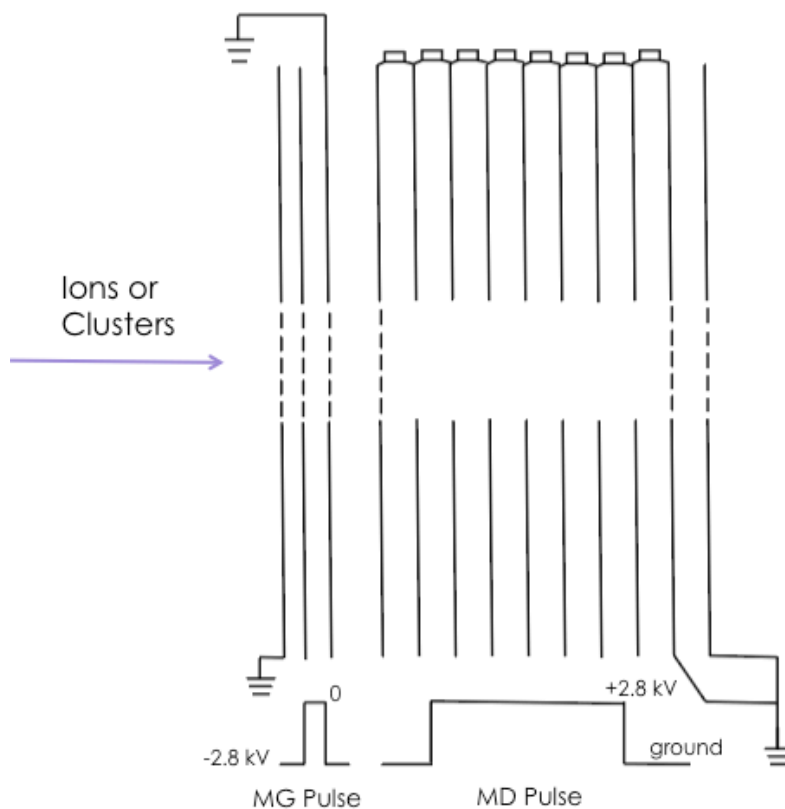


Figure 1.5: Schematic of the Mass Gate (MG) and Momentum Decelerator (MD).

#### D. Magnetic Bottle Photoelectron Spectrometer

A time-of-flight photoelectron spectrometer analyzes the electron kinetic energies by measuring the flight time of the electrons. There are two types of TOF photoelectron spectrometers, field free and magnetic bottle. While a field free photoelectron spectrometer generally gives better resolution, the magnetic bottle photoelectron spectrometer has a much more advantageous collection efficiency. In a field free photoelectron spectrometer, the emitted electrons are focused in a narrow cone facing the detector, minimizing Doppler effects but failing to detect the majority of the electrons since they are emitted in different directions. Magnetic bottle photoelectron spectrometers use a divergent magnetic field to direct most of the electrons toward the detector while conserving the electron kinetic energy. The

first magnetic bottle type photoelectron spectrometer was reported by Kruit and Read<sup>8</sup> and had the ability to detect electrons ejected from a  $2\pi$  solid angle.

As previously mentioned, magnetic bottle photoelectron spectrometers use a divergent magnetic field and the field lines resemble the top of a wine bottle. The magnetic fields change gradually from a strong field,  $B_s$ , to a weak uniform field,  $B_w$ . The strong field is generated by a high field permanent magnet while the weak field is generated by a solenoid that spans a drift region. This method allows for a collection angle of nearly  $4\pi$  solid angle, a design improvement from the original, indicating that nearly all the electrons generated by a detachment process can be collected and analyzed.

Electron motion in a divergent magnetic field generally proceeds as follows: The Lorentz force  $e\mathbf{v} \times \mathbf{B}$  causes a photodetached electron to spiral around a magnetic field line as it follows it from the high field to the low field regions of the bottle. The total velocity of the electron remains constant, but the Lorentz force has a component along the axis of the bottle, which will result in an increase in the axial component of the electron's velocity and a decrease in the transverse velocity component. The net effect of the magnetic field is the parallelization of electron velocities to the axis of the bottle regardless of the initial direction of the electron's velocity vector.<sup>8</sup> An electron trajectory within the bottle can be described as a continuously loosening spiral in the direction of and around a particular magnetic field line.

In this apparatus, the magnetic bottle uses a low field solenoid (2-5G) and a high field permanent magnet (400-1000G). The bottle is shielded with  $\mu$ -metal to



minimize the effect from external fields, such as the Earth's magnetic field. The interaction region is shielded with a shroud, which is a nonmagnetic stainless steel tube (2' in diameter) to minimize residual electric fields in that region.<sup>6,7</sup>

The conversion from the electrons time-of-flight to kinetic energy is accomplished in an analogous manner as previously described for converting the ions flight time to mass in the previous section. In this case, all the electrons have the same mass so the different arrival times reflect differences in kinetic energy. Its flight time can be expressed as

$$t_e = \frac{L_e \sqrt{m_e}}{\sqrt{2}} \frac{1}{\sqrt{EKE}} \quad (1.8)$$

where  $t_e$  is the electron flight time,  $L_e$  is the distance between the interaction region and the MCP electron detector,  $m_e$  is the electron mass, and  $EKE$  is the electron kinetic energy. In this specific setup,  $L_e$  and  $m_e$  are constant so equation 1.8 can be more generally written as

$$t_e = \frac{C_e}{\sqrt{EKE}} \quad (1.9)$$

where  $C_e$  simply reflects the relevant constants.

Just as before, during actual experiments the flight time will be affected by unavoidable factors, such as trigger delays and electron parallelization time, and the equation will be modified to account for such effects giving

$$t_e + b = \frac{a}{\sqrt{EKE - c}} \quad (1.10)$$

where  $a$ ,  $b$ , and  $c$  are empirically determined constants. Rearranging,

$$EKE = \frac{a^2}{(t_e + b)^2} + c \quad (1.11)$$

Using equation 1.1, the electrons' binding energy is formulated.

$$EBE = h\nu - \left[ \frac{a^2}{(t_e + b)^2} + C \right] \quad (1.12)$$

### III. Theory

Polyatomic molecules are complex by nature since their structure and properties are governed by the concerted motions of the constituent particles and the particles respective interactions. Thus, it is routine to make approximations to ease the solution of the Schrödinger equation. The Schrödinger equation is the fundamental equation of quantum mechanics and its solutions, the wave functions, give the complete description of any system. The non-relativistic, time-independent Schrödinger equation is given by<sup>9</sup>

$$H^T(\mathbf{r}, \mathbf{R}) - E_l^T \Psi_l^T(\mathbf{r}, \mathbf{R}) = 0 \quad (2.1)$$

where  $H^T$  is the Hamiltonian operator of the system<sup>9</sup>,

$$H^T(\mathbf{r}, \mathbf{R}) = T^{nuc} + T^e + V^{e,N}(\mathbf{r}, \mathbf{R}) + V^{N,N}(\mathbf{r}, \mathbf{R}) + V^{e,e}(\mathbf{r}, \mathbf{R}) \quad (2.2)$$

In the total Hamiltonian given above, the first term represents the kinetic energy for the  $N^{at}$  nuclei, coordinates  $\mathbf{R}_\alpha$ ,  $\alpha = 1-N^{at}$ ; the second term represents the kinetic energy for the  $N^{el}$  electrons, coordinates  $\mathbf{r}_a$ ,  $a = 1-N^{el}$ ; the third term represents the Coulomb attraction between the electrons and nuclei; while the last two term represents the Coulomb repulsion operation between electrons and between nuclei. This equation is directly solvable for only the simplest systems. These terms are described below. Atomic units are used unless otherwise noted.

$$T^{nuc} = \sum_{\alpha=1}^{N^{at}} -\frac{1}{2M_{\alpha}} \nabla_{\alpha}^2 \quad (2.3)$$

$$T^e = \sum_{a=1}^{N^{elec}} -\frac{1}{2} \nabla_a^2 \quad (2.4)$$

$$V^{e,N}(\mathbf{r}, \mathbf{R}) = \sum_{\alpha} \sum_{\alpha} \frac{-Z_{\alpha}}{r_{\alpha,\alpha}} \quad (2.5)$$

$$V^{N,N}(\mathbf{r}, \mathbf{R}) = \sum_{\alpha} \sum_{\alpha>\beta} \frac{Z_{\alpha}Z_{\beta}}{r_{\alpha,\beta}} \quad (2.6)$$

$$V^{e,e}(\mathbf{r}, \mathbf{R}) = \sum_a \sum_{a>b} \frac{1}{r_{a,b}} \quad (2.7)$$

The Born-Oppenheimer approximation is one of the most notable approximations used. This approximation reasonably assumes that the Hamiltonian can be solved in two stages due to the large difference in mass between the nuclei and electrons.<sup>9</sup> The electrons are then traveling at a velocity far greater than the nuclei; the nuclei are moving on a single potential energy surface created by the faster moving electrons. First, the kinetic energy of the nuclei is neglected and the internuclear potential is considered constant. The remaining terms comprise the electronic Hamiltonian, which describes the motion of the electrons in a field of stationary nuclei. The equations below show the electronic Hamiltonian.<sup>9</sup> It is important to note that it still has a parametric dependence on the nuclear coordinates.

$$[H^e(\mathbf{r}; \mathbf{R}) - E_i^e(\mathbf{R})]\Psi_i^{e,a}(\mathbf{r}; \mathbf{R}) = 0 \quad (2.8)$$

where<sup>9</sup>

$$H^e(\mathbf{r}, \mathbf{R}) = T^e + V^{e,N}(\mathbf{r}, \mathbf{R}) + V^{N,N}(\mathbf{r}, \mathbf{R}) + V^{e,e}(\mathbf{r}, \mathbf{R}) \quad (2.9)$$

Second, the nuclear Hamiltonian is solved using the solution of the electronic part as the potential on which the nuclei move. This will yield equations describing the rotational and vibrational motions of the nuclei.

$$(H^T(\mathbf{r}, \mathbf{R}) - E_i^e(\mathbf{R}))\chi_i^N(\mathbf{r}, \mathbf{R}) = 0 \quad (2.10)$$

where

$$H^T(\mathbf{r}, \mathbf{R}) = T^{nuc} + H^e(\mathbf{r}, \mathbf{R}) \quad (2.11)$$

The total wavefunction is then expressed as the simple product of the two wavefunctions.

$$\Psi^T(\mathbf{r}, \mathbf{R}) = \Psi_i^{e,a}(\mathbf{r}, \mathbf{R})\chi_i^N(\mathbf{R}) \quad (2.12)$$

### A) Nonadiabatic Interactions

While this approximation is central to theory, there are a plethora of cases where it fails to adequately describe chemical events. Such cases are referred to as nonadiabatic processes, which are characterized as occurring in regions of nuclear coordinate space where Born-Oppenheimer potential energy surfaces become close and even intersect. These nonadiabatic processes, although ubiquitous in nature, are difficult to describe computationally due to the necessity to consider more than one potential energy surface.<sup>10-12</sup>

Conical intersections are not necessarily required by symmetry though there are symmetry-required intersections. Such intersections of multidimensional potential energy surfaces can happen in polyatomic systems as long as it is in accordance with the “noncrossing rule” of von Neumann and Wigner.<sup>13,14</sup> This states that two independent constraints must be satisfied by the parameterized electronic Hamiltonian to obtain a crossing point of two electronic states of the same

symmetry. Such intersections can either be symmetry-allowed or same-symmetry intersections and are designated as accidental conical intersections.<sup>15</sup> Symmetry-allowed conical intersections involve electronic states belonging to distinct irreducible representations while in same-symmetry conical intersections the point group symmetry is absent. The “noncrossing rule” permits the dimensionality of the intersections space to be characterized.

When electronic states approach one another, the electronic structure and nuclear motion can no longer be approximated as independent to which the Born-Huang expansion presents a solution.<sup>16</sup> The total wave function dependent upon all electronic and nuclear coordinates is expressible as<sup>17</sup>

$$\Psi_K^T(\mathbf{r}, \mathbf{R}) = \sum_{J=1}^{N^{state}} \Psi_J^{e,a}(\mathbf{r}, \mathbf{R}) \chi_J^K(\mathbf{R}) \quad (2.13)$$

where  $\chi_J^K(\mathbf{R})$  are the expansion coefficients and  $\Psi_M^{e,a}$  are the adiabatic electronic basis set wave functions. Substituting the above total wave function expansion into the nonadiabatic Hamiltonian, equation 2.10, and taking the inner product with the  $\Psi_M^{e,a}$ , gives the system of coupled differential equations for the nuclear coordinate expansion coefficients.<sup>17,18</sup>

$$T^{nuc} + E_l^e(\mathbf{R}) + K_{l,l}(\mathbf{R}) - E_k^T \chi_l^K(\mathbf{R}) = \sum_{J \neq l} \{\Lambda_{lJ}(\mathbf{R})\} \chi_J^K(\mathbf{R}) \quad (2.14)$$

The  $\Lambda(\mathbf{R})$  term represents the nonadiabatic coupling term that originates from the nuclear kinetic energy operating on the electronic wave functions.<sup>11</sup> This coupling term is composed of two terms, the derivative coupling vector,  $\mathbf{f}^{lJ}(\mathbf{R})$ , and

the adiabatic diagonal correction  $K_{I,I}$ , which are the terms responsible for interactions between surfaces. The equations for these terms are given below.<sup>17,18</sup>

$$\Lambda_{IJ}(R) = \sum_{L=1}^{Nat} \frac{f_L^{I,J}(\mathbf{R})}{M_L} \cdot \nabla_L - K_{I,J}(\mathbf{R}) \quad (2.15)$$

where

$$f_L^{I,J}(\mathbf{R}) = \langle \Psi_I^{a,e}(\mathbf{r}, \mathbf{R}) | \nabla_L \Psi_J^{a,e}(\mathbf{r}, \mathbf{R}) \rangle_{\mathbf{r}} \quad (2.16)$$

$$K_{I,J}(\mathbf{R}) = \langle \Psi_I^{a,e}(\mathbf{r}, \mathbf{R}) | T^{nuc} \Psi_J^{a,e}(\mathbf{r}, \mathbf{R}) \rangle_{\mathbf{r}} \quad (2.17)$$

The behavior of  $K_{I,I}(\mathbf{R})$  near a conical intersections produces a discontinuity in the adiabatic wavefunctions at the intersection. The failure of the Born-Oppenheimer approximation is due to this coupling between the electronic and nuclear motion.

The derivative coupling is a measure of the variation of the electronic wave function with the nuclear coordinates.<sup>19</sup> When states are not well separated, the Born-Oppenheimer approximation breaks down due to the couplings between states becoming significant. Derivative couplings approach infinity at conical intersections, creating complications. This occurs because derivative couplings are inversely proportional to the energy difference between states, which is zero at a conical intersection.

## **B) Adiabatic to Diabatic Basis**

When the Born-Oppenheimer approximation breaks down, where more than one potential energy surfaces come within close proximity to each other or even cross, the problem of appropriate wave functions becomes relevant.<sup>20</sup> The motivation behind the construction of diabatic bases<sup>21-23</sup> is to transfer the couplings

that arise from the nuclear kinetic energy operator to off-diagonal matrix elements of the electronic Hamiltonian. The construction of diabatic bases occurs by applying a unitary transformation to the adiabatic electronic states. The adiabatic states are expanded in a configuration state function basis (CSF), which are linear combinations of Slater determinants, as:<sup>18,19</sup>

$$\Psi_i^{a,e}(r, R) = \sum_{\alpha} c_{\alpha}^i \psi_{\alpha}(r; R) \quad (2.18)$$

The diabatic states are then constructed from the adiabatic states with the use of a unitary transformation.<sup>24,25</sup>

$$\Psi_u^d(q; R) = \sum_{l=1}^{N^{state}} \Psi_l^{a,e}(q; R) (d^{-1})_u^l(R) \quad (2.19)$$

A true diabatic state is one in which the derivative couplings vanish globally and does not exist. Thus, the states resulting from this transformation are typically referred to as quasi-diabatic states. The transformation to diabatic states mostly eliminates the singularity in the derivative couplings at a point of conical intersection. The transformation from adiabatic states to diabatic states equivalently transforms the nonadiabatic Hamiltonian to:<sup>26</sup>

$$(T^{nuc} + H_{M,M}^{e,d}(\mathbf{R}) - E_K^T) \chi_M^{K,d}(\mathbf{R}) = \sum_{J \neq M} H_{M,J}^{e,d} \chi_J^{K,d}(\mathbf{R}) \quad (2.20)$$

where

$$H_{M,J}^{e,d}(\mathbf{R}) = \langle \Psi_J^{e,d}(\mathbf{r}, \mathbf{R}) | H^e | \Psi_M^{e,d}(\mathbf{r}, \mathbf{R}) \rangle \quad (2.21)$$

### C) Intersection Adapted Coordinates

A characteristic feature of conical intersections is that the adiabatic electronic wave function changes sign when transported along a closed loop

surrounding the conical intersection.<sup>27,28,29</sup> Furthermore, as described by the Berry phase effect, when an adiabatic electronic wave function is transported around a closed loop around a point of conical intersection in the nuclear coordinate space, an additional geometric or Berry phase is acquired.<sup>30</sup> This additional phase compensates for the changes in the phase of the adiabatic electronic wave function, since it cannot be both real valued and continuous. This phase effect is a consequence for using the adiabatic basis, which is another reason to use diabatic states.<sup>30</sup>

It is important to note that not all closed loop path are equivalent and that there will be a preferential one.<sup>31</sup> Furthermore, conical intersections are not isolated points but instead are connected continuously forming a seam.<sup>31</sup> At a point of conical intersection, **g** and **h** vectors can be defined such that  $2\mathbf{g}$  is the energy difference gradient and  $\mathbf{h}^{I,J} = \lim_{R \rightarrow R_x} \Delta E_{I,J} \mathbf{f}_{I,J}$  and is parallel to the derivative coupling vector,  $\mathbf{f}_{I,J}$ . Generally, these vectors are not orthogonal however by using a unitary transformation at a conical intersection, they can be made orthogonal.<sup>26</sup> These two vectors define the **gh**-plane in which the degeneracy of the conical intersection is lifted linearly. In this plane the energy gradients and derivative couplings are well behaved.

By using the **g** and **h** vectors a canonical representation of the internal nuclear degrees of freedom can be constructed with regard to conical intersections. It becomes convenient to use intersection adapted coordinates, in which the **g** and **h** vectors compliment a  $N^{\text{int}}-2$  dimensional seam space with coordinates mutually orthogonal and mutually orthogonal to **g** and **h**.<sup>32</sup> Such a set of internal coordinates



is referred to as intersection adapted coordinates and provide a complete description of the nuclear motions in the vicinity of intersecting surfaces.

### D) Locating Conical Intersections

The determination of a conical intersection can be computationally costly, especially if an indirect method is used where the two potential energy surfaces involved are determined first. Another direct method can be used in which intersection point is determined without determining the potential energy surfaces first. The direct method algorithm is utilized here, which directly locates the portions of the crossing surfaces that are energetically relevant.

It is crucial to note that conical intersections are not isolated points but instead are connected continuously forming a seam. Conical intersections composed of two states of the same symmetry represent a crossing surface of dimension  $N-2$ , where  $N$  is the number of internal coordinates.<sup>33</sup> The algorithm used determines the minimum energy point of the crossing surface as well as allowing for the possibility of a minimization subject to geometric constraints.<sup>33</sup> The minimization is accomplished by determining the extrema of the following Lagrangian function:

$$L_{IJ}(\mathbf{R}, \xi, \lambda) = E_I(\mathbf{R}) + \xi_1 \Delta E_{IJ}(\mathbf{R}) + \frac{\xi_2 H_{IJ}(\mathbf{R})}{2} + \sum_{k=1}^M \lambda_k C_k(\mathbf{R}) \quad (2.22)$$

where  $\xi$  and  $\lambda$  are Lagrange multipliers,  $\Delta E_{IJ}(\mathbf{R}) = E_I(\mathbf{R}) - E_J(\mathbf{R})$ ,  $H_{IJ}(\mathbf{R}) = \langle \Psi_I(\mathbf{r}; \mathbf{R}) | H^e(\mathbf{r}; \mathbf{R}) | \Psi_J(\mathbf{r}; \mathbf{R}) \rangle_r$ , and  $H^e(\mathbf{r}; \mathbf{R})$  is the nonrelativistic Hamiltonian. The  $\xi$  Lagrange multipliers correspond to the constraints  $\Delta E_{IJ}(\mathbf{R})=0$  and  $H_{IJ}(\mathbf{R})=0$ , implying that the energy difference and the coupling between the electronic states are both

zero. The  $\lambda$  Lagrange multipliers provide geometric restraints, such as restricting bond angles.<sup>33</sup>

In the case of two states of the same symmetry, the case  $H_{11}(\mathbf{R})=0$  is satisfied automatically for all  $\mathbf{R}$ .<sup>34</sup>

$$\begin{bmatrix} \mathbf{g}^I(\mathbf{R}) + \xi_1 \mathbf{g}^{IJ}(\mathbf{R}) + \xi_2 \mathbf{h}^{IJ}(\mathbf{R}) + \sum_{i=1}^M \lambda_i \mathbf{k}^i(\mathbf{R}) \\ \Delta E_{IJ}(\mathbf{R}) \\ 0 \\ \mathbf{C}(\mathbf{R}) \end{bmatrix} = \begin{bmatrix} 0 \\ 0 \\ 0 \\ 0 \end{bmatrix} \quad (2.23)$$

Extrema of the Lagrangian function are located by setting the energy gradient to zero<sup>33</sup> and using a second order approximation that gives Newton-Raphson equations that are iteratively solved until equation 2.23 is satisfied.

## E) Simulating Spectra

Frequently, it is desirable to not only determine critical points but to also reproduce enough of the potential energy surfaces to be able to simulate a vibronic spectrum. Simulating spectra that contain intersecting potential energy surfaces is more involved due to the vibrational motion no longer being confined to one electronic surface but rather proceeding on both surfaces simultaneously due to nonadiabatic coupling. In order to do this, the multimode vibronic coupling model is used, which has been shown as a powerful tool for determining spectra of molecules having conical intersections.<sup>35-38</sup>

The nonrelativistic spectral intensity distribution function is given by<sup>39</sup>

$$I(E) = 2\pi \sum_f |A_f^i|^2 \delta(E - E_f) \quad (2.22)$$

where

$$A_f^i = \langle f | \mu | i \rangle \quad (2.23)$$

and  $|i\rangle$  is the fixed initial state,  $|f\rangle$  is a final state, and  $\mu$  is a transition moment operator.

In the vibronic coupling model, the initial state is assumed to be well described by a single electronic potential energy surface while the final state is a complicated vibronically coupled state. The sudden approximation is used here, which assumes that the wave function of the final state is unaltered by the photodetached electron allowing the final state to be determined without first determining the transition moment.<sup>39</sup> The vibronic wave functions are expressed as a sum of products of an electronic term and a vibrational term.

The initial state is composed of an adiabatic electronic state for a molecule with  $N^{el}+1$  electrons and a vibrational wave function that is given by the multimode product of the normal modes of the harmonic potential for the initial state

$$|i\rangle = \Psi_0^a(\mathbf{r}^{N^{el}+1}, \mathbf{Q}') \Theta_I^0(\mathbf{Q}') \quad (2.24)$$

where

$$\Theta_I^0(\mathbf{Q}') = \sum_{j=1}^{N^{int}} \chi_{I_j}^{0,j}(\mathbf{Q}'_j) \quad (2.25)$$

and  $\mathbf{Q}'$  are the normal modes of the corresponding harmonic potential and  $\chi_m^{0,j}$  denotes the  $m$ th harmonic oscillator function corresponding to the  $j$ th mode of the initial state harmonic potential.<sup>39</sup>

The final state is a vibronic level with  $N^{\text{el}}$  electrons and one photodetached electron. The wave function employs diabatic electronic states and must be expanded as a sum of vibronic products. Since there are  $N^{\text{el}}$  rather than  $N^{\text{el}}+1$ , only a correct description of the photodetached species can be described<sup>39</sup>

$$|f\rangle = \sum_{\alpha=1}^{N^{\text{state}}} \Psi_{\alpha}^d(\mathbf{r}^{N^{\text{el}}}; \mathbf{Q}) \Theta_{\alpha}^f(\mathbf{Q}, t) \quad (2.26)$$

where

$$\Theta_{\alpha}^f(Q) = \sum_m d_{\alpha,m}^f \prod_{i=1}^{N^{\text{int}}} \chi_{m_i}^{\alpha,i}(Q_i), \quad 0 \leq m_i < M_i \quad (2.27)$$

and  $d_{\alpha,m}^f$  is an  $N^{\text{state}}N^{\text{vib}}$  dimensional eigenvector. The same multimode basis is used for all the electronic states.

The total Hamiltonian has the form<sup>38,39</sup>

$$H^T = T^{\text{nuc}} + H^e = H^{T,\text{nr}} \quad (2.28)$$

where  $T^{\text{nuc}}$  is the nuclear kinetic energy operator,  $H^e$  is the electronic Hamiltonian, which is also the Coulomb Hamiltonian, and  $H^{T,\text{nr}}$  denotes the nonrelativistic Hamiltonian. The nonrelativistic nuclear-electronic Schrodinger equation is then<sup>35</sup>

$$(H^{T,\text{nr}} - E_f^{T,\text{nr}}) \Psi_f^{T,\text{nr}} = 0 \quad (2.29)$$

The kinetic energy operator is expanded as a sum of vibronic products with diabatic electronic states. Again, the vibrational basis generally used is the normal modes of the precursor state, which allows the initial state to be accurately described thus allowing for the determination of the spectral intensity for a given eigenstate.<sup>38</sup>

Employing diabatic wave functions that are expanded as a sum of the multimode products and inserting them into the nonrelativistic Hamiltonian, a working form of equations is obtained, shown here only for two states<sup>39</sup>

$$\begin{pmatrix} \mathbf{H}_{1,1}^{vib,nr} & \mathbf{H}_{1,2}^{vib,nr} \\ \mathbf{H}_{2,1}^{vib,nr} & \mathbf{H}_{2,2}^{vib,nr} \end{pmatrix} \begin{pmatrix} \mathbf{d}_1^f \\ \mathbf{d}_2^f \end{pmatrix} = E_k^{T,nr} \begin{pmatrix} \mathbf{d}_1^f \\ \mathbf{d}_2^f \end{pmatrix} \quad (2.30)$$

where

$$H_{\gamma,m;\gamma',m}^{vib,nr} = \left\langle \theta_m^\gamma(\mathbf{Q}) \left| H_{\gamma,\gamma'}^{d,0}(\mathbf{Q}) \right| \theta_{m'}^{\gamma'}(\mathbf{Q}) \right\rangle_{\mathbf{Q}} \quad (2.31)$$

and

$$H_{\alpha,\beta}^{d,0}(\mathbf{Q}) = \left\langle \Psi_\alpha^d(\mathbf{r}^{N^{el}}; \mathbf{Q}) \left| H^0 \right| \Psi_\beta^d(\mathbf{r}^{N^{el}}; \mathbf{Q}) \right\rangle_r \quad (2.32)$$

Each  $H^{vib,nr}$  represents a  $N^{vib} \times N^{vib}$  matrix. Since the quasidiabatic representation is used and the Hamiltonian is an  $N^{state} \times N^{state}$  symmetric matrix with matrix elements that are linear and quadratic functions of all the internal coordinates, it can be explicitly written through second order as<sup>39</sup>

$$\begin{aligned} H_{\alpha,\beta}^{d,0}(\mathbf{Q}) &= \left\langle \Psi_\alpha^d(\mathbf{r}^{N^{el}}; \mathbf{Q}) \left| H^0 \right| \Psi_\beta^d(\mathbf{r}^{N^{el}}; \mathbf{Q}) \right\rangle_r \\ &= E_\alpha^0(Q^0) \delta_{\alpha,\beta} + \sum_i V_i^{(1),\alpha,\beta} Q_i + \frac{1}{2} \sum_{i,j} V_{i,j}^{(2),\alpha,\beta} Q_i Q_j + \dots \end{aligned} \quad (2.33)$$

where  $N^{el}$  is the number of electrons and  $\mathbf{Q}$  is a set of normal coordinates.

A suitable  $H^{d,0}$  for spectral simulations is constructed using electronic structure data. The working equations that result are over determined, meaning that there are more equations than unknowns, and it is required that they be solved in a least squares sense. These working equations are the pseudo normal equations, with “pseudo” implying that these equations must be solved self-consistently.

Appropriate electronic data can be determined by expanding around the minimum energy point of conical intersection.<sup>38, 39</sup> Since this is a least squares system of equations,  $H^{d,0}$  can be improved by including data points from regions of interest on the potential energy surface.

Using equations 2.24 and 2.30 the amplitude for the transition reduces to<sup>36</sup>

$$A_f^I = \sum_{\gamma} \langle \Theta_{\gamma}^f(\mathbf{w}) | \mu^{\gamma,0} | \Theta_I^0(\mathbf{w}') \rangle \approx \sum_{m,\gamma} d_{\gamma,m}^f [\mu^{\gamma,0} o(\mathbf{m}, \mathbf{I})] = \mathbf{s}^{\dagger} \mathbf{d}^f \quad (2.34)$$

where

$$o(\mathbf{m}, \mathbf{I}) = \left\langle \prod_{i=1}^{N^{int}} \chi_{m_i}^{\alpha,i}(Q_i) \left| \prod_{j=1}^{N^{int}} \chi_{I_j}^{0,j}(Q'_j) \right. \right\rangle \quad (2.35)$$

and  $o(\mathbf{m}, \mathbf{I})$  is the vector of Franck-Condon factors of length  $N^{vib}$  with  $\mathbf{s}$  being the seed vector, which allows for the determination of the transition intensities.

Since  $H^{vib,nr}$  has such a large dimension, its diagonalization is computationally challenging and a Lanczos algorithm is employed.<sup>38</sup> In this approach, the eigenvalues of the large vibronic Hamiltonian matrix are determined by diagonalizing a smaller, tri-diagonal matrix that is constructed such that it approximates  $H^{vib,nr}$ .<sup>39</sup> The initial seed vector,  $\mathbf{s}$ , is also appropriately chosen to reproduce the line intensities and the elements of the tri-diagonal matrix are determined each iteration.

The initial step in the Lanczos procedure is to determine the seed vector, which corresponds to the ground vibrational state of the initial electronic state. Since  $H^{vib,nr}$  is a large but sparse matrix, the algorithm utilizes a preprocessing step to identify the location of non-zero matrix elements of the Hamiltonian.<sup>39</sup> Once the

Lanczos iterations begin, the product of the vibronic Hamiltonian with the current Lanczos vector is evaluated. Each matrix-vector multiplication simply involves looping over the non-zero elements for each non-zero potential term. The algorithm converges the extremal eigenvalues first then proceeds “inwards”.<sup>39</sup> Many of the first and second order coefficients will be zero if symmetry is exploited, which reduces the number of non-zero elements to be determined.

### F) Relativistic Contribution

The Breit-Pauli approximation is utilized to include the relativistic contribution in the electronic Hamiltonian.<sup>40,41</sup> This work is exclusively concerned with the spin-orbit contributions, which arise from the coupling of the orbital and the spin angular momentum associated with the electrons. The spin-orbit operator of the Breit-Pauli approximation ( $H^{so}$ ) includes the one electron, spin-orbit, and two electron, spin-same orbit and spin-other orbit, parts and has the form<sup>42</sup>

$$\begin{aligned}
 H^{so} &= \frac{-e^2}{2mc^2} \left[ \sum_{i,K} \frac{Z_K}{r_{K,i}^3} \mathbf{1}_i(\mathbf{K}) \cdot \mathbf{s}_i + \sum_{i \neq j} \left( \frac{\mathbf{r}_{ij} \times \mathbf{p}_i}{r_{ij}^3} \right) \cdot (\mathbf{s}_j + 2\mathbf{s}_j) \right] \\
 &= \sum_i \mathbf{h}_i^{so} \cdot \mathbf{s}_i + \sum_{i \neq j} \mathbf{h}^{soo}(i,j) \cdot (\mathbf{s}_j + 2\mathbf{s}_j) \quad (2.36)
 \end{aligned}$$

It is important to note that this interaction lifts the  $2S+1$  degeneracy arising from the spin multiplicity. Due to the large size of the expansion and the need for complex mathematics in treating the spin-orbit interaction, the relativistic eigenstates are expanded in the nonrelativistic eigenbasis with the additional specification of the spin quantum numbers. This is relevant because in the vibronic

coupling approximation, the nonrelativistic diabatic Hamiltonian matrix is unchanged when time reversal adapted electronic functions are used. Thus, the time reversal adapted electronic basis will be used. The antiunitary time reversal symmetry operator  $T$  is utilized, where  $\hat{T}\Psi_k^{T,nr,+} = \Psi_k^{T,nr,-}$ . The time-reversal basis is used because it simplifies the treatment of the spin-orbit interaction.<sup>39</sup> The form of the eigenstates, for  $M_s = \pm 1/2$ , is

$$\Psi_\alpha^{d,\pm} = \frac{\pm 1}{\sqrt{2}} (\Psi_\alpha^{d,1/2} \pm i\Psi_\alpha^{d,-1/2}) \quad (2.37)$$

The eigenstates of  $H^{T,nr}$  can then be written as

$$\Psi_f^{T,nr,p}(\mathbf{r}^{N^{el}}; \mathbf{Q}) = \sum_{m,\alpha} \Psi_\alpha^{d,p}(\mathbf{r}^{N^{el}}; \mathbf{Q}) d_{\alpha,m}^f \prod_{i=1}^{N^{int}} \chi_{m_i}^{\alpha,i}(Q_i), \quad p = \pm \quad (2.38)$$

The nonrelativistic energies are independent of  $p$  and the states will come in degenerate pairs. These pairs are called Kramers' doublets,  $(\Psi_m^{T,so}, \hat{T}\Psi_m^{T,so})$  and are expressed as

$$\Psi_m^{T,so} = \sum_{\substack{p=\pm \\ k=1-N^{el}g}} c_{p,k}^m \Psi_k^{T,nr,p} \quad (2.39)$$

The total nuclear-electronic Hamiltonian including the spin orbit coupling in equation 2.36 is shown below along with the relativistic electronic-nuclear Schrodinger equation.<sup>39</sup>

$$H^{T,so} = T^{nuc} + H^0(\mathbf{r}; \mathbf{Q}) + H^{so}(\mathbf{r}; \mathbf{Q}) \quad (2.40)$$

$$(H^{T,so} - E_m^{T,so})\Psi_m^{T,so} = 0 \quad (2.41)$$

Using the approximation that interactions with other nonrelativistic electronic wave states is neglected, the matrix elements  $\langle \Psi_f^{T,nr,z} | H^{so} | \Psi_l^{T,nr,z'} \rangle$



can be computed given<sup>42</sup>

$$\mathbf{H}^{e,so}(\mathbf{Q}) = \begin{pmatrix} 0 & iH_Y^{rso} & 0 & iH_Z^{rso} - H_X^{rso} \\ -iH_Y^{rso} & 0 & -iH_Z^{rso} - H_X^{rso} & 0 \\ 0 & iH_Z^{rso} - H_X^{rso} & 0 & -iH_Y^{rso} \\ -iH_Z^{rso} + H_X^{rso} & 0 & iH_Y^{rso} & 0 \end{pmatrix} \quad (2.42)$$

where

$$H_\lambda^{rso}(\mathbf{Q}) = i \left\langle \Psi_\alpha^{d,\frac{1}{2}} \left| \sum_{i=1}^{N^{el}} h_\lambda^{1-2}(\mathbf{r}_i; \mathbf{Q}) s_z(i) \right| \Psi_\beta^{d,\frac{1}{2}} \right\rangle_r, \quad \lambda = X, Y, Z \quad (2.43)$$

In the case where there is no dependence on  $\mathbf{Q}$ , the elements reduce to<sup>39</sup>

$$\left\langle \Psi_k^{T,nr,z}(\mathbf{r}, \mathbf{Q}) \left| H^{so} \right| \Psi_l^{T,nr,z'}(\mathbf{r}, \mathbf{Q}) \right\rangle = O_{k,l} H_{\alpha,z;\beta,z'}^{e,so} \quad (2.44)$$

where

$$O_{f,l} = \sum_m (d_{1,m}^f d_{2,m}^l - d_{2,m}^f d_{1,m}^l) \quad (2.45)$$

and  $|O_{f,l}|$ , which is referred to as a generalized Ham reduction factor, has the effect of reducing the net spin-orbit interaction and is less than one.

The relativistic electronic-nuclear Schrodinger equation, 2.41, which is complex and Hermitian, can be separated into the real and imaginary parts through diagonalization so<sup>39</sup>

$$\begin{pmatrix} \mathbf{E}^{T,nr} & \mathbf{H}_X^{A,so} & -\mathbf{H}_Y^{A,so} & -\mathbf{H}_Z^{A,so} \\ -\mathbf{H}_X^{A,so} & \mathbf{E}^{T,nr} & -\mathbf{H}_Z^{A,so} & \mathbf{H}_Y^{A,so} \\ \mathbf{H}_Y^{A,so} & \mathbf{H}_Z^{A,so} & \mathbf{E}^{T,nr} & \mathbf{H}_Z^{A,so} \\ \mathbf{H}_Z^{A,so} & -\mathbf{H}_Y^{A,so} & -\mathbf{H}_X^{A,so} & \mathbf{E}^{T,nr} \end{pmatrix} \begin{pmatrix} \mathbf{c}_+^{m,R} \\ \mathbf{c}_-^{m,R} \\ \mathbf{c}_+^{m,I} \\ \mathbf{c}_-^{m,I} \end{pmatrix} = E_m^{T,so} \begin{pmatrix} \mathbf{c}_+^{m,R} \\ \mathbf{c}_-^{m,R} \\ \mathbf{c}_+^{m,I} \\ \mathbf{c}_-^{m,I} \end{pmatrix} \quad (2.46)$$

where

$$\mathbf{c}_\pm^m = \mathbf{c}_\pm^{m,R} + i\mathbf{c}_\pm^{m,I} \quad (2.47)$$

The vector of spin-orbit coupling matrix elements is  $\mathbf{H}^{rso}=(\mathbf{H}_X^{rso}, \mathbf{H}_Y^{rso}, \mathbf{H}_Z^{rso})$ .

The energy and spectral intensity distribution depend only on  $|| \mathbf{H}^{rso} ||$ , which is independent of the orientation.

When deriving the spectral intensity distribution including the spin-orbit interactions, the method is similar to the nonrelativistic case, but caution must be used since the time-reversal adapted electronic basis is used. Due to the sudden approximation, there are two  $N^{el}+1$  wave functions that also contain the continuum orbital, which describes the photodetached electron, equations 2.48 and 2.49. There are  $N^{el}+1$  antisymmetrized products must be formed. The linear combinations of the spin-eigenfunctions are shown below.<sup>39</sup>

$$\Psi_m^{T,so,\alpha} = \sum_{\substack{p=\pm \\ k=1-N^{el}}} c_{p,k}^m \Psi_k^{T,nr,p}(\phi_m^c \alpha) \quad (2.48)$$

and

$$\Psi_m^{T,so,\beta} = \sum_{\substack{p=\pm \\ k=1-N^{el}}} c_{p,k}^m \Psi_k^{T,nr,p}(\phi_m^c \beta) \quad (2.49)$$

so

$$\Psi_m^{T,so,\pm} = \frac{1}{\sqrt{2}} \left( \Psi_m^{T,so,\alpha} \pm i \Psi_m^{T,so,\beta} \right) \quad (2.50)$$

Each of the wave functions shown above makes an independent contribution to the line intensity, which is given by<sup>39</sup>

$$2|A_{m,I}^{so}| = |\mu^{so,m,I,+}|^2 + |\mu^{so,m,I,-}|^2 \quad (2.51)$$

Assuming the electronic transition moment is independent of Q,

$$\mu^{so,m,I,\pm} = \sum_{f=1}^{N^{eig}} c_{\mp,f}^m \sum_{\mathbf{m}',\gamma} d_{\gamma,\mathbf{m}'}^f \mu^{\gamma,0} o(\mathbf{m}', I) \quad (2.52)$$

## REFERENCES

1. H. Matsui, Y.-F. Zhu, and E.R. Grant. *Laser Chem.* **16**, 151 (1996)
2. X. Xing, M.-K. Bahng, B. Reed, C. S. Lam, K.-C. Lau, and C. Y. Ng. *J. Chem. Phys.* **128**, 094311, (2008)
3. W. C. Wiley, and I.H. McLaren. *Rev. Sci. Instrum.* **26**, 1150 (1955).
4. W. A. de Heer, and P. Milani. *Rev. Sci. Instrum.* **62**, 670, (1991).
5. L.-S. Wang, H.-S. Cheng, and J. Fan. *J. Chem. Phys.* **102**, 24 (1995).
6. Zheng, W. PhD. Dissertaion, Johns Hopkins University, 2004.
7. Thomas, O. C. PhD. Dissertation, Johns Hopkins University, 2001.
8. P. Kruit, and F. H. Read. *J. Phys. E Sci. Instrum.* **16**, 313, (1983).
9. A. Szabo and N. S. Ostlund. *Modern Quantum Chemistry: Introduction to Advanced Electronic Structure Theory*, *Dover Pub.* (1996).
10. W. Domcke and D. R. Yarkony. *Ann. Rev. Phys. Chem.*, **63**, 325 (2012).
11. W. Domcke, D. R. Yarkony, and H. Köppel, eds. *Conical Intersections: Electronic Structure, Dynamics & Spectroscopy*, *World Scientific, Adv. Ser. Phys. Chem.*, **15** (2004).
12. S. Matsika and P. Krause. *Ann. Rev. Phys. Chem.*, **62**, 621 (2011).
13. J. von Neumann and E. Wigner. *Physik.* **30**, 467 (1929).
14. C. A. Mead. *J. Chem. Phys.*, **70**, 2276 (1979).
15. D. R. Yarkony. *Modern Electronic Structure Theory I*, *World Scientific*, 642 (1995).
16. C. J. Ballhausen and A. E. Hansen. *Ann. Rev. Phys. Chem.*, **23**, 15 (1972).
17. G. A. Worth and L. S. Cederbaum. *Ann. Rev. Phys. Chem.*, **55**, 127 (2004)
18. M. Dallos, H. Lischka, R. Shepard, D. R. Yarkony, and P. G. Szalay. *J. Chem. Phys.*, **120**, 7730 (2004).
19. W. Domcke, D. R. Yarkony, and H. Köppel, eds. *Conical Intersections: Electronic Structure, Dynamics & Spectroscopy*, *World Scientific, Adv. Ser. Phys. Chem.*, **15** (2004).
20. K. Ruedenberg and G. J. Atchity. *J. Chem. Phys.*, **99.5**, 3799 (1993).
21. W. Domcke, D. R. Yarkony, and H. Köppel, eds. *Conical Intersections: Electronic Structure, Dynamics & Spectroscopy*, *World Scientific, Adv. Ser. Phys. Chem.*, **15**

- (2004).
22. H. Köppel. *Adv. Ser. Phys. Chem.*, **15**, 175 (2004).
  23. L. S. Cederbaum, H. Köppel, and W. Domcke. *Int. J. Quant. Chem. Symp.*, **15**, 251 (1981).
  24. X. Zhu and D. R. Yarkony. *J. Chem. Phys.*, **132**, 104101:1-15 (2010).
  25. X. Zhu and D. R. Yarkony. *Molecular Phys.*, **108**, 2611 (2010).
  26. D. R. Yarkony. *J. Chem. Phys.*, **112**, 2111 (2000).
  27. W. Domcke and D. R. Yarkony. *Ann. Rev. Phys. Chem.*, **63**, 325 (2012).
  28. W. Domcke, D. R. Yarkony, and H. Köppel, eds. Conical Intersections: Theory, Computation, Experiment, *World Scientific, Adv Ser. Phys. Chem.*, **17** 1-115 (2011)
  29. S. Matsika and P. Krause. *Ann. Rev. Phys. Chem.*, **62**, 621 (2011).
  30. D. R. Yarkony. *Rev. Mod. Phys.*, **68**, 985 (1996).
  31. D. R. Yarkony. *Acc. Chem. Res.*, **31.8**, 511 (1998).
  32. W. Domcke, D. R. Yarkony, and H. Köppel, eds. Conical Intersections: Electronic Structure, Dynamics & Spectroscopy, *World Scientific, Adv. Ser. Phys. Chem.*, **15** (2004).
  33. M. R. Manaa and D. R. Yarkony. *J. Chem. Phys.*, **99**, 5251 (1993).
  34. W. Domcke, D. R. Yarkony, and H. Köppel, eds. Conical Intersections: Theory, Computation, Experiment, *World Scientific, Adv Ser. Phys. Chem.*, **17** (2011).
  35. M. Döscher, H. Köppel, and P. G. Szalay, *J. Chem. Phys.*, **117**, 2645 (2002).
  36. S. Mahapatra, V. Vallet, C. Woywod, H. Köppel, and W. Domcke. *Chem. Phys.*, **304**, 17 (2004).
  37. A. Hazra and M. Nooijen, *J. Chem. Phys.*, **122**, 204327 (2005); A. Viel and W. Eisfeld. *J. Chem. Phys.*, **120**, 4603 (2004).
  38. M. S. Schuurman, D. E. Weinberg, and D. R. Yarkony. *J. Chem. Phys.*, **127**, 104309 (2007).
  39. M. S. Schuurman and D. R. Yarkony. Conical intersections: Theory, Computation, and Experiment, *Adv. Ser. Phys. Chem.*, **17**, 197-248 (2011).
  40. D. R. Yarkony. *Int. Rev. Phys. Chem.*, **11**, 195 (1992).
  41. D. R. Yarkony, ed. Modern Electronic Structure Theory I and II, *World Scientific*

- (1995).
42. D. R. Yarkony. *J. Chem. Phys.*, **84**, 2075 (1986).
43. R. A. Young, and D.R. Yarkony. *J. Chem. Phys.* **125**, 234301 (2006)
44. Goyal, S., Schutt, D. L., Scoles, G. *Phys. Rev. Lett.* **73**, 2512 (1994)
45. B. M. Elliot, R. A. Relph, J. R. Roscioli, J. C. Bopp, G. H. Gardenier, T. L. Guasco, M. A. Johnson. *J. Chem. Phys.* **129**, 094303 (2008)
46. M. Hartmann, R. E. Miller, J. P. Toennies, and A. Vilesov. *Phys. Rev. Lett.* **75**, 1566 (1995)

## **CHAPTER 2: EXPERIMENTAL ANION PHOTOELECTRON SPECTROSCOPY**

## I. Introduction

The overall goal is to obtain photoelectron spectra. Thus, ions and clusters must be created in a reliable ion source, mass selected, and then crossed with a fixed-frequency photon beam in an interaction region. With the apparatus now having the ability to accommodate an additional ion source, the versatility of the apparatus was greatly expanded. Unfortunately, this led to the necessity of unforeseen modifications and revealed the previous shortcomings that needed to be overcome. Once the electrospray ionization (ESI) source was working, it became immediately clear that the vacuum system would have to be modified because the previous system was not able to adequately accommodate the buffer gas being dosed into the ion trap, while also producing an intense, reliable ion beam. The ESI source further revealed that the previous time-of-flight (TOF) mass spectrometer could not sufficiently accommodate the ESI ion beam due to the transverse ion energy being higher. The ions being ejected from the ion trap of the ESI source have approximately 10 eV of transverse energy entering the TOF extraction region, while ions from a chamber zero source, such as a laser vaporization source, only have approximately 2 eV of transverse energy entering the TOF extraction region. The disparity between the two source sides of the apparatus was resolved by modifying and replacing the TOF optics.

While the photoelectron spectrometer region seemingly worked sufficiently well before, it was most likely due to the samples being used, which were mostly metal clusters samples. Such metal species are advantageous because they have a higher cross section, and they usually fall no higher than in the third harmonic



energy range. However, when the samples were expanded to inorganic and organic samples, higher energies are required, and fourth harmonic and excimer energies must be used, though they do exhibit more noise. Furthermore, the materials inside the interaction chamber become problematic, since their photoelectric work function could be exceeded in such energy ranges. When the fourth harmonic and excimer energies were used in the previous setup, the noise was too significant to collect an adequate spectrum, thus requiring an adaptation of the light baffles. This was most likely due to stray photons causing a significant amount of electron noise.

This chapter will discuss in detail the additions and modifications that have been made over the years to the apparatus, which were performed in order to enhance and expand its functionality. The extensive renovations will be discussed in terms of the different regions on the apparatus. The first substantial build project was adding a novel electrospray ionization source (ESI) to the machine; this will be detailed in the first section. The ESI source was additionally fitted with a purge chamber, so that air sensitive samples can be accommodated; a cryostat to cool the ion trap was also added. The addition of the cryostat has many advantages including improved spectral resolution and the potential to react species inside the trap. The next stage of major maintenance discussed relates to the modifications made to the overall vacuum system. This will be followed by a discussion of the alterations made to the time-of-flight (TOF) mass spectrometer region, which include augmented deflectors and Einzel lenses. Finally, the last substantial build project was to refabricate and align the light baffles in the interaction region. The general

schematic for the apparatus has already been introduced in chapter one. The figure below shows a reference of the chamber labels.

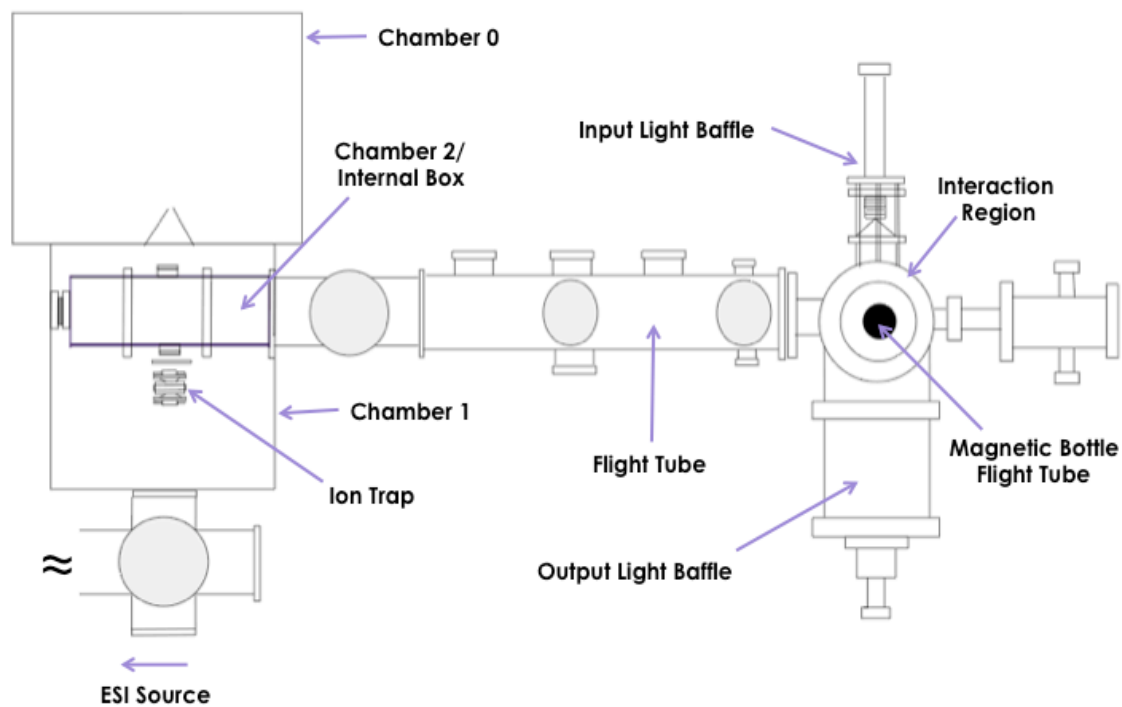


Figure 2.1: Schematic of the overall apparatus from a top view. Chamber 1 has been drawn as if the top were removed so that chamber 2, also referred to as the internal box, can be seen. The ion trap, which is located in chamber 1 and can be thought of as the terminal point of the ESI source, is shown.

## II. Sources

As previously stated, the experimental apparatus here is able to accommodate a variety of sources. The machine can be thought of as having two source sides. Both sources ultimately end up in the center of the extraction plates and are located directly across from each other on either side of the extraction region. On one side is chamber zero, where the laser vaporization source and PACIS source are run. The other side is the ESI side. It is important to note that there is a

shutter located in chamber 1 to protect the ion trap when the chamber 0 side is running. This section will succinctly discuss the laser vaporization and PACIS chamber 0 sources as well as an in depth survey of the ESI source.

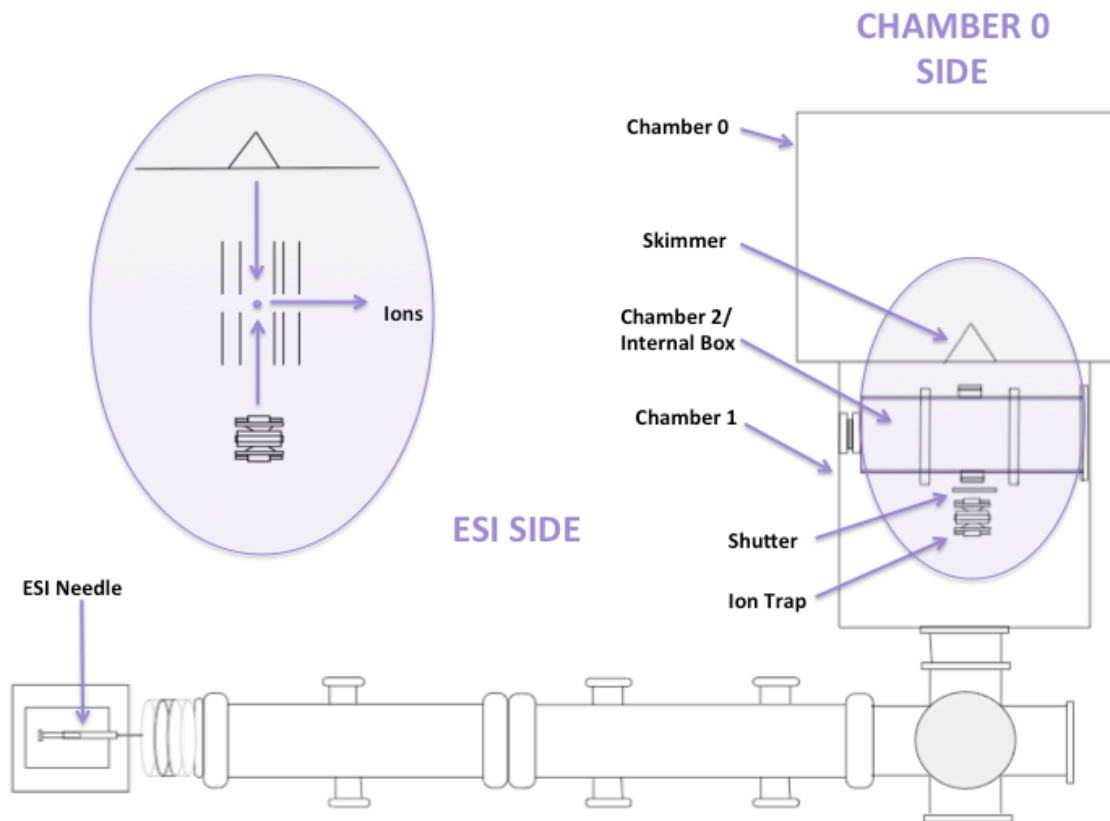


Figure 2.2: Schematic of the two source sides of the machine from a top view. The shaded enclosed area is shown to the side and portrays how the two sources are both aligned to transport ions to the center of the extraction plates. The enclosed area does not include the shutter, which is closed when the chamber 0 sources are running to protect the trap. When it is closed, ions fabricated in the ESI source will never make it to the extraction region.

### A. Laser Vaporization

In the laser vaporization source, a sample rod is located in a specially designed holder that is in-line with the gas flow from a general purpose valve

operating at 10 Hz. A pulsed Nd:YAG laser (532 nm, 10 Hz) is used as the vaporization laser, which is focused onto the surface of the sample rod, and is employed to ablate material off the simultaneously rotating and translating sample rod creating electrons from photoemission. The incorporation of the sample as a rotating and translating rod ensures a fresh metal surface is supplied avoiding deep cuts by the laser. The ablation process produces a hot plasma, so collisional cooling is crucial to promote cluster growth. In this process, the neutral and ionized metal atoms as well as electrons are ejected forming a metal plasma. Negative ions are then created by electron attachment between the neutral molecule and the photoemission produced electrons resulting from collisions in the helium jet expansion.

Supersonic nozzle sources provide the most rapid and efficient collisional cooling. Helium is typically the expansion gas of choice because, when considering the typical velocity of the gas and spatial dimensions of the nozzle, helium moves faster and will undergo more collisions with the ablated material.<sup>1</sup> After the vaporization laser pulse, the growth channel keeps the metal vapor and collision gas confined allowing cluster condensation. The gas will finally expand from the end of the growth channel and a skimmer is utilized to collimate the beam as it leaves the source chamber. In this source, cluster growth is believed to occur by three-body collisions occurring in a sequential process after the vaporization of the atoms.<sup>1</sup>

The performance of this source is determined by the variables: the specific expansion gas used and its backing pressure in the valve, the pulse energy of the vaporization laser and how well it is focused, the dimensions of the growth channel

in the nozzle, and the temporal duration of the gas pulse in relation to the laser pulse. The main parameters in the design of the nozzle are the length of the growth channel and its diameter. Both the nozzle parameters and experimental variables must be optimized for each sample. The ablation laser is typically realigned before each experiment.

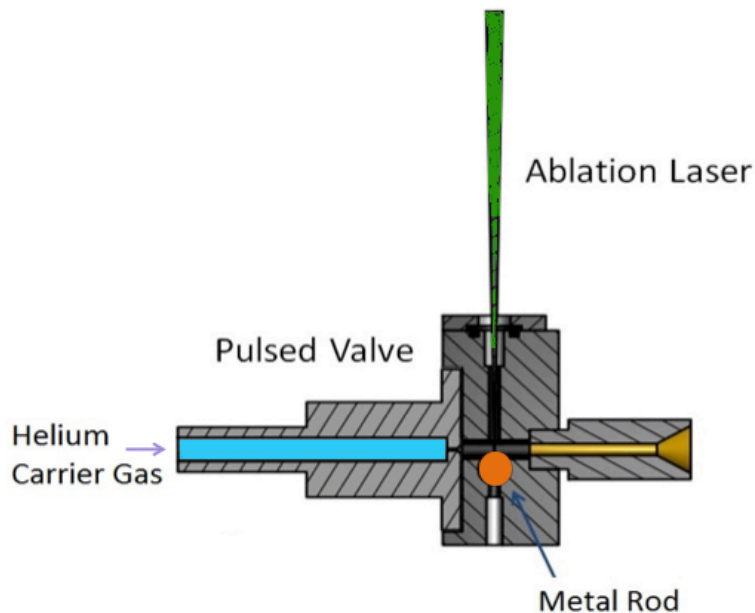


Figure 2.3: Schematic of the laser vaporization source.

## B. PACIS

The pulsed arc cluster ionization source (PACIS)<sup>2</sup> is particularly suited to creating metal hydride ions. Metallic cluster and metal hydrides are generated with a 30 microsecond long, 150 V electrical discharge from an anode, usually copper, to a metal cathode while simultaneously flowing hydrogen carrier gas from a pulsed valve over the discharge region. The discharge produces a high density region of free metal atoms, electrons, and hydrogen atoms. The plasma that is created is cooled in the gas expansion down the extender tube, forming clusters as the jet

condenses. It is important to note that this source is limited to conductive samples, primarily metals.

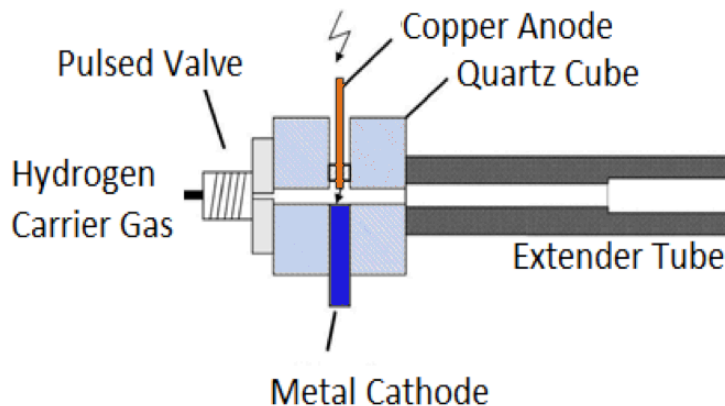


Figure 2.4: Schematic of the pulsed arc cluster ionization source (PACIS).

### C. Electrospray Ionization Source

The electrospray ionization source (ESI) is the newest source addition and vastly expands the capabilities of the apparatus. It has long been desirable to put complex and relatively nonvolatile molecules into the gas phase without decomposition.<sup>3</sup> However, a major stumbling block in performing spectroscopic analysis on liquid systems was the difficulty of transforming large, complex, fragile, or otherwise nonvolatile species into the gas phase intact. The ESI source is unique in that it readily provides intact ions in the gas phase from liquid, nonvolatile species. It is important to note that only species existing in the liquid solution are found as gas phase ions and the observed species are intact anions and intact anions with unionized solvent or solute molecules attached.<sup>3,4</sup> The liquid that emerges from the needle is dispersed in a fine spray of droplets, and as it travels, the droplets

evaporate leaving intact, desolvated ions and clusters. The ESI source is intrinsically continuous.

The ESI source generally operates to produce ions at atmospheric pressure by spraying a solution through a needle floated at high voltage to produce a fine spray. The ions are then drawn into a desolvation chamber through hydrodynamic flow. The ions pass through skimmers, a series of lenses, differential apertures, and ion guides ultimately to a 3D Paul trap. In the ion trap, the ions can be stored for a variable period of time before being extracted in order to increase the duty cycle. Since the ultimate goal is to pass the ESI generated ions into the time-of-flight (TOF) mass spectrometer for mass selection and onto the magnetic bottle photoelectron spectrometer (PES), the ESI source must be integrated into these pulsed regions. This is easily facilitated with the ion trap since the ions can be trapped for a tunable amount of time and then extracted at a 10 Hz repetition rate.<sup>5-8</sup> On the apparatus the ion trap has the added advantage of being cooled to liquid nitrogen temperatures, which results in cold anions that have better resolved photoelectron spectra due to the elimination of vibrational hot bands.

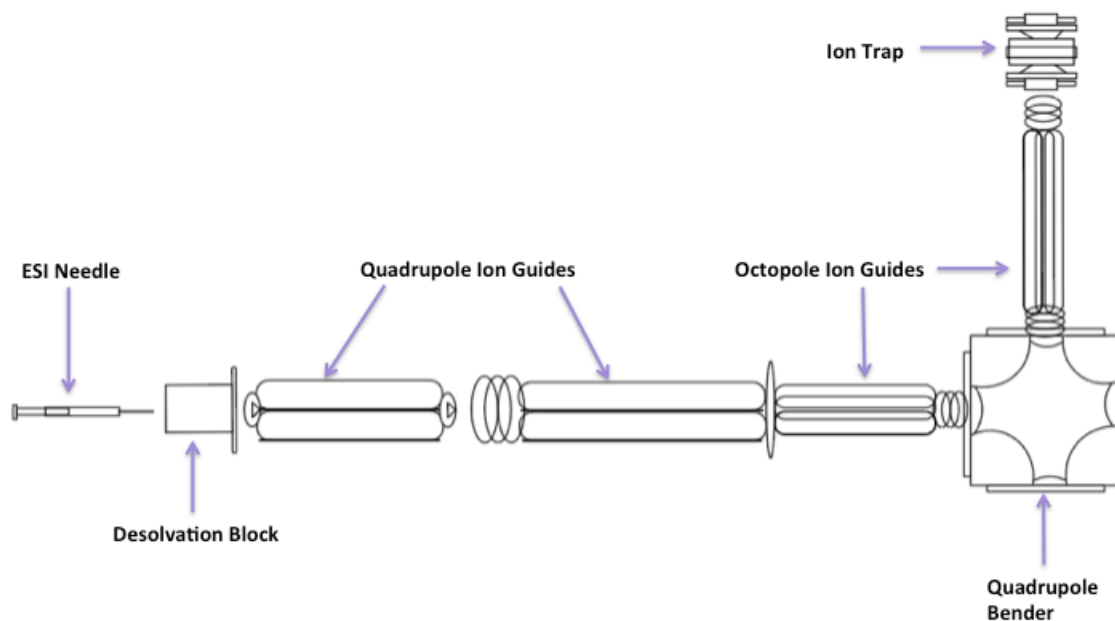


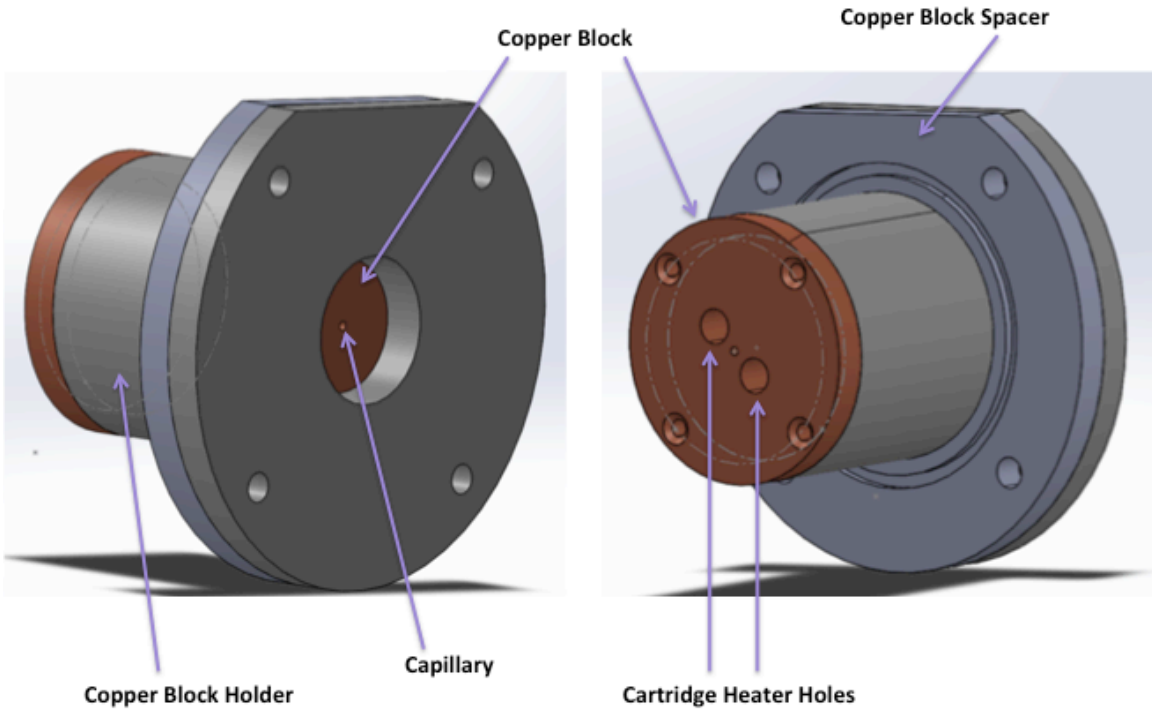
Figure 2.5: This illustrates the general schematic of the electrospray ionization source in which the imperative components are labeled.

The ESI source starts by dispensing a liquid sample through a 22 gauge, stainless steel, gastight LTN (Luer tip cemented) needle from Hamilton Company (Reno,NV) , fitted with a fused silica tubing tip that has been pulled to a 1-15  $\mu\text{m}$  inner diameter. The fused silica tip is first gently placed into a MicroTight® sleeve, 0.025" outer diameter x 0.009" inner diameter, IDEX Health & Science (Middleborough, MA), then both are placed into MicroTight® coned nut sized to fit the sleeve. An equivalent coned nut is place on the stainless steel needle as well. A MicroTight® union assembly is then used to connect the needle coned nut end and the fused silica tip coned nut end together. MicroTight® adapters, unions, and fittings are used because they create zero dead volume, allowing for an uninterrupted fluidic path between tubing of different sizes. The liquid samples are

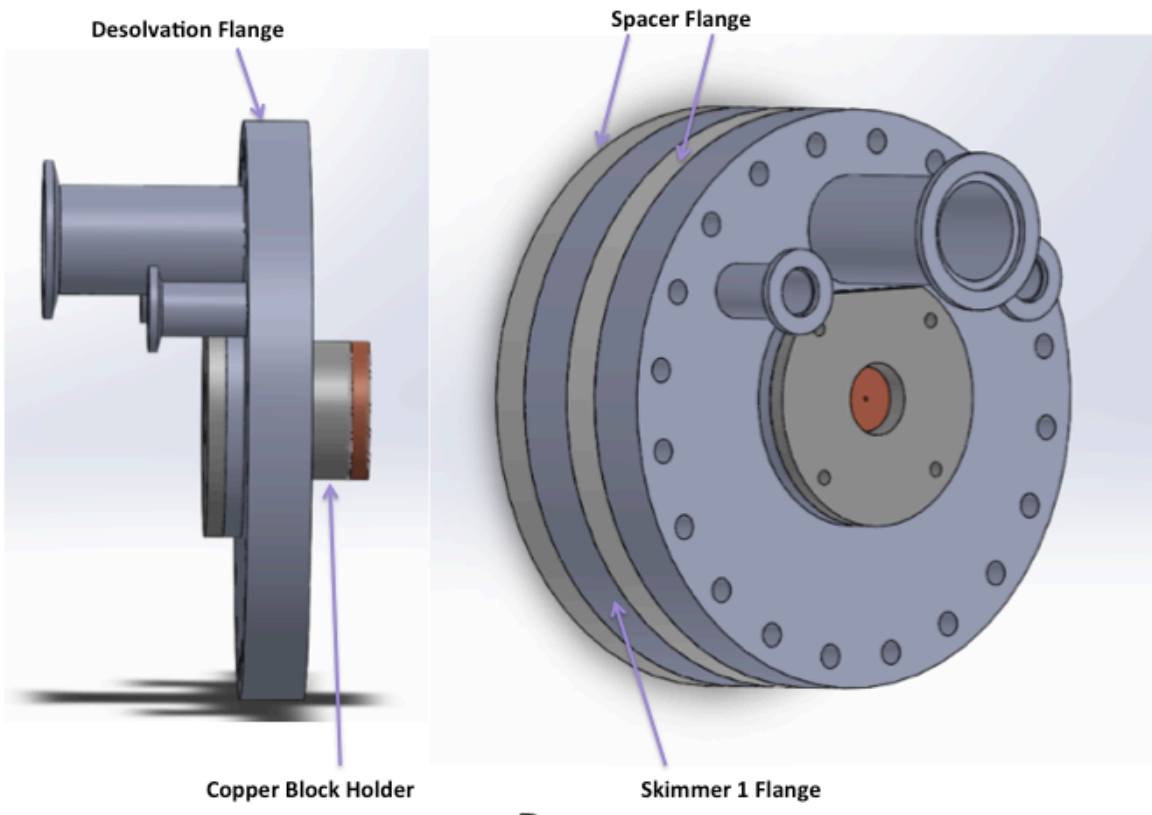


dilute in solute concentration with the solvent being 50:50 mixture of a volatile solvent, such as methanol, with water, since it has the ability to dissolve a wider range of solutes, especially those that are biological. A high voltage of a few thousand kilovolts is applied to the stainless steel needle tip, the polarity of which depends on the polarity of ions desired. A Harvard Apparatus '22' standard infusion syringe pump, Harvard Apparatus (Holliston, MA), was utilized here to control the flow rate. Typically, the flow rate is approximately 3.00  $\mu\text{l}/\text{min}$ , though it should be adjusted to optimize the ion signal. The magnitude of the high voltage applied will determine the droplet size and composition. Care must be taken not to turn the voltage up enough to cause fragmentation. The needle and syringe pump of the ESI source is located at atmosphere. They are positioned in an enclosed box, facilitating humidity control.

A spray or aerosol is created by the application of the high voltage and is drawn into the desolvation block by hydrodynamic flow. The desolvation block here is a copper piece fitted with a capillary in the center that is heated with two cartridge heaters fitted directly into the block. In the heated capillary, the droplets are desolvated, or the solvent evaporates, leaving intact ions and clusters. Figure 2.6 below shows the desolvation block.



**A**



**B**

Figure 2.6: **A)** This schematic depicts the copper block with the heated capillary. The copper block is held in the copper block holder and there is a spacer made of Teflon. The back view shows the holes in which the cartridge heaters are placed. **B)** This schematic depicts the copper block in the desolvation flange and the three other flanges, two spacer flanges and the skimmer 1 flange, that are used to hold the copper block in place. The entire assembly bolts on the first quadrupole chamber.

The desolvated ions then pass through a first skimmer, into the first ion guide, which is a radio frequency (rf) quadrupole, followed by a second skimmer. At this point on the apparatus there is a VAT valve, which separates the desolvation block, the first skimmer, the first quadrupole ion guide, and the second skimmer from the rest of the ESI ion guides, lenses, quadrupole bender, and ion trap. This valve ensures protection of the higher vacuum regions in case of accidents. The conditions of the needle, including the block temperature and the voltage applied, the first two skimmers, and the first quadrupole are critical to controlling the size of the droplets produced and transmitted. Their voltages should be optimized for desolvation and the transmission of bare anions. Moreover, in order to transmit ions for TOF mass spectroscopy, the needle and desolvation block conditions must be stable and the dc floats and peak-to-peak rf voltages optimized.

After the second skimmer, there is a three element lens denoted as the plate lens. Similar to the Einzel lenses in the TOF mass spectrometer region, matching voltage is applied to the first and third elements while voltage can be separately applied to the second element. After the plate lens is the second rf quadrupole ion guide and the first rf octopole ion guide. There is a small aperture between the quadrupole and the first octopole that assists with differential pumping. Another

smaller diameter three-element lens is located just after the first octopole ion guide to facilitate the ion beam transmission to the quadrupole bender. This lens is set up in the same fashion as the plate lens and the Einzel lenses with elements one and three receiving the same voltage and element two having a separate voltage. Figure 2.7 below shows the ESI source up to this point.

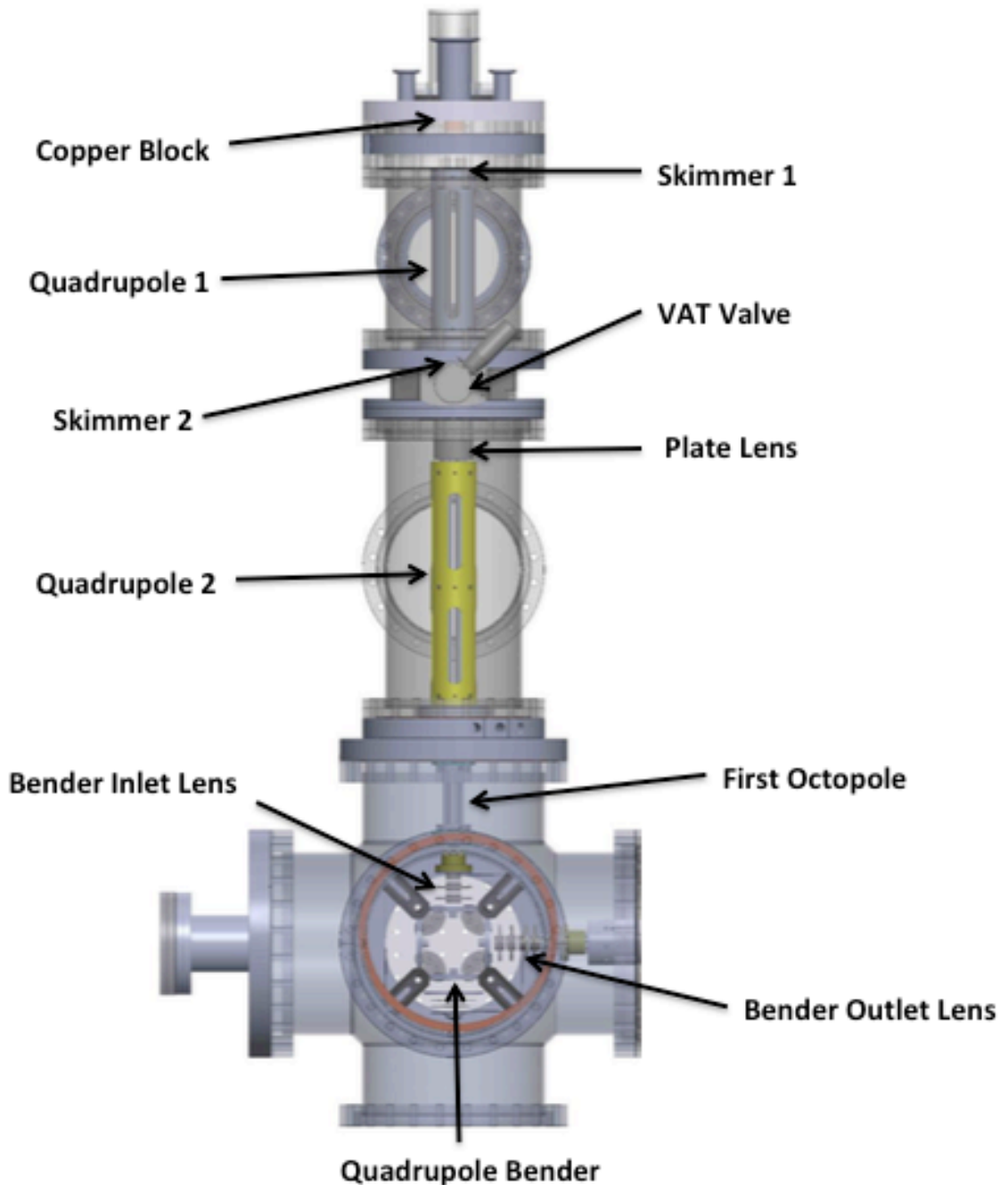


Figure 2.7: This schematic depicts a top view, close up of the ESI source before the ion beam is bent 90° towards the ion trap.

Since the ESI source was designed to attach to the existing TOF mass spectrometer and magnetic bottle PES, there were physical placement limitations. To ensure the source could fit in the space provided while leaving the existing regions of the apparatus unmoved, a quadrupole bender was employed so the ion beam created by the ESI source could be “bent” 90° in the direction of the ion trap, located adjacent to the extraction region. The quadrupole bender is set up such that element one and four have the same voltage and elements two and three have the same voltage. There are also apertures on the bender input side, immediately after the bender input three element lens, and on the bender output side, immediately before another three element lens that is denoted as the bender outlet lens. The bender outlet lens elements are of the same diameter as the bender inlet lens. The bender outlet lens elements have voltage applied in the same manner as the bender inlet lens. After the bender outlet lens there is a second rf octopole ion guide followed by another three element lens denoted as the last Einzel lens. As suggested in the name, this is an Einzel lens with identical voltage applied to the first and third lens elements, and separate voltage applied to the second element.

The series of rf quadrupole and octopole ion guides, the lenses, the bender, and the skimmers all function to guide the ion beam to the ion trap for storage and integration into the TOF mass spectrometer, and ultimately the magnetic bottle PES. The ESI source was originally setup such that it did not include cryogenic cooling of the ion trap. In this case, the ion trap was located immediately after the last Einzel

lens. Now, however, the ion trap is encased in a heat shield and attached to a liquid nitrogen cooled cold head of a cryostat. The details of the cryostat assembly will be further detailed below. It is important to note there is a shutter mounted on a manipulator with external control that is positioned between the ion trap and the ESI side of the internal box (chamber 2). The purpose of the shutter is to block the trap from the chamber 0 species. The shutter is a 0.048" thick stainless steel plate that is just thick enough to rigidly stand in place. If a non-conducting substance condenses on the electrode surface of the trap, a dielectric coating will form resulting in surface charge and causing distortions in the local field. If a conducting substance coats the insulators, leakage paths between the elements will be created. Such situations are indicated by the amount of power needed to adjust the amplitude of the RF peak-to-peak voltage increasing inconsistently.

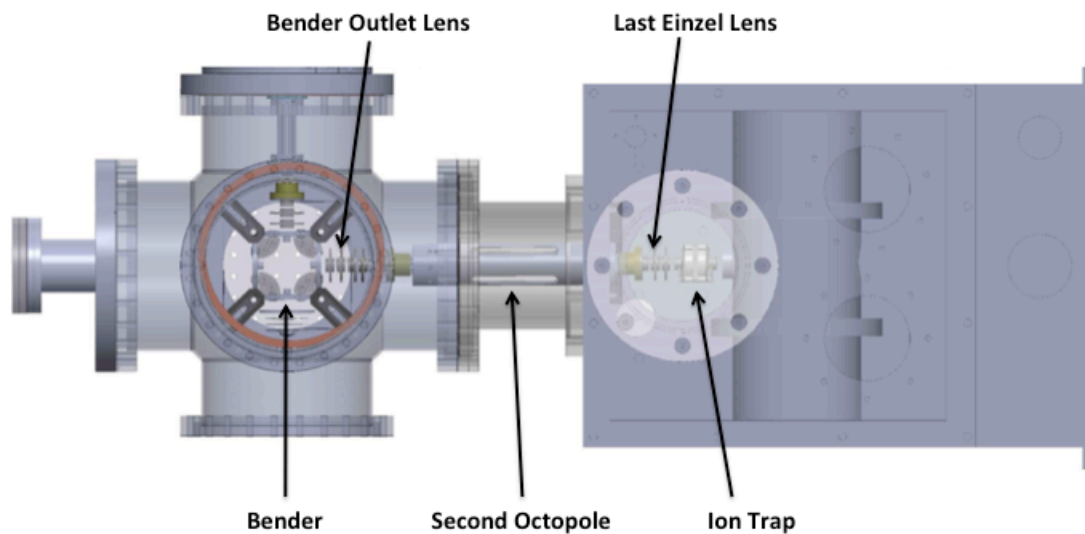


Figure 2.8: This schematic depicts a top view of the ion trap and ion optics after the ion beam is bent 90° towards the ion trap.

The quadrupole ion trap and its power supply are commercial products from R. M. Jordan (Grass Valley, CA). This 3D Paul trap confines the ions much like a point source, where the ions are confined both axially and radially. The ion trap in the apparatus is operated as a closed structure for use with a buffer gas. The ion trap is assembled by first mounting ceramic sleeves over 0-80 threaded rods, which act as supports for the ion trap. A tube lens is positioned before the entrance end cap to facilitate guiding the ion beam into the trap. Since this is operating in a closed mode, a ceramic ring is placed in between the entrance end cap rather than a just a ceramic spacer that is used in an open structure. There is another ceramic ring in between the ring electrode and the exit end cap. After the exit end cap there is another tube lens, which guides the ion beam exiting the ion trap to the extraction region. The buffer gas is continuously leaked in through a hole in one of the ceramic rings, with the flow rate controlled externally by a needle valve.

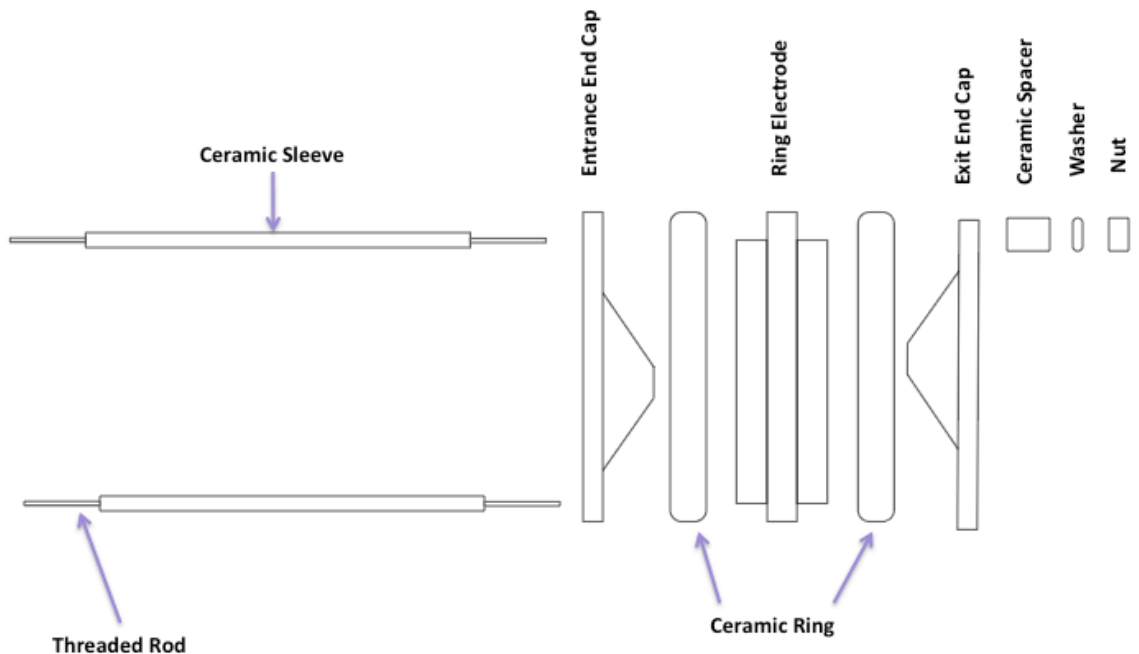


Figure 2.9: This schematic depicts an exploded view of the ion trap so the individual components are clear. It is run in a closed configuration so ceramic rings are used.

The ion trap operates at a frequency of 1 MHz with a peak-to-peak voltage of  $\sim 500\text{-}900$  V depending on the sample. The ion trap is not floated and is at ground relative to the last octopole, which has a DC float of  $\sim -14$  V. The ion packet that is extracted from the trap should diverge quickly; to mitigate this, a bipolar extraction scheme is used as well as the exit tube lens. To extract ions from the trap, the rf is turned off. After  $1.5\text{-}2$   $\mu\text{s}$ , to ensure the rf is indeed off, a negative pulse of  $\sim -80$  V is applied to the entrance end cap and a positive pulse of  $\sim +20$  V is applied to the exit end cap for  $15$   $\mu\text{s}$ . The ion trap runs at a 10 Hz repetition rate, indicating that the ion accumulation time is approximately 100 ms. The ions are ejected from the trap into the extraction region of the TOF mass spectrometer, where they are perpendicularly extracted down the TOF mass spectrometer axis. The ions are ejected with approximately 10 eV of transverse kinetic energy. It is important to note that, while the ion guides are able to transmit large droplets that the ESI source can produce, the ion trap has a mass range, the upper limit being approximately about 2000 amu.

The rf quadrupole and octopole ion guides are essential for the transmission of the ion beam to the 3D Paul trap. Under stable conditions, oscillatory electromagnetic fields are used to either transmit charged particles or to confine them into bounded regions of space.<sup>9</sup> The basic idea is that the ions experience a field gradient force, which is caused by the inhomogeneity of the field. The field gradient force is proportional to the square of the charge, is mass dependent, and is



independent of sign. This results in smooth motion that is independent of the starting phase. Adiabatic conservation of energy is used to deduce the transmission of the ions and depends only on their transverse energy and not on the individual initial conditions.<sup>9</sup> The operating conditions are calculated such that the adiabatic approximation remains valid everywhere within the boundaries defined by the electrode surfaces. With an added DC potential, additional boundary conditions are implied, and there must be slow adjustment of the DC and rf fields to obtain stable transmission conditions.<sup>9</sup> The transmission features depend on the position of the rf electrodes, and as such, must be taken into account during the design process. The ions usually stay near the centerline, and the ideal equipotential lines of multipole circular rods are equally spaced on an inscribed circle with radius  $r_0$ .<sup>9</sup> Moreover, these ion guides are designed such that the ions will not collide with the rods, resulting in an approximately 100% transmission efficiency. The inscribed circle for the ion guide rods were used to design the plate lens, bender inlet lens, bender outlet lens, and the last Einzel lens since these lenses are mounted directly off the ion guides. Also note, the bender inlet lens, bender outlet lens, and last Einzel lens were modified to all have the stainless steel spacers connected to ground using copper wire to avoid stray fields. For more specific information on the rf quadrupole ion guides, rf octopole ion guides, skimmers, and lenses, please refer to Evan Collins' thesis.

The ESI source physically spans multiple chambers on the apparatus. The desolvation block consists of a copper block positioned in a stainless steel block holder. This assembly, along with skimmer 1, is held together by a series of four

custom flanges that mount directly onto the chamber that houses the first rf quadrupole ion guide. The desolvation block assembly is directly pumped by a Leybold D90AC dual stage vacuum pump and the working pressure is 1.1 Torr. The first rf quadrupole is housed in its own T chamber that is pumped by a Leybold-Heraeus WS500 blower booster vacuum pump backed by a Leybold Trivac D40B two stage rotary vane vacuum pump and is kept in the 10-100s of mTorr. After the VAT valve, there is another, longer T chamber that primarily houses the second rf quadrupole ion guide and is pumped by a Pfeiffer TMU 260 turbomolecular pump. The first rf octopole ion guide, the bender inlet lens, the quadrupole bender, and the bender outlet lens are all completely housed in a six-way cross chamber, which is directly pumped by a Pfeiffer TMU 521 turbomolecular pump. A portion of the second rf octopole ion guide is positioned in the six-way cross chamber, but the majority of it is in an extender piece connecting the six-way cross chamber to chamber 1. The last Einzel lens and the ion trap, including when the ion trap is mounted on the cold head of the cryostat, are located in chamber 1, just before the internal box/chamber 2 that houses the TOF extraction region. The buffer gas is continuously bled into the ion trap and there is no way to directly measure the pressure in the trap. Instead, the overall pressure of the region is monitored, and the working pressure is approximately  $8.5 \times 10^{-6}$  Torr with the base pressure approximately  $2.0 \times 10^{-6}$  Torr. The working pressure in the interaction region, indicating that the buffer gas is on, is approximately  $8.0 \times 10^{-8}$  Torr, with a base pressure approximately  $3 \times 10^{-8}$  Torr.

## 1. Cryostat

The capability to control ion temperature, which is critical for gas phase spectroscopy, has been a challenge in chemical physics. Cold ions are desirable since vibrational hot bands are eliminated resulting in more resolved photoelectron spectra. The temperature of the ions produced in the ESI source should be around room temperature, because the desolvation block temperature is between 50-100°C. Since the anions are at room temperature, they carry a substantial amount of energy resulting in significant thermal broadening, limiting the spectral resolution. There are many methods currently employed to create cold ions including supersonic expansion, helium nanodroplets, and argon tagging.<sup>10-14</sup> Recent advances in ion trap technology have allowed for the production of cold ions by using the buffer gas as a thermal bath. Since the ion trap confines ions kinetically through the use of time varying electric fields, the ions can be thermalized internally and translationally via collisions with the buffer gas. Keeping this in mind, the ESI source was fitted with a cryogenically cooled ion trap to produce cold anions. This was accomplished by attaching the 3D Paul trap to the cold head of a liquid nitrogen cooled cryostat capable of reaching 77 K.

In order to integrate a cryostat into the existing apparatus, multiple design obstacles had to be overcome. The most critical was the decision of where to mount the cryostat on the apparatus. Fortunately, there is a port on the top of chamber 1 in the region of the ion trap that sufficed for this purpose. The second obstacle was the selection of the cryostat and the design of the critical components necessary for mounting the ion trap to the cold head of the chosen cryostat. The third obstacle

was to deduce a way in which to align the ion trap once it was mounted to the cold head of the cryostat. It is crucial to note that cooling the ion trap to liquid nitrogen temperatures can induce changes in the physical alignment of the assembly. Taking all these concerns into account, the LB-4T system built by Advanced Research Systems, Inc. (Macungie, PA) was chosen. This system was customized to include a custom sample plate and a custom radiation shield mount. A silicon diode from Lake Shore Cryotronics, Inc. (Westerville, OH) and a cartridge heater from Watlow (St. Louis, MO) were mounted in the sample plate by Advanced Research Systems, Inc. to allow temperature monitoring and control.

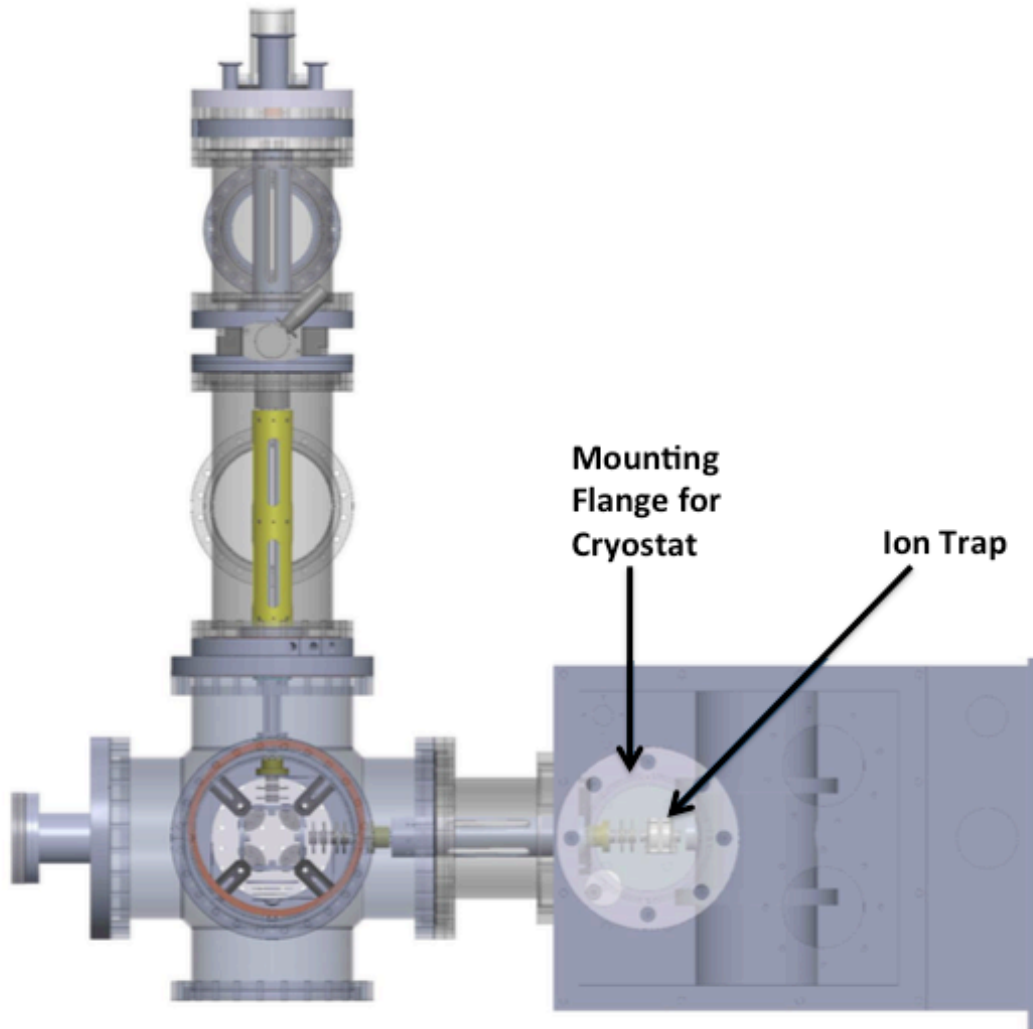


Figure 2.10: This schematic is a top view of the ESI source. The top port of chamber 1 that the cryostat is mounted on is shown. While the ion trap is located just below this port, it is clear that it is not quite center, resulting in the machining of an adapter ASA flange with a bore that is not centered.

The cryostat was designed to mount on a port on top of chamber 1 almost directly above the ion trap. A blank ASA flange was adapted to mount the cryostat on the chamber and needed to be customized, since the bore was not exactly centered, due to the location of the port on the chamber. Evidently, for the flange to

seal to the chamber and not leak when cooled to liquid nitrogen temperatures, an o-ring was required, which was greased with Apiezon N vacuum grease. A cluster flange, which houses all of the necessary electrical connections and buffer gas line, is mounted on top of the ASA flange. Next, there is a port aligner, which is the primary piece of the assembly that allows for alignment adjustments. The LT-4B cryostat is then mounted on top of the port aligner with a 2.75" rotatable conflat flange. The ASA adapter flange, cluster flange, port aligner, and the top of the LT-4B all exist outside chamber 1 at atmosphere. There is a custom cold tip flange made of oxygen free high purity copper (OFHC) attached to the bottom of the LT-4B, which houses a cartridge heater allowing for temperature control. An ion trap mounting flange and ion trap mount, both made of OFHC, were fabricated to facilitate mounting the ion trap to the cold tip flange. When removing the cryostat assembly for cleaning or maintenance, only the ASA flange is left on chamber 1. All of the component shown in figure 2.11 are mounted together and are removed together.

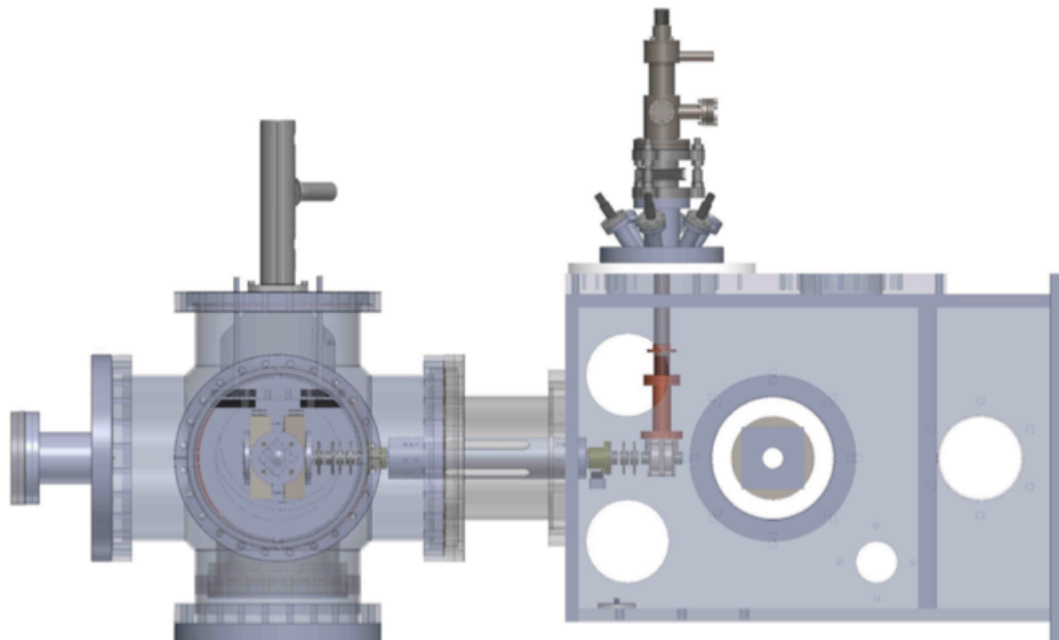


Figure 2.11: This schematic is a side view of the apparatus illustrating how the ion trap mounts to the bottom of the cold head of the liquid nitrogen cooled LT-4B cryostat. In this schematic, the heat shield and two apertures are not present.

A Shapal Hi-M Soft™ plate, Precision Ceramics USA, Inc. (Tampa, FL), was custom fabricated for placement in between the ion trap mount and the ion trap. Shapal Hi-M Soft™ is a hybrid material, composed of aluminum nitride and boron nitride, blended and sintered to form a dense ceramic. It has high thermal conductivity, high mechanical strength allowing it to be easily machined, and a very low coefficient for thermal conductivity. As such, it has exceptional electric insulation and high heat resistance. Due to its thermal conductivity and electrical insulation properties, it was chosen over a sapphire plate that is used in similar setups.<sup>8</sup> Both the Shapal Hi-M Soft™ plate and ion trap are mounted to the ion trap mount using 0-80 threaded rods. There were already 0-80 tapped holes in the end cap pieces of the trap, facilitating its mounting onto the ion trap mount. The ion trap is encased in a heat shield that has tunable apertures mounted to it. The heat shield is composed of three parts and is made of aluminum (due to cost). At the top, there is a heat shield adapter plate cut down the center with a small width saw to facilitate the electrical connections, especially those of the cartridge heater and silicon diode. This piece mounts directly onto a custom radiation shield mount, which is part of the LT-4B. There is a heat shield extension piece that connects to the heat shield adapter plate at the top and to the heat shield bottom. The heat shield bottom is designed such that it slides over the top with a space on each face to mount the cryostat apertures, which are made of stainless steel. While the heat shield assembly

fit together almost perfectly, an ultrathin aluminum spacer was additionally fabricated that has an outer diameter of 3.625", the same outer diameter as the rest of the heat shield assembly, and a bolt circle with thru holes that match the bottom of the heat shield extension and the top of the heat shield bottom. The addition of this ultrathin spacer ensured that the ion trap did not touch the bottom of the heat shield bottom piece of the assembly.

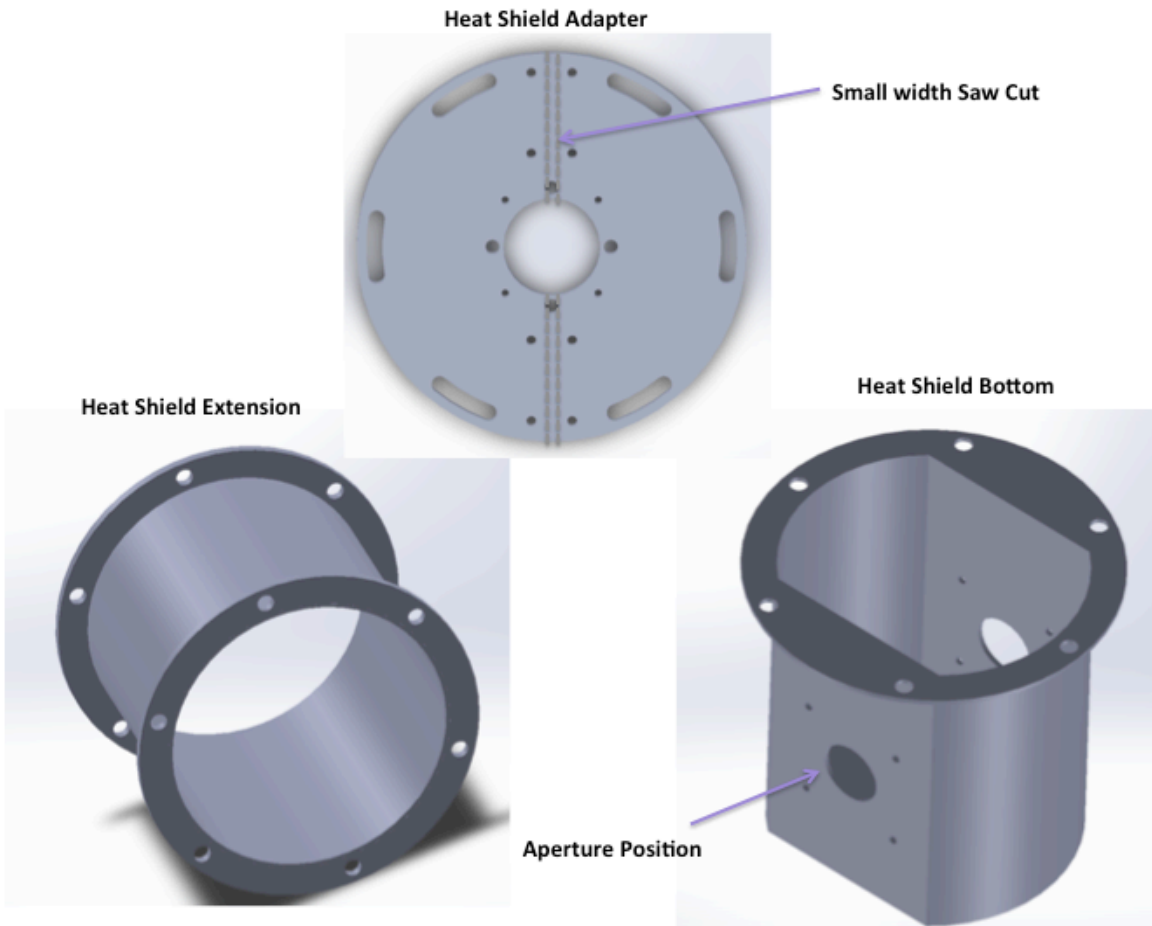


Figure 2.12: This is a schematic of the heat shield assembly. The heat shield adapter plate is connected directly to the LT-4B cryostat assembly by mounting onto the custom radiation shield mount. Two tunable, stainless steel apertures mount onto the heat shield bottom. There is a place to mount a pulse valve on the heat shield bottom.



While the cryostat was initially designed to have a pulse valve, which would mount to the bottom of the heat shield bottom, experimentation was done and it is better, both in terms of signal and pumping adequacy, to run continuously. The temperature of the cryostat is controlled and monitored by a control board obtained from the Instrument Development Group at Johns Hopkins University (Baltimore, MD). It is also desirable to be able to controllably heat up the cryostat in order to prevent electrical shortages. It is important to note that the surfaces were greased using Apiezon N Grease, M&I Materials (Manchester, UK), which is a cryogenic high vacuum grease.

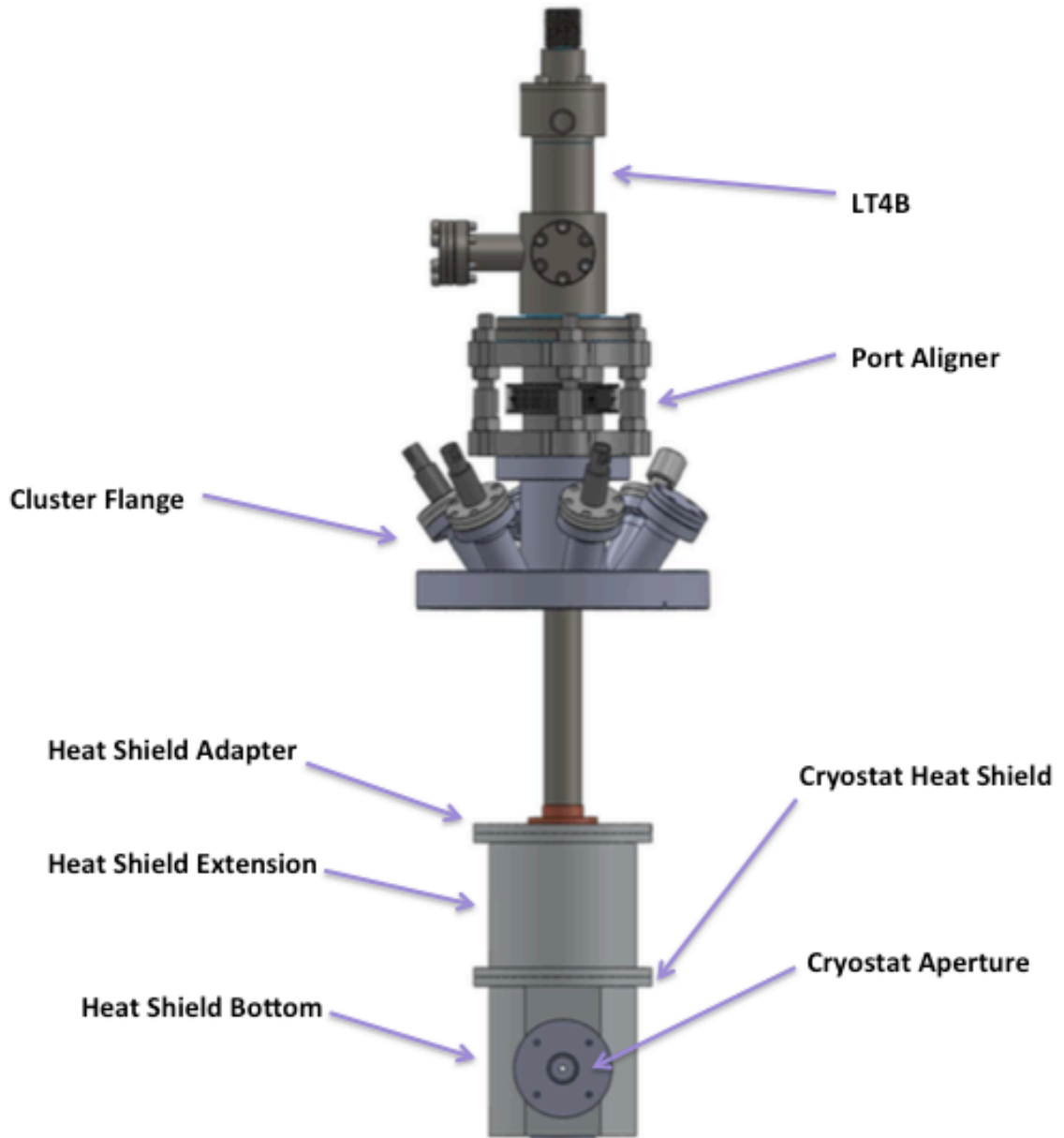


Figure 2.13: This is a schematic of the cryostat assembly. The LT-4B cryostat is mounted on top of a port aligner, which facilitates positional adjustments necessary when the ion trap is cryo-cooled, which bolts to the cluster flange housing the electrical and buffer gas connections. The cryostat heat shield is shown as mounted to the custom radiation shield mount and has apertures mounted on the bottom assembly.

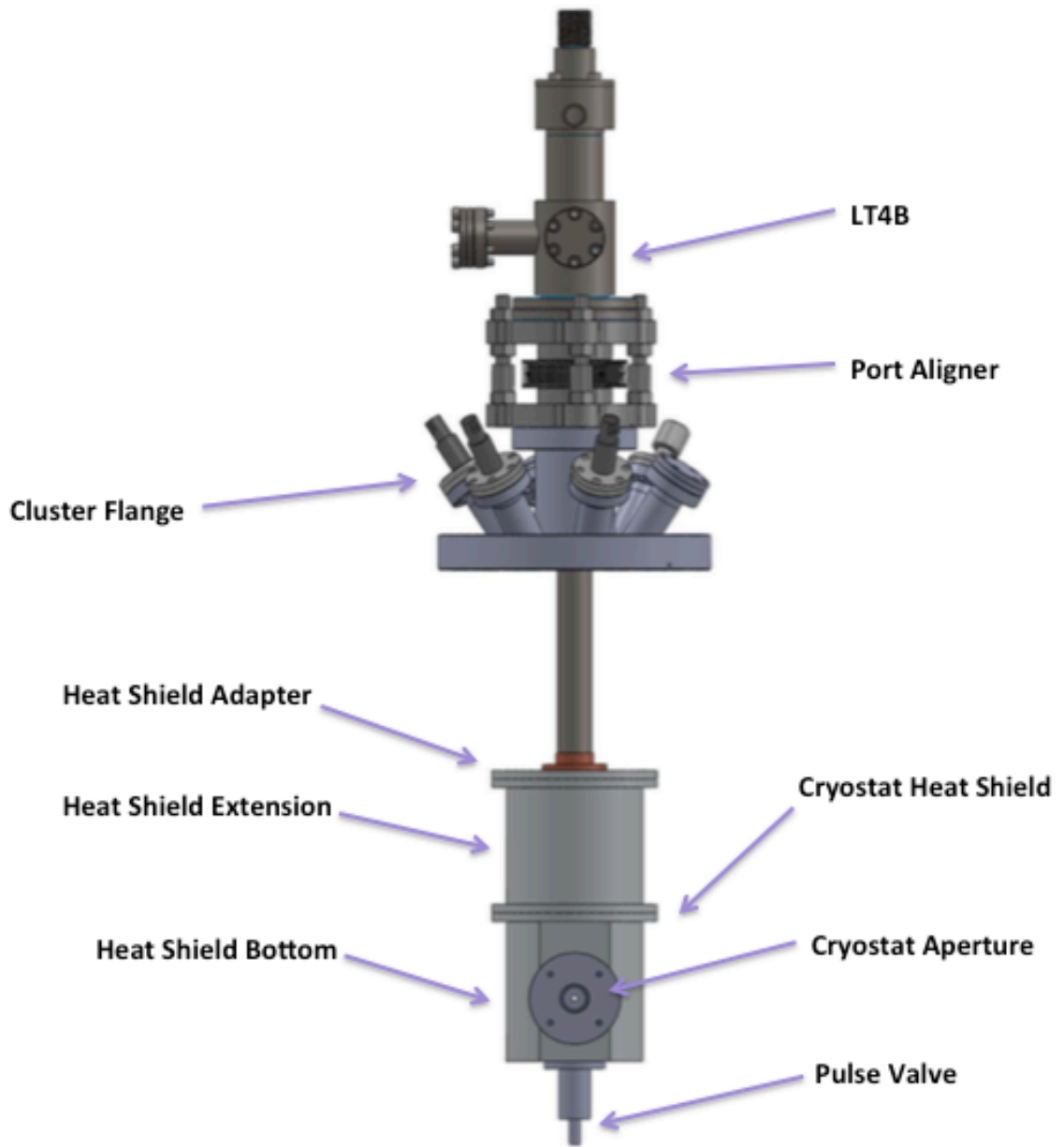


Figure 2.14: This schematic illustrates the existing pulse valve mount on the bottom of the heat shield assembly.

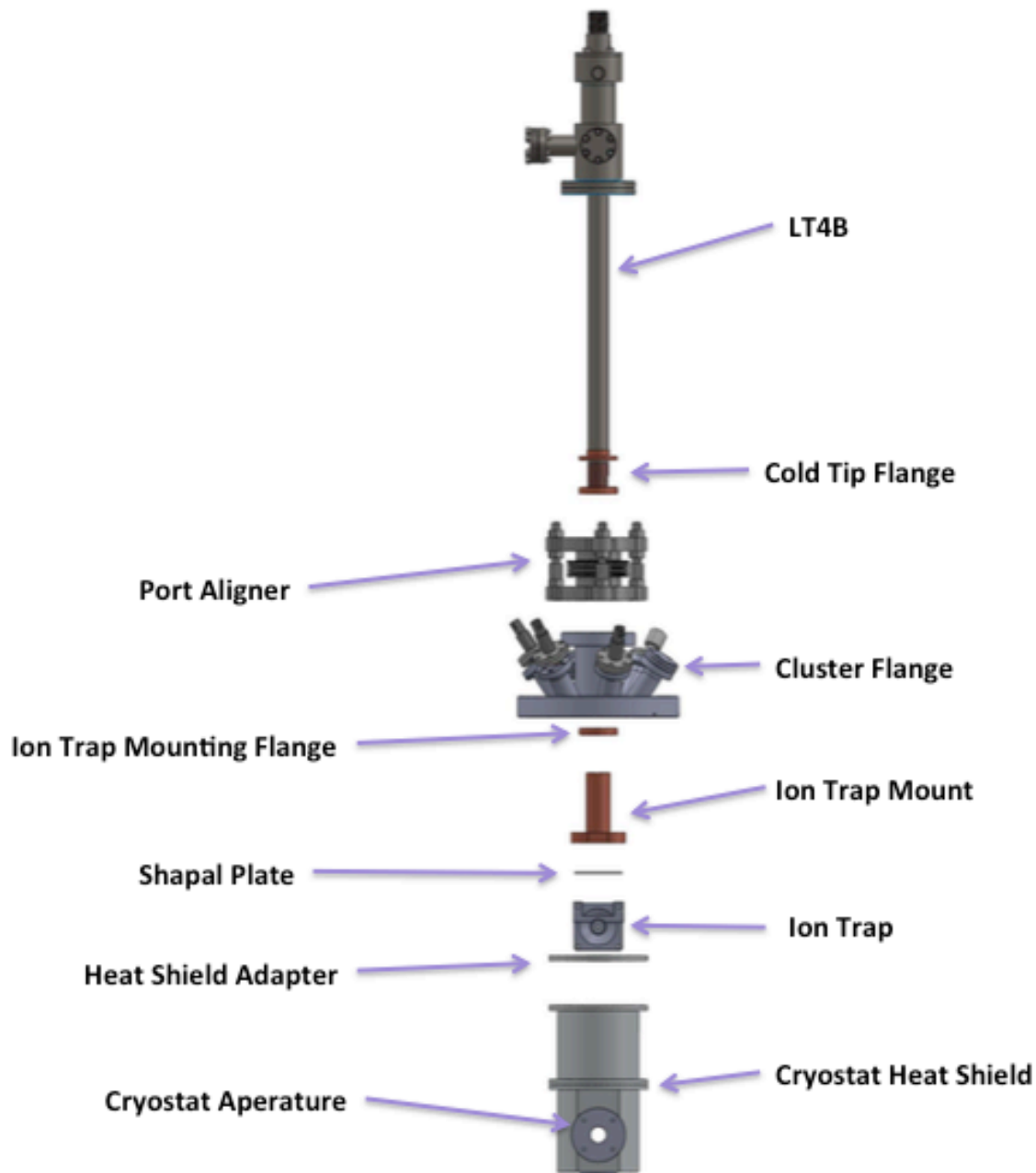


Figure 2.15: This schematic is an exploded view of all the components of the cryostat, including all necessary pieces for mounting and the heat shield assembly.

The ion trap is configured in a closed configuration so buffer gas is crucial to trap and cool the ions. A buffer gas line was constructed, complete with a needle valve to control the flow directly into the ion trap, back up valves, and a mechanical

pump, an Agilent Varian HS 602 dual state rotary vane pump, to deliver variable amounts of buffer gas to the trap. While nitrogen, air, and helium have been used as the buffer gas for calibration and testing purposes, an 80/20 He/H<sub>2</sub> mixture is the preferential choice. While there is a place on the heat shield bottom for a pulse valve to mount, the preferential mode of operation is to continuously bleed in buffer gas. The flow rate is externally controlled by a needle valve that is connected to ¼" stainless steel tubing that is connected to the vacuum region through a port on the cluster flange. From there, a stainless steel Swagelok ® fitting connects the ¼" tubing to 1/8" stainless steel tubing that flows the buffer gas through the heat shield into the ion trap. When the ion trap is running, there becomes enough helium present that the existing vacuum system was struggling to maintain the low vacuum desired, especially after an extended period of time. A "back up" turbomolecular pump, a Varian Turbo-V70 969-9356 series, was incorporated to handle the buffer gas. When buffer gas is being added to the trap, there is a valve that simply switches from the backing scroll pump to the backing turbomolecular pump, which was proven to be adequate in maintaining the vacuum during buffer gas addition.

## **2. Purge Chamber**

In order to accommodate air sensitive samples on the ESI source, a purge chamber was constructed such that the sample would spray in an air free environment accomplished by a continuous flow of dry nitrogen gas. A base flange made of Delrin® was fabricated to mount directly to the copper block holder in the desolvation flange. Four support rods made of 0.25" diameter smooth stainless steel tubing were cut into 3.2" lengths and tapped on both sides to accommodate 6-32

size set screws or flat point screws. The support rods connect on the other side to a Delrin® mounting flange, which has counter sunk holes to accommodate the flat point screws such they are completely flush with the mounting flange surface. The base flange, support rods, and mounting flange assembly hold in place a 2" outer diameter polycarbonate tube, which also has a length of 3.2". There are o-ring grooves cut into both the base flange and the mounting flange to ensure the assembly seals. Next, there is a threaded adapter flange that was 3D printed. The threaded adapter flange mounts onto the mounting flange with 4-40 set screws, oversized washers, and nuts so positional adjustments can be made in all directions. The threaded piece allows for adjustments of the needle tip closer or further from the copper block to optimize the ion signal.

The fused silica tip is held in place at the end of the threaded adapter flange with a small, Delrin® needle mounting flange. The needle mounting flange also has an associate o-ring to ensure it seals. The fused silica tip is again placed gently into a MicroTight® sleeve and are both placed into a MicroTight® coned nut sized to fit the sleeve. A MicroTight® adapter with a MicroTight® PEEK fitting connects the fused silica tip coned nut to the PEEK tubing, 1/16" outer diameter, 0.030" inner diameter. The PEEK tubing spans the length of the threaded adapter flange and another MicroTight® adapter with a MicroTight® PEEK fitting is used to connect the MicroTight® coned nut positioned on the stainless steel needle with the PEEK tubing. There is an additional o-ring positioned in between the threaded adapter flange and the mounting flange to ensure that the assembly seals. There are two channels on the side of the mounting flange allowing for dry nitrogen gas flow and

monitoring. A ¼" stainless steel tube was threaded to fit into the mounting flange while the other side connected to a Swagelok® fitting and needle valve regulating the dry nitrogen gas flow. Figure 2.16 portrays the purge chamber assembly and figure 2.17 depicts how it fits onto the copper block holder in the desolvation flange.

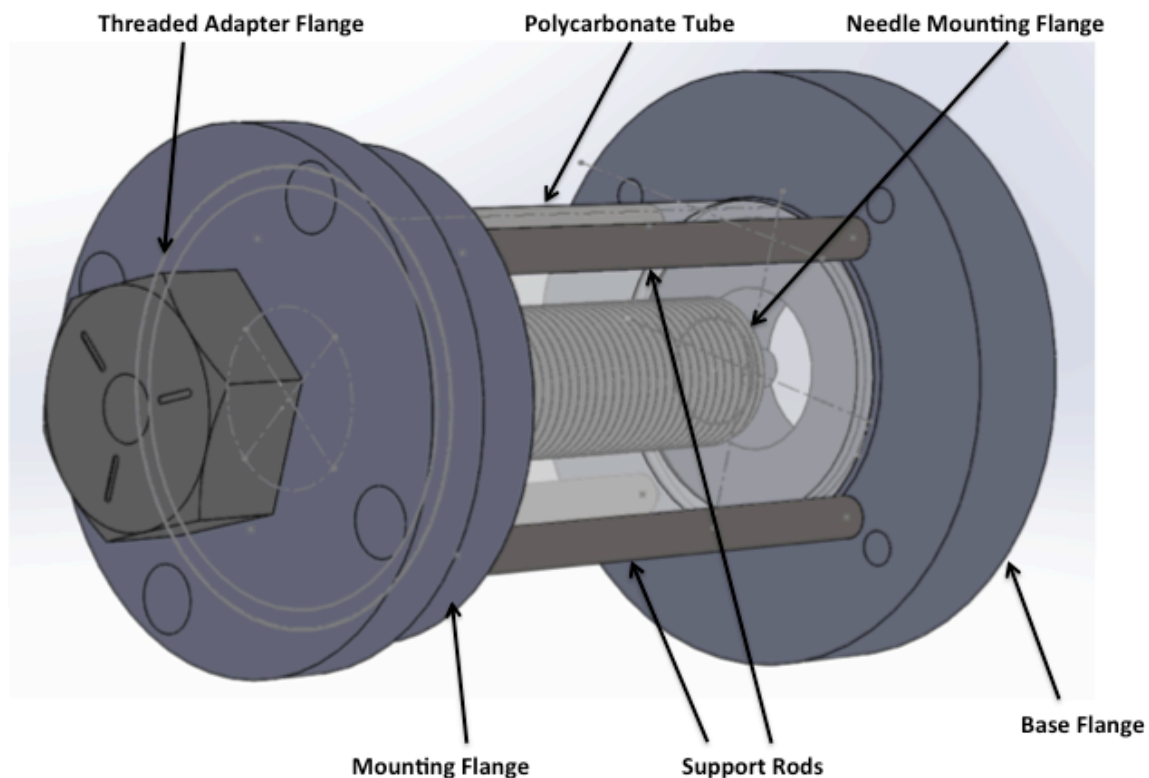


Figure 2.16: This is a schematic of the purge chamber designed and fabricated to accommodate air sensitive samples. Its assembling involves securing the polycarbonate tube in between the four support rods, the needle mounting flange, and the mounting flange. A needle mounting flange, which holds the fused silica tip assembly, is bolted onto the end of the threaded adapter flange. The threaded adapter flange is bolted onto the mounting flange using oversized washers for positional adjustments in all directions. O-rings are used to ensure all surfaces seal.

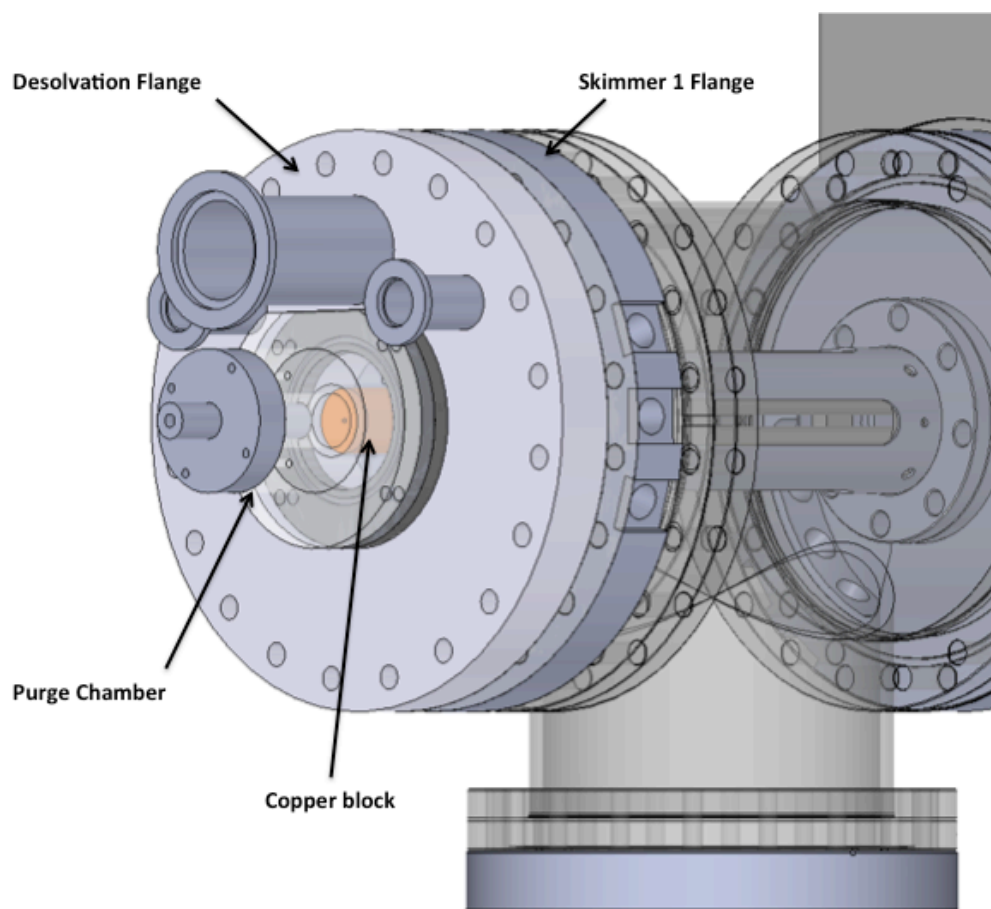


Figure 2.17: This schematic demonstrates how the purge chamber is connected to the external part of the copper block holder.

### III. Modifications to the Vacuum System

Due to the addition of the ESI source, more specifically the requirement of dosing in buffer gas into the ion trap, there needed to be some modifications to the pumping scheme in chamber 1. When working out the pumping scheme, it was crucial to ensure that a stable pressure could be established in that region. If oscillations occur, a stable and reliable ion beam will not be established. There are three ports on the top of chamber 1, as shown in figure 2.18. On both ports A and B, a Pfeiffer Vacuum Turbo HiPace 300 turbomolecular pumps were mounted in a 180°



orientation. There was also a broken reflectron housed in a side chamber attached to chamber 1 that was replaced with a Pfeiffer TMU 261 turbomolecular pump mounted in a 90° orientation.

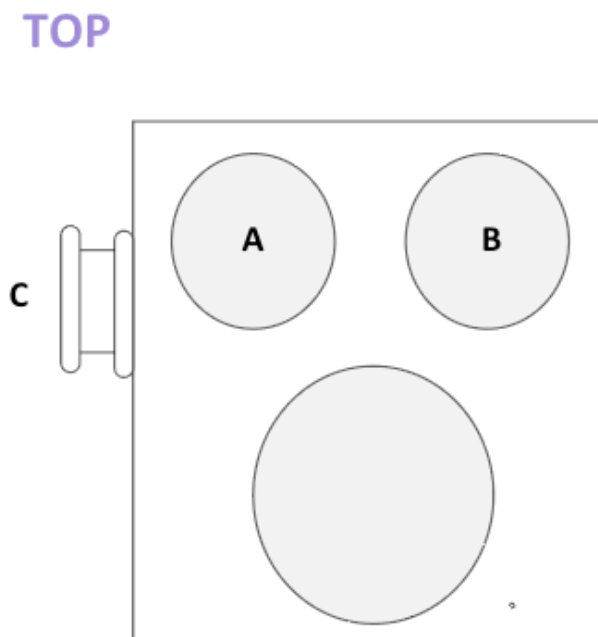


Figure 2.18: This is a schematic of chamber 1. The ports labeled **A**, **B**, and **C** represent where modifications were made to the vacuum system. On ports **A** and **B**, turbomolecular pumps were added in a 180° orientation. On port **C**, another turbomolecular pump was added in a 90° orientation.

Further additions and modifications were made to the flight tube and the interaction region primarily because when taking photoelectron spectra, it is advantageous to have the lowest pressure possible. There is an inline gate valve that separates the flight tube and interaction region from chamber 1, but there are no other assemblies that block off the flight tube from the interaction region. There was a broken ion pump attached to one of the ports near the interaction region. This was

removed and replaced with a working ion pump that was moved from the bottom port of the flight tube. Vacuum modifications were additionally made to the flight tube by adding three turbomolecular pumps, one to replace the ion pump. On both ports D and E a Pfeiffer Vacuum Turbo HiPace 300 was mounted. On port D it is mounted in a 180° orientation while on port E it is mounted in a 90° orientation. On the bottom of the flight tube, port F, a Pfeiffer Vacuum Turbo HiPace 700 was mounted in a straight up orientation. Figures 2.19 and 2.20 show the port locations on the flight tube and in the interaction region.

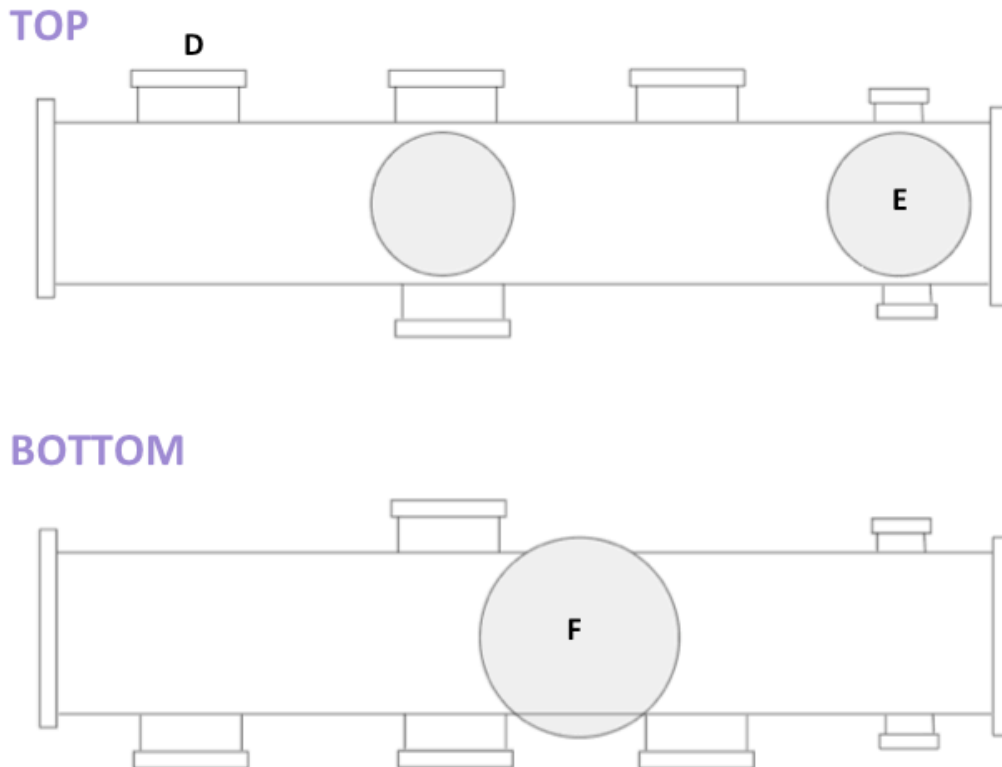


Figure 2.19: This is a schematic of the flight tube in both a top view and a bottom view to show the ports where vacuum modifications were made. On port **D**, a turbomolecular pump was added in a 90° orientation. On port **E**, a turbomolecular

pump was added in a 180° orientation. On port **F**, an ion pump was moved and replaced with a larger turbomolecular pump.

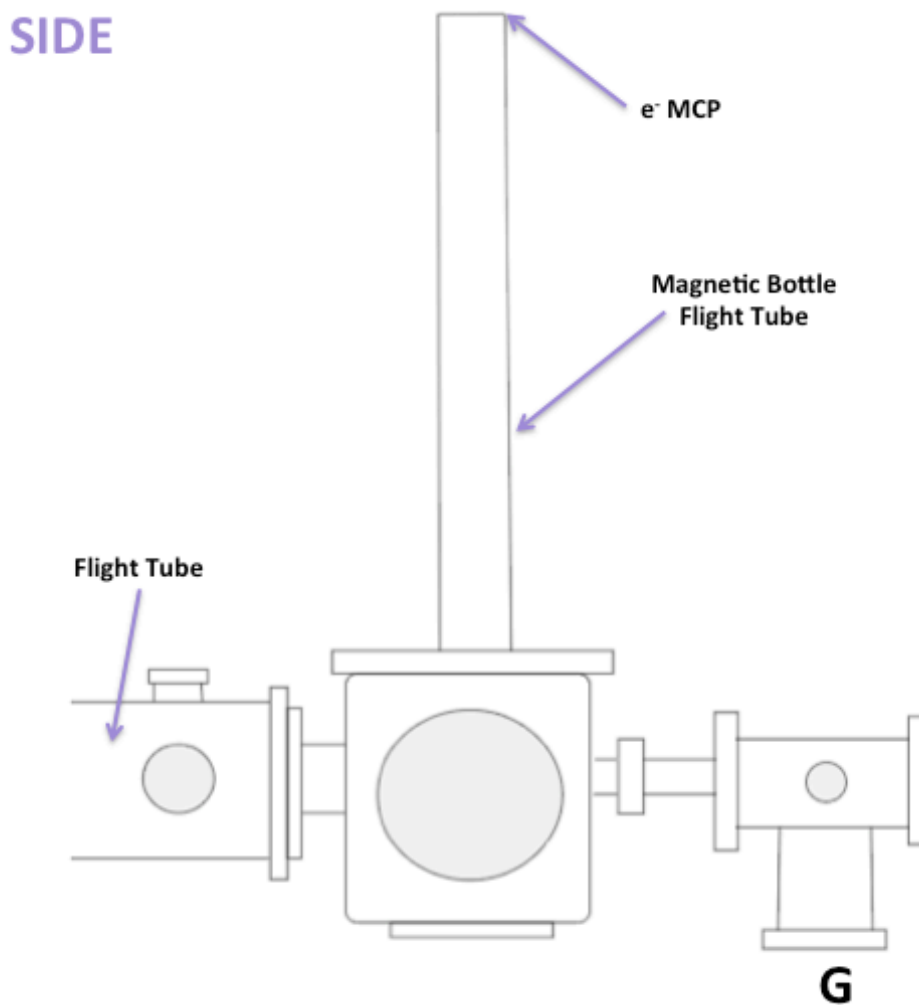
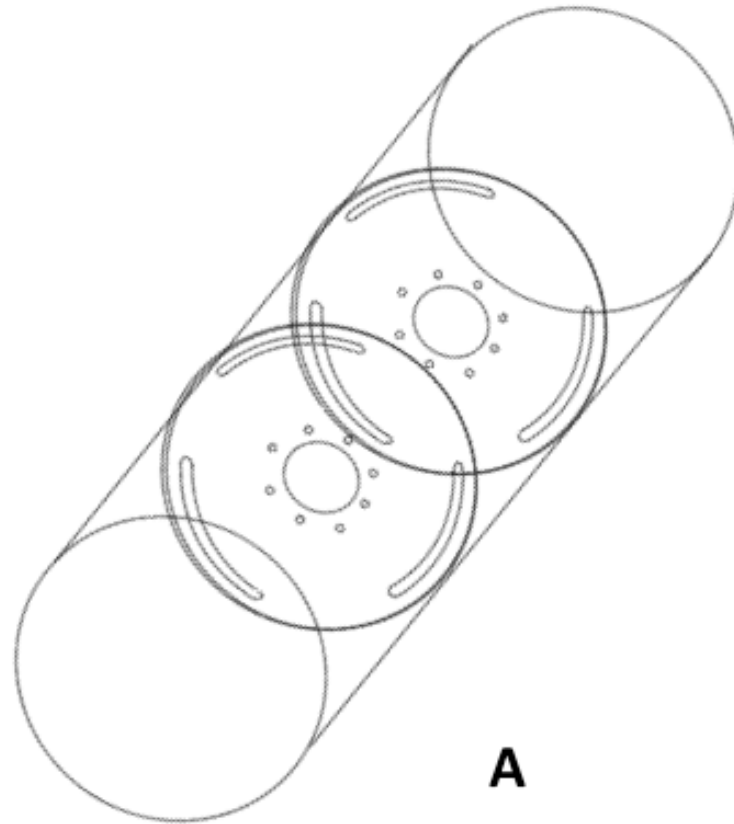


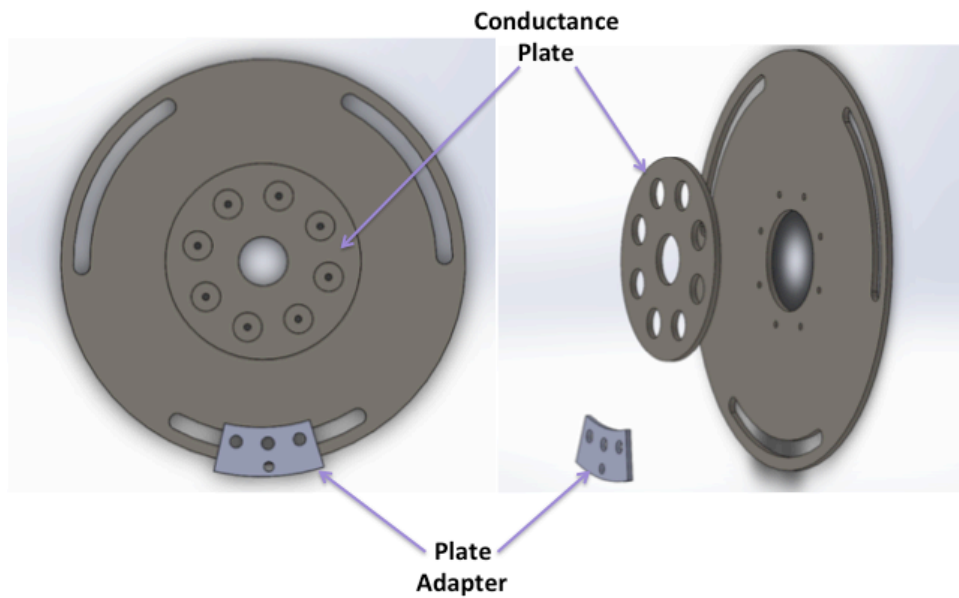
Figure 2.20: This is a schematic of the interaction region in a side view to show the port where vacuum modifications were made. On port **G**, a broken ion pump was removed and replaced with the working ion pump that used to be on port **F** of the flight tube. Note, there is also a cryopump in this region, but it is not shown here so that port **G** is visible.

Prior to the renovations and modifications, there was a conductance limiting aperture located just after the inline gate valve at the beginning of the flight tube.

This differential pumping tube had an inner diameter of 0.6". This was removed and instead two vacuum walls were mounted inside the flight tube. There were already welded tabs inside the flight tube, so plate adapters were designed to hold the vacuum walls upright in place along threaded rods. The conductance plate was designed with two purposes: to limit the size of the center hole and to allow for alignment of the ion beam line. The center hole was decided to be 1" in diameter. The conductance plate is attached to the wall such that it can be moved in all directions to ensure it is centered on the ion beam line. The vacuum walls are 8.25", just under the inner diameter of the flight tube. Very thin stainless steel shim with a thickness of 0.001" was spotwelded to cover the small space between the vacuum walls and the flight tube. The vacuum walls are positioned in the flight tube such that it is essentially split into thirds. Each third includes a port with a turbomolecular pump attached. The figure below shows the vacuum wall assembly.



**A**



**B**

Figure 2.21: This is a schematic of the vacuum wall assembly added to the flight tube. **A)** This is a schematic of the flight tube such that the vacuum walls added are

shown. **B)** This shows the all of the pieces of the vacuum wall together, including both the conductance plate and plate adapter.

#### **IV. Time-of-Flight Mass Spectrometer**

Once the ions from a source are in the extraction region, they are accelerated towards an ion MCP by high voltage pulses. There are five extraction plates in the vicinity of the extraction region with grids spotwelded over the extraction holes. Plate 1 is held at ground; the extraction region is defined by plate 2 and plate 3; an adjacent “field free” region is defined by plate 3 and plate 4; the acceleration is defined by plate 4 and plate 5. Such pulses are generated by Behlke HTS-31 variable switches and are applied simultaneously to the plate 2 (-1500 V) and plates 3 and 4 (-1390 V). By pulsing these plates, two high field regions are generated and are separated by a field free region. The switches are triggered by TTL pulses generated by a Stanford Research Systems 535 delay generator.

In the setup before all the renovations, the ions first encountered a box deflector set after being accelerated in the extraction region followed by two Einzel lens assemblies. The purpose of the deflectors is to compensate for the initial kinetic energy of the ions perpendicular to the axis of extraction. The Einzel lens assemblies are intended to focus the ion packets onto the ion MCP detector. Two Einzel lenses are used here because they focus without changing the energy of the ion beam.

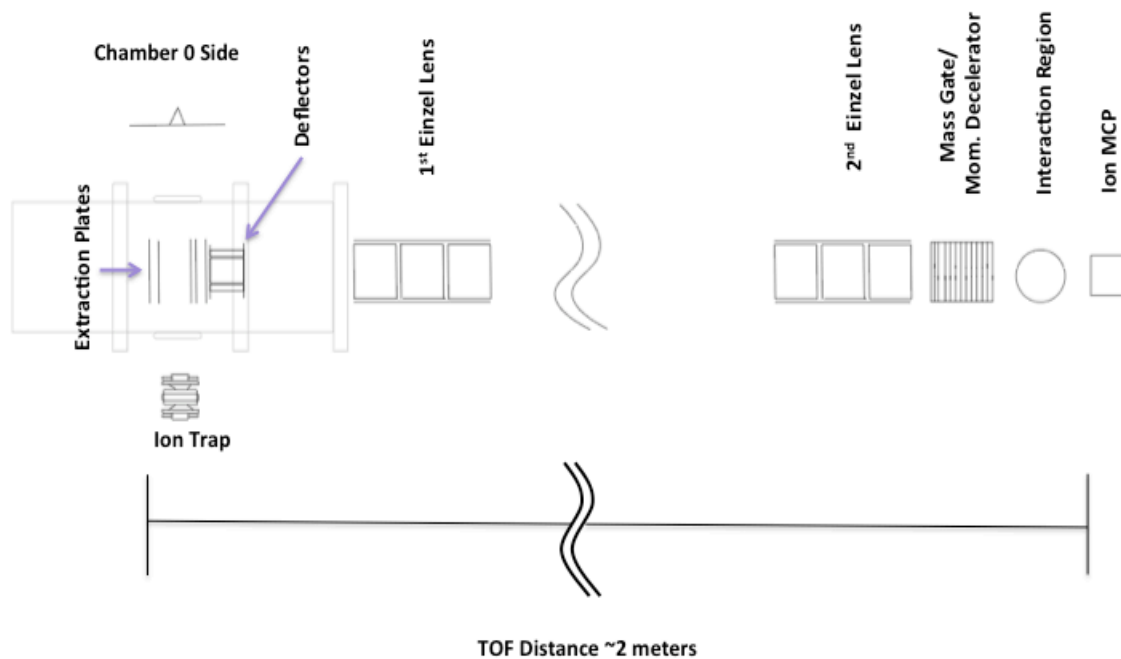


Figure 2.22: This is a schematic of the TOF mass spectrometer region. Here, the ion trap is used to indicate the ESI source side. As depicted, the extraction plates and deflectors are located inside the internal box (chamber 2).

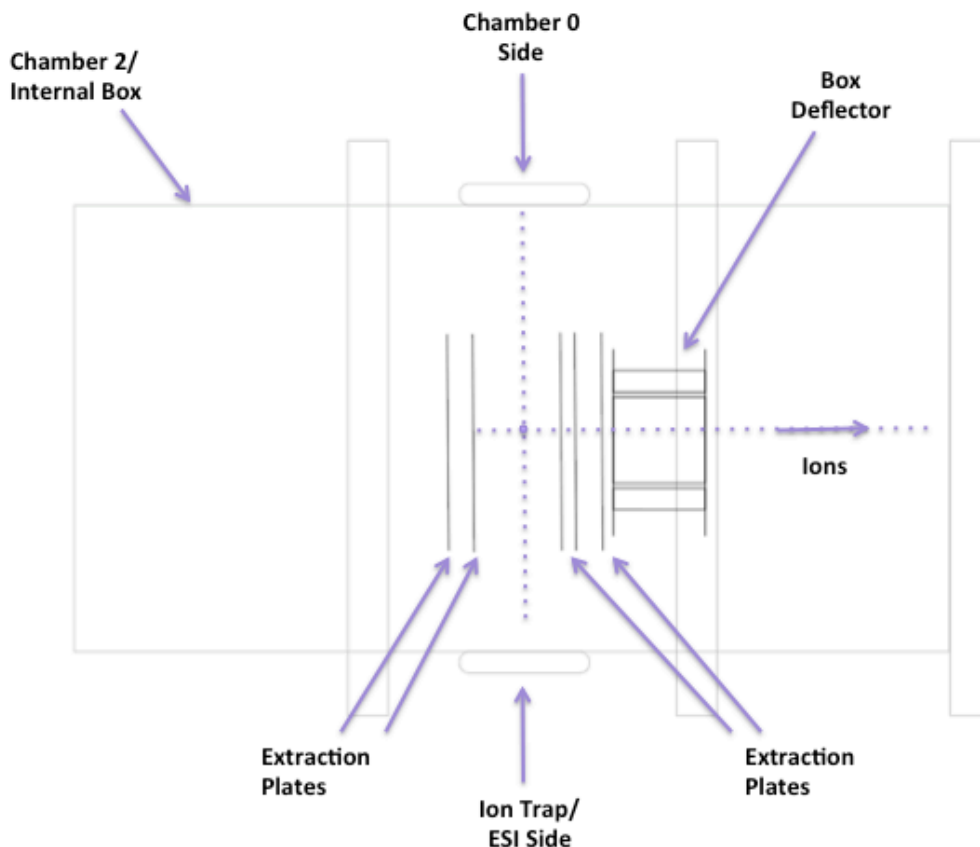


Figure 2.23: This schematic depicts the previous setup of the internal box (chamber 2), which includes the extraction plates and a box deflector.

### A. Deflectors

As previously noted, the deflector set in the apparatus prior to renovations was a box deflector set. In the box deflector, there are grounded entrance and exit plates with completely open center holes 1" in diameter. The deflection plates have a gap of 1.5" between them, which is where the ion beam travels through. The new design includes separated horizontal and vertical deflectors. There are now grounded plates at the front, in between, and at the end. The deflection plates have been both widened and lengthened to provide uniform electric fields. The horizontal deflector, which deflects the ions to either the left or the right, is mounted first just



after the extraction stack followed by the vertical deflector, which deflects the ions either up or down. Figure 2.24 depicts the new contents of the internal box (chamber 2). Figure 2.25 details how voltages are applied in the new setup.

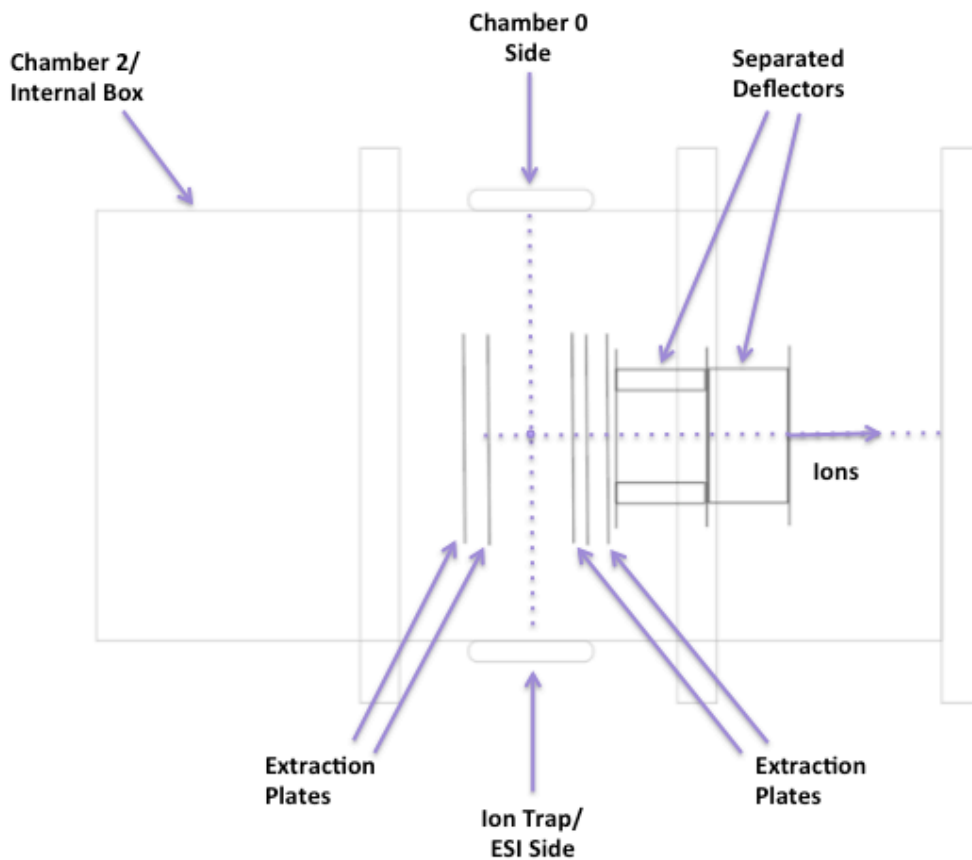


Figure 2.24: This is a schematic of the new setup of the internal box (chamber 2). Now, the deflectors are separated with the horizontal deflector mounted first, followed by the vertical deflector. There are three grounded plates in this setup, one in the front, one in between, and one at the back.

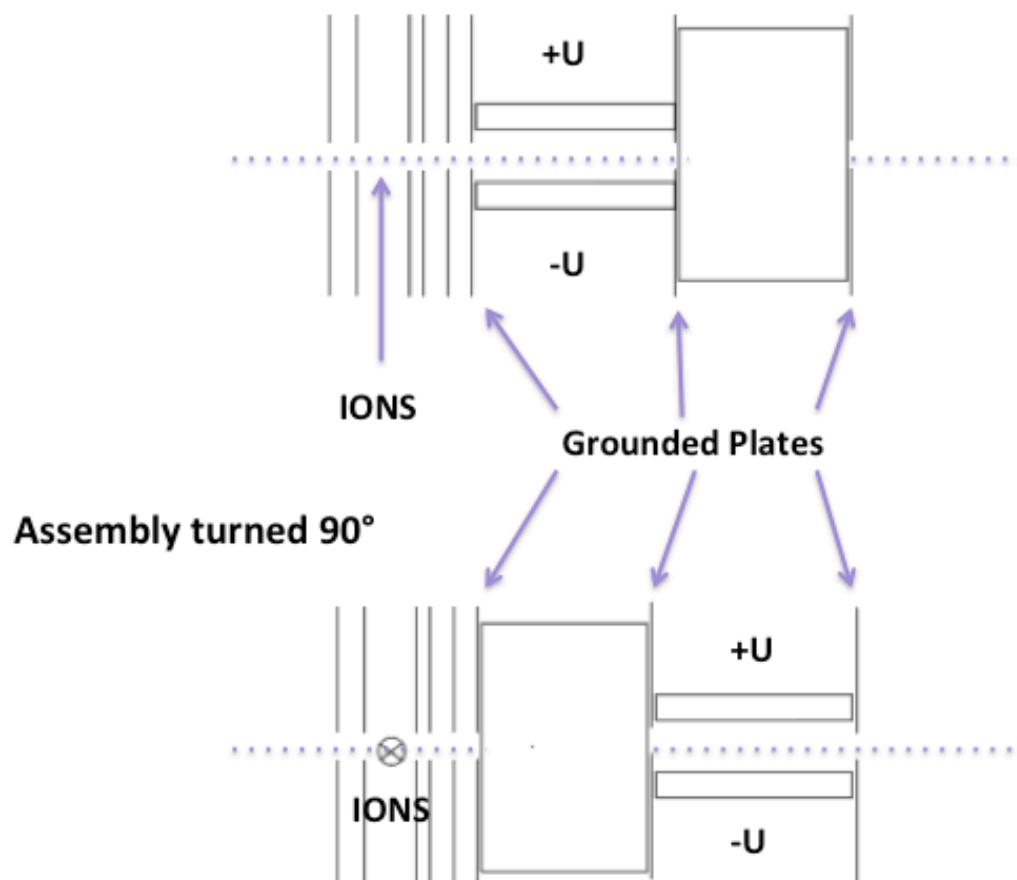
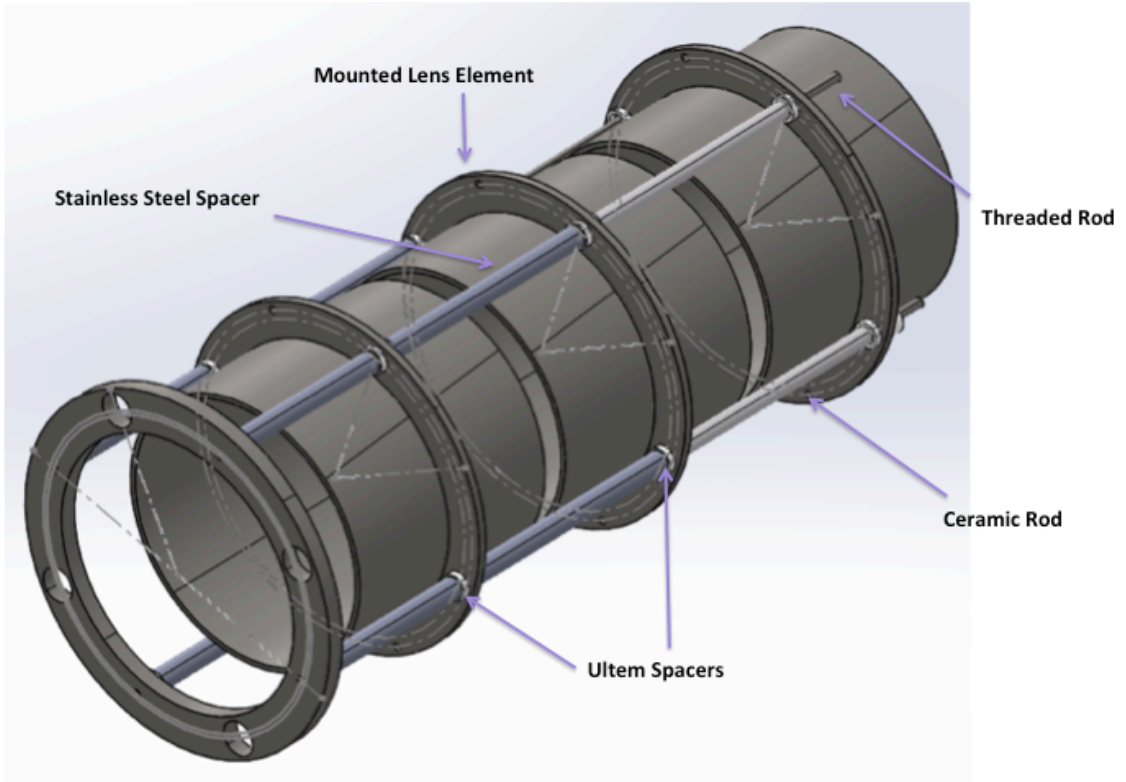


Figure 2.25: This is a schematic of the modified deflectors. Now, the horizontal and vertical deflection units are separate. The ions encounter the horizontal deflector first then the vertical deflector. There are grounded plates in front, in between, and at the end of the deflections units. The +U/-U is such that there is 0 V on the middle axis. The deflection electrode plates are wider than before, so the ions encounter a uniform deflection field.

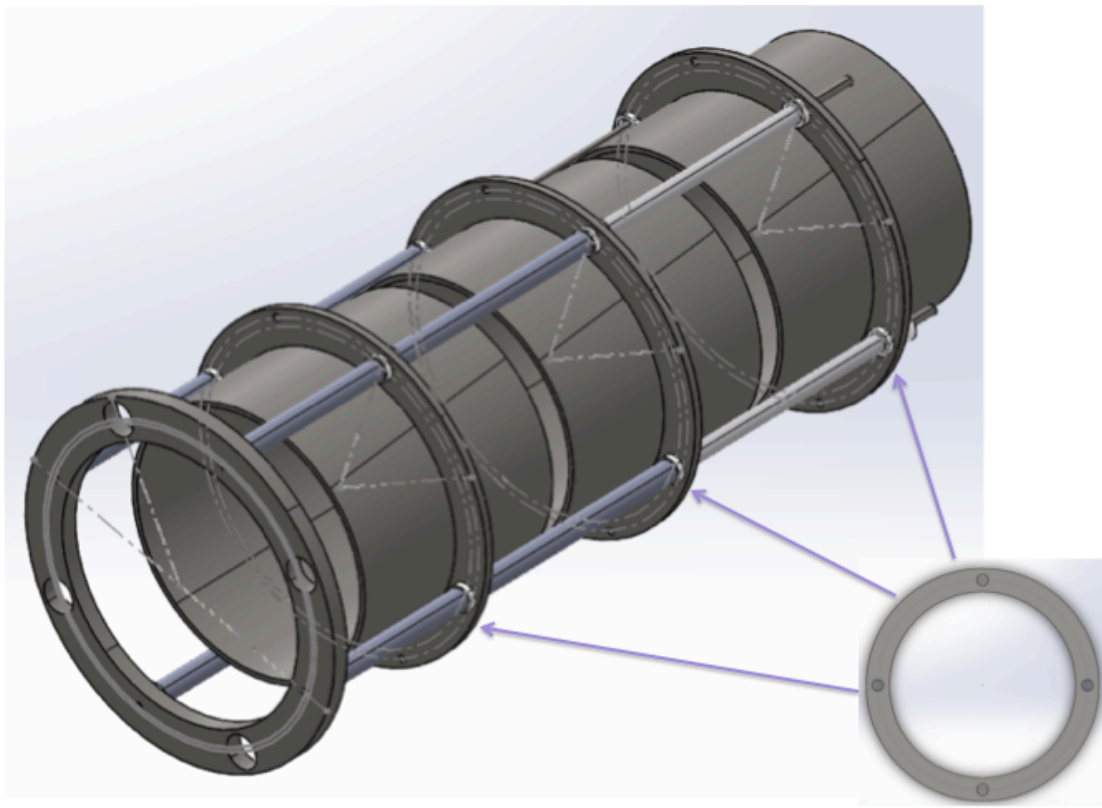
### B. First Einzel Lens

While the previous first Einzel lens was operational, it was not able to adequately handle the ion beam created from the ESI source side resulting in massive losses in ion signal intensity. The previous first Einzel lens had an inner diameter of 1.76". Comparing this to those who have similar ESI sources setups,<sup>6,7</sup> it

was at least half as small. Using SIMION®, Scientific Instrument Services, Inc. (Ringoes, NJ), simulations were performed and the first Einzel lens was modified to have a 3.83" inner diameter, 4.0" outer diameter allowing for majority of the ESI source side ion beam to be accommodated and focused. The length of the cylindrical tube elements is 3.6". 304 stainless steel was used to construct the redesigned first Einzel lens including the lens elements, the chamber mounting flange, and individual lens mounts. The mounted lens elements were assembled via high temperature silver braze. Threaded rods were used for the base supports and ceramic tubes were fitted over the threaded rods. Stainless steel spacers were fabricated and placed in between each lens element with Ultem (polyetherimide) spacers on either side. Finally, 0.004" diameter stainless steel shim was spot welded to each of the stainless steel spacers and connected to a ground in the chamber.



**A**



**B**

Lens Mount

Figure 2.26: This is a schematic of the first Einzel lens. **A)** The stainless steel spacers in between the second and third elements were made transparent to show the ceramic rods underneath. **B)** The lens tubes were mounted in the lens mounts via high temperature silver braze.

### **C. Second Einzel Lens**

The second Einzel lens is located just before the mass gate and momentum decelerator assembly. The previous lens was especially problematic, essentially charging up after a period of time, diminishing the ion signal, and eventually annihilating it all together. The previous lens had aluminum parts, which was likely a source of charge up, and was poorly aligned. While it was possible to collect adequate data from the chamber zero side, it was not possible from the ESI source side. Thus, the second Einzel lens was removed and replaced with one made from Kimball Physics, Inc. (Wilton, NH) parts, which are intended for use in high vacuum applications. The newly constructed lens is made from stainless steel and ceramic parts. The lens cylinder elements have an inner diameter of 1.4", an outer diameter of 1.5", and a length of 3.6". The cylinders are precision cut lengths of seamless metal tubing. The individual lens elements were constructed by positioning the cylinders in the plates. The plates have small holes punched in them on the outside borders and are designed such that they can be mounted onto the ceramic rods. Wire rings are utilized to keep the cylinders in place once assembled. The wire rings are first spotwelded to the plate four times and then to the cylinder another four times. The technique used to assemble the lens was to thread the plates supporting the cylinders together by passing the ceramic rods through the punched holes and

using the ceramic and stainless steel spacers to hold the plates apart. The primary purpose of the stainless steel spacers is to protect the ceramic from contamination and avoid charge-up by stray particles. Stainless steel shim with a thickness of 0.004" was spot welded to the stainless steel spacers and connected to a ground in the chamber. On one end, the side to be mounted off the mass gate/momentum decelerator assembly, screw clamp assemblies are used to hold the assembly in place on the ceramic rods; these were chosen since they are ideal for heavier assemblies. On the other side, stainless steel lock rings are used and were spotwelded into place. The figure below shows the second Einzel lens stack.

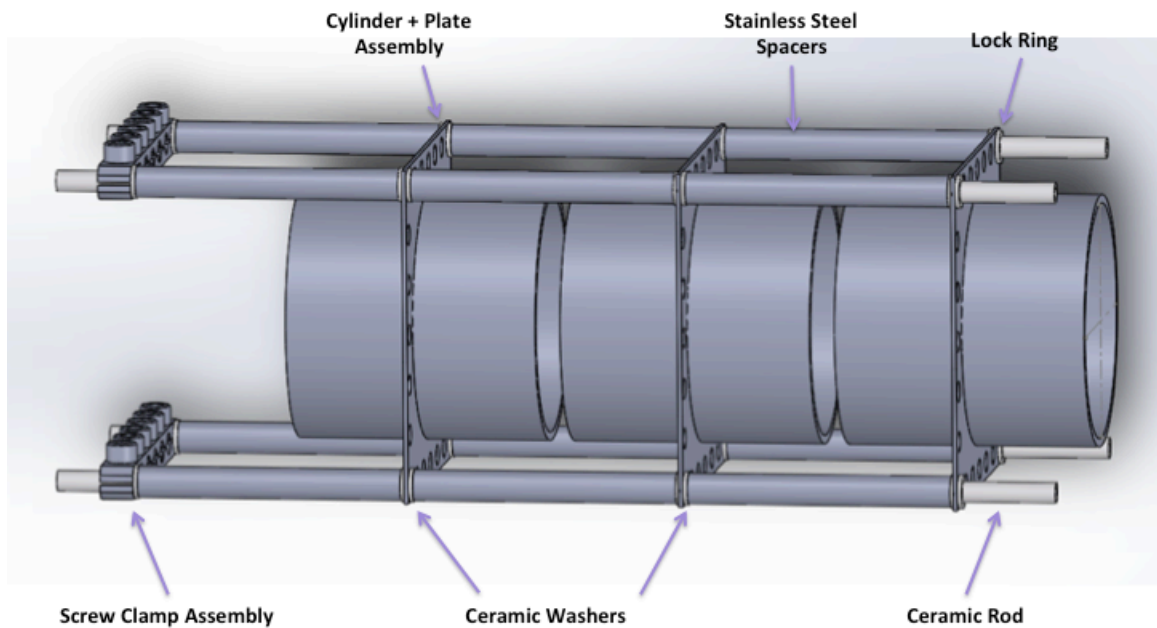


Figure 2.27: This is a schematic of the second Einzel lens stack.

The Einzel lens stack was then attached to the mass gate/momentum decelerator assembly using lock rings, short lengths of stainless steel rod, and the screw clamp assemblies ensuring the entire load is supported. Once the second

Einzel lens stack was mounted to the mass gate/momentum decelerator assembly, the whole thing was mounted to the decelerator mount plate. An additional rectangular plate, which spanned the entire seven holes of the enclosure plate, was mounted to the back of the mass gate/momentum decelerator assembly using stainless steel rods and lock rings and the top set of holes of the rectangular plate. The entire assembly is mounted to a decelerator mounting plate, which is supported by two “L-mounting” brackets that are mounted to the bottom of the chamber, also using stainless steel rods and lock rings and the bottom set of holes of the rectangular plate. Figure 2.28 illustrates the entire assembly.

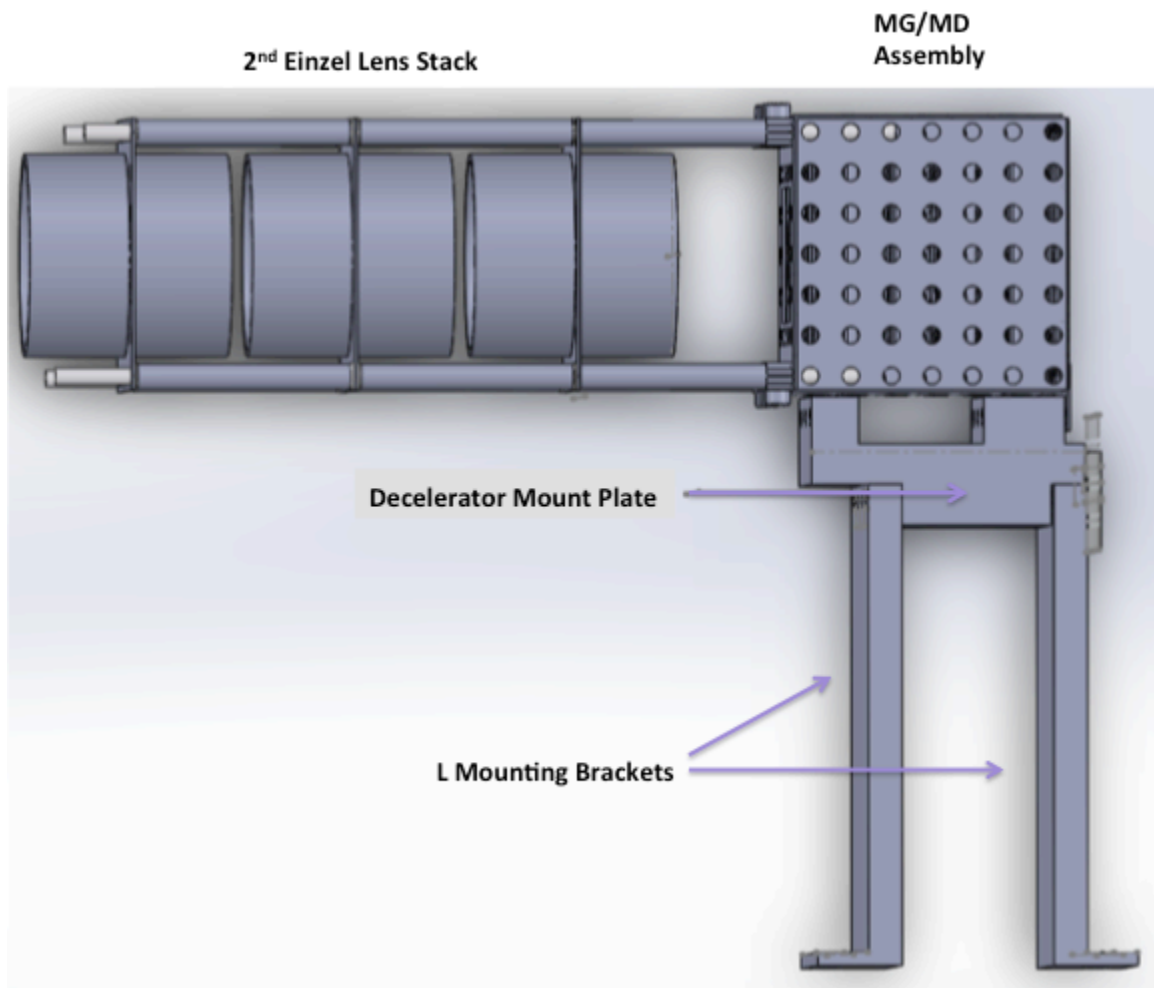


Figure 2.28: This is a schematic illustrating how the second Einzel lens stack is mounted off the mass gate/momentum decelerator assembly and how it is supported in the chamber.

The figures below illustrate all the modifications that were performed on the TOF mass spectrometer region, including the separated deflectors, the larger first Einzel lens, and the second Einzel lens constructed from Kimball Physics parts, mounted to the mass gate/momentum decelerator assembly.

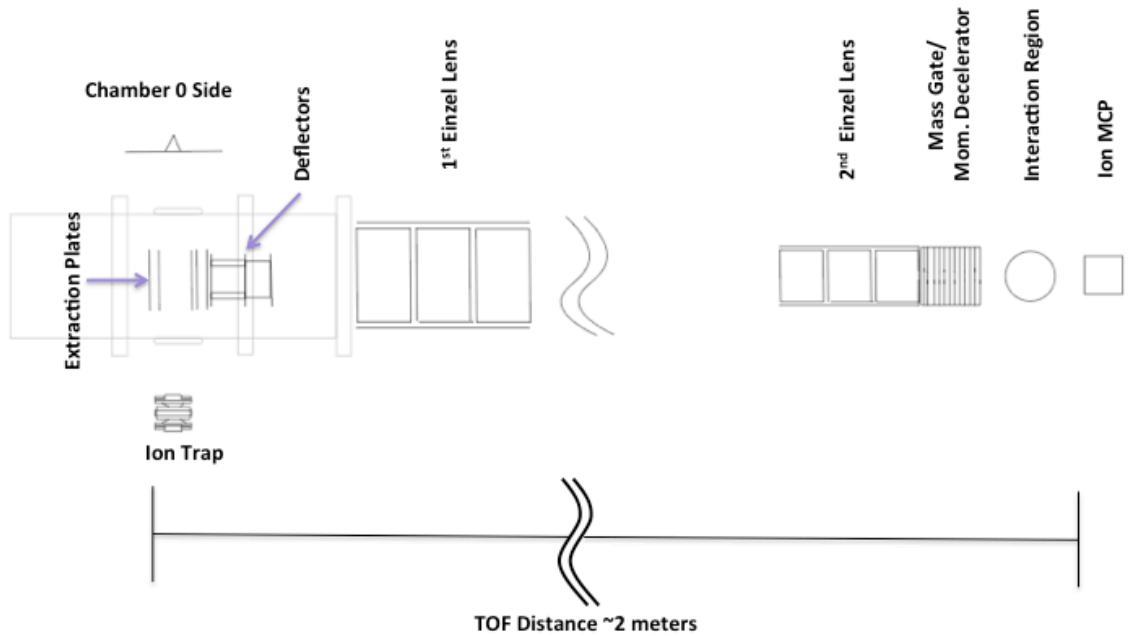


Figure 2.29: This schematic reflects the new design modifications that have been executed in the TOF mass spectrometer region.



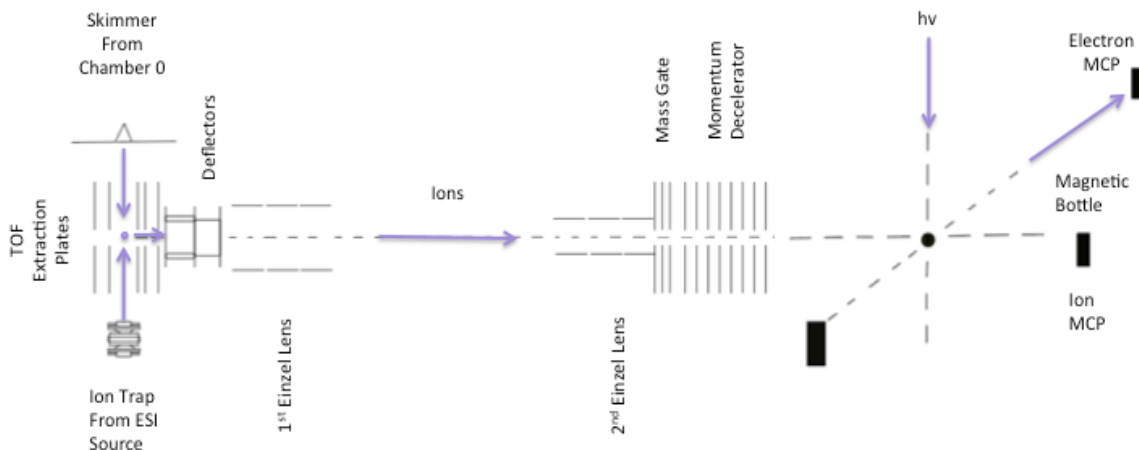


Figure 2.30: This schematic depicts the general setup with the new design modifications implemented.

The following table gives the pressures of the relevant regions on the apparatus. The base pressure reading represents the apparatus under no gas load from experiments. It is important to note that the base pressure readings are given under the conditions that there are no leaks and all pumps are on and working. The chamber 0 side pressures are reported for a laser vaporization experiment using helium as the backing gas, at a backing pressure of 50 psi. The ESI side pressures are reported for a continuous flow of helium as the buffer gas. It should be noted that these values could change upon switching buffer gases. These values will also change if there is a leak or if a pump is not working properly.

	Base Pressure (Torr)	Chamber 0 Side(Torr)	ESI Side(Torr)
Chamber 1	1.70E-06	4.40E-06	8.50E-06
1st Flight Tube Partition	1.10E-07	7.80E-07	2.00E-06
2nd Flight Tube Partion	5.20E-08	7.20E-08	1.20E-07
Interaction region	3.10E-08	4.20E-08	8.20E-08

Table 2.1: Table of base pressures and working pressures of both the ESI source side with buffer gas added and the laser vaporization source with helium in chamber 0.

## **V. Interaction Region**

In general, after leaving the second Einzel lens, the ions encounter the mass gate and momentum decelerator assembly then move on to the interaction region. The interaction region is defined as the point of intersection between the mass selected ion beam and photodetachment laser. Centered above the interaction region is the weak field portion of the magnetic bottle, a solenoid covered flight tube. Located below the interaction region is a rare Earth magnet that defines the strong field portion of the magnetic bottle. The photodetachment laser is either a Nd:YAG photodetachment laser (primarily operated in the third harmonic, 355 nm, or fourth harmonic, 266 nm) or an excimer (operating at 196 nm). The beam of either of these lasers enters and exists through CaF windows, after proceeding through a series of aligned external apertures.

There is also a shroud or shield around the interaction region to reduce any stray electric fields resulting from the mass gate, momentum decelerator, or the ion detector. The shroud is a 304L stainless steel cylinder with a 2" inner diameter. There are four holes in the shroud, two for the ion beam and two for the laser beam. The ion beam inlet is 0.32" and the outlet is 0.40". The laser beam inlet and outlet are 0.52". The magnet, which is mounted such that its height is adjustable, is essentially centered in the shroud. The magnet is raised and used as an anchor point during alignment.

There is both an input and output light baffle through which the photodetachment laser is directed. On the input side, the baffle incorporates into

vacuum by being flange mounted directly onto the main chamber. A portion of the baffle is exposed to atmosphere while the rest is under vacuum. To align the input baffle, a bellows and cylindrical extension flange is included along with a third flange fixed in space to hold all the adjustment screws in place once aligned. The apertures and spacers are held in place by the outer cylindrical tube that the flanges and bellows pieces are welded to. The laser entrance window is bolted directly onto the input light baffle assembly. On the output side, the entire baffle is in vacuum and held up by two identical ring mounts. The outer cylindrical tube, which is identical in dimension to the input side, holds the apertures and spacers in place and is mounted through the center of the ring mounts. This ring mounts have two sets of alignment bolts, one that holds the ring upright inside the chamber and one to hold the light baffle in its aligned position. The figures below illustrate the general locations and features of these assemblies.

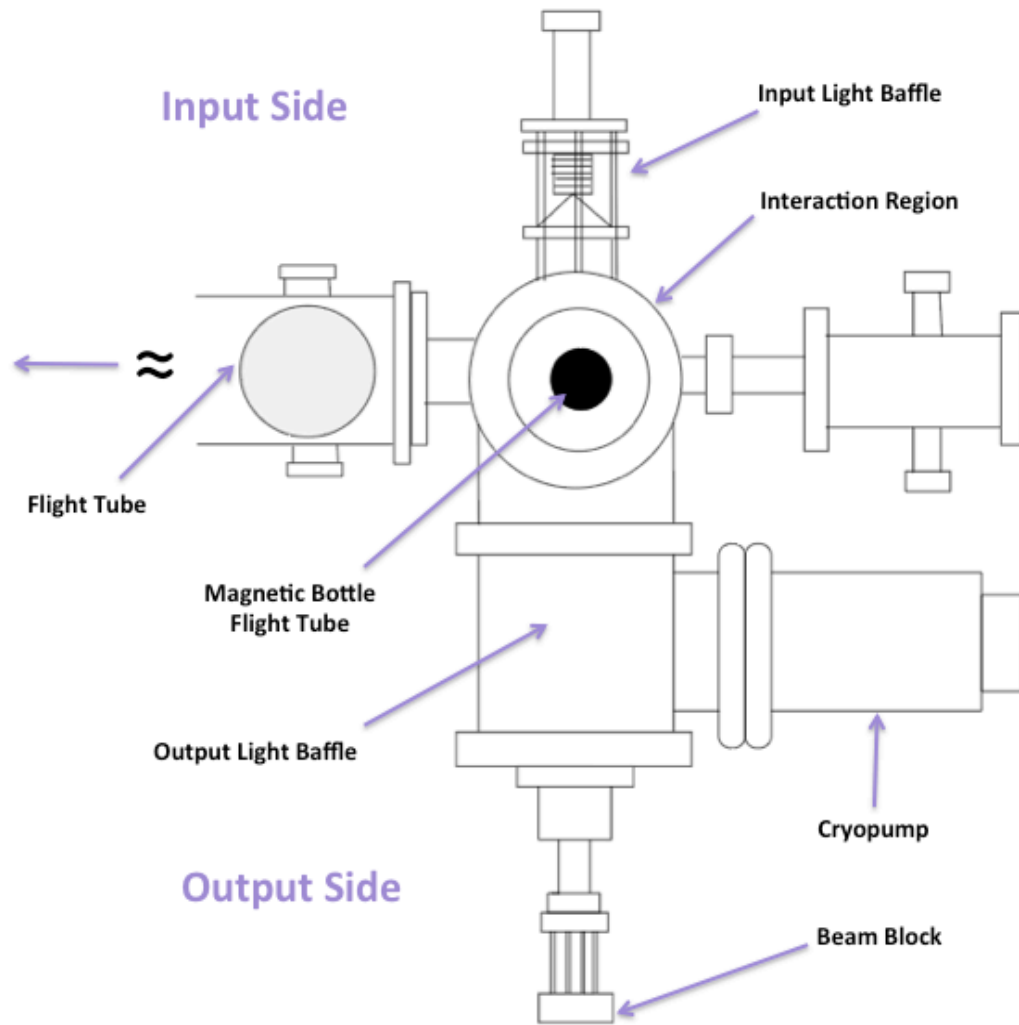


Figure 2.31: This schematic show the interaction region of the apparatus from a top view. In this schematic the cryopump is shown attached for completeness.

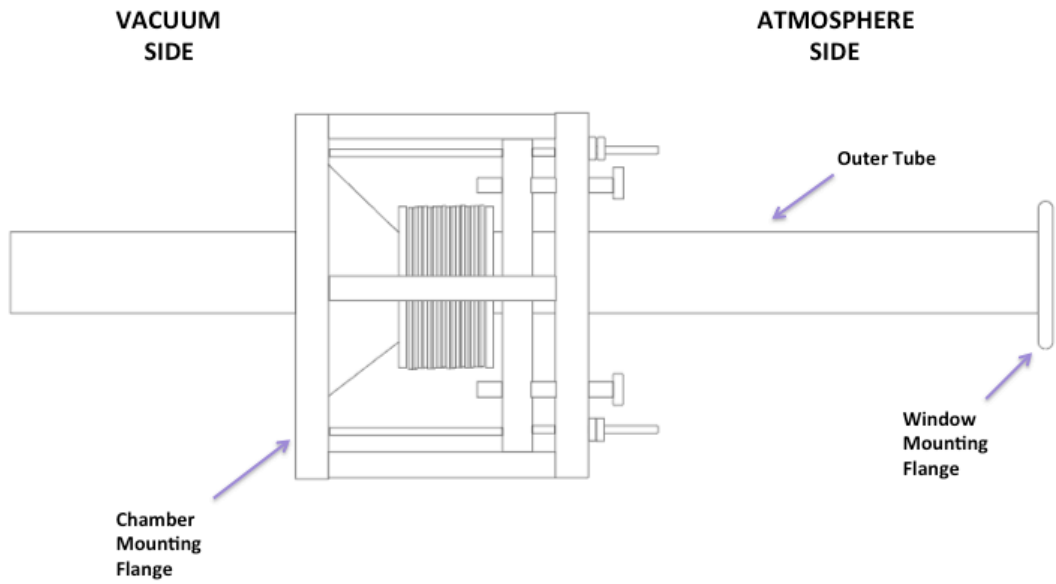
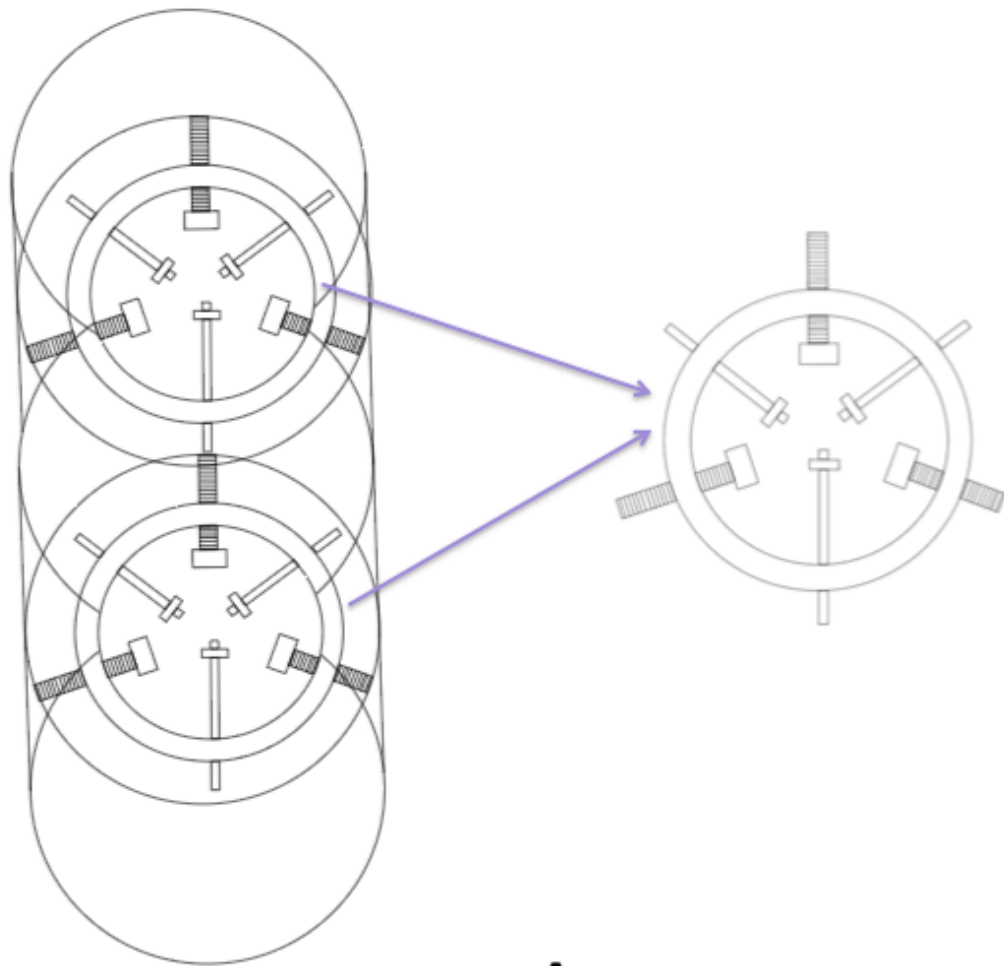
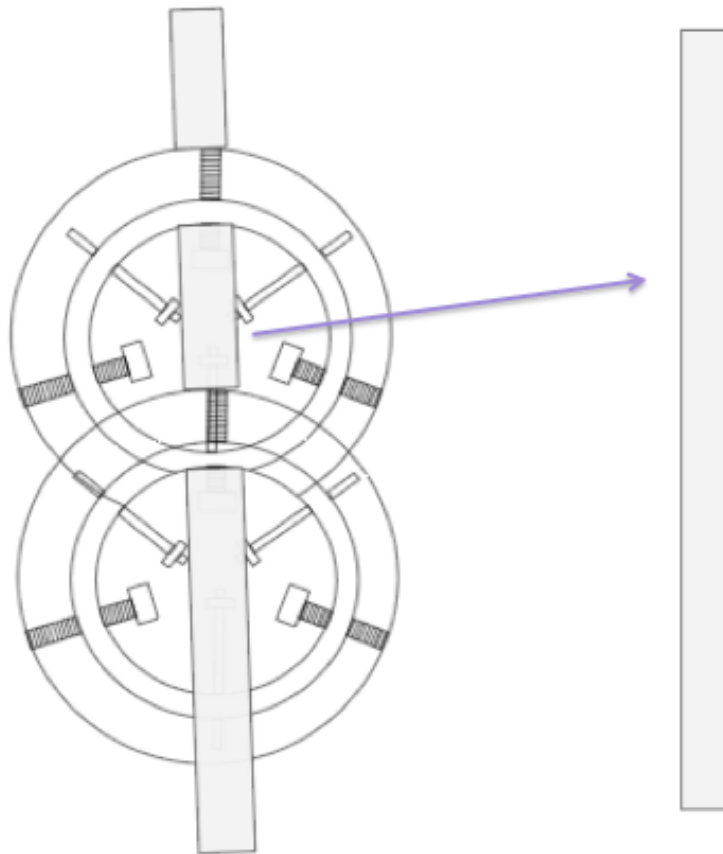


Figure 2.32: This is a schematic of the input light baffle.



**A**



**B**

Figure 2.33: This is the schematic of the output light baffle. **A)** This is a schematic of the ring mounts inside the vacuum chamber. **B)** This is a schematic of the outer cylindrical tube, which holds the internal apertures and spacers in place, mounted in the ring mounts.

### **A. Light Baffles**

The purpose of the light baffle is to block low-order stray light paths and effectively reduce stray photons. The main part of the baffle is a cylindrical tube that was designed to enclose the photodetachment laser path and block zeroth-order stray light paths.<sup>15</sup> Apertures are included internally to block scattering. These stray

light paths are the source of unintended photons.<sup>15</sup> The diameter of the laser beam is 6 mm and should pass through the light baffle essentially unperturbed. When the original light baffles were removed from vacuum, it became immediately clear that this design was actually a telescope rather than a baffle. Modifications were made accordingly to keep the external parts, the outer cylindrical tubes and mounts on each side, while redesigning the internal apertures and spacers.

In the old light baffle setup, instead of a flat laser window at the output, a Brewster angle window was used. It was intended to prevent photons from reflecting off the output window and scattering back towards the interaction region; but it actually did the opposite. It is important to note that the input baffle is symmetric to the output baffle. The length of the outer cylindrical tube is 18". The diameter of the A3 center hole, which is where the laser beam enters on the input side and then exits on the output side, was 6 mm (.236"), and essentially the diameter of the laser. The diameter of the A2 center hole, which is the second aperture on both sides, is 7 mm (.275"). The diameter of the A1 center hole, which is right before the interaction region on the input side and just after the interaction region on the output side, 13.21 mm is (.52"). Since A1 is more than double the size of the laser beam, it is not actually blocking any scattering. Also, A1 is not facing the optimal way. Both A1 and A3 are threaded, while A2 is not and is held in place with spacers. Furthermore, the apertures were not equally spaced within the outer cylindrical tube. Spacer SP1 (2.196") is significantly shorter than SP2 (14.825"). The figure below shows the schematic of the previous light baffles.

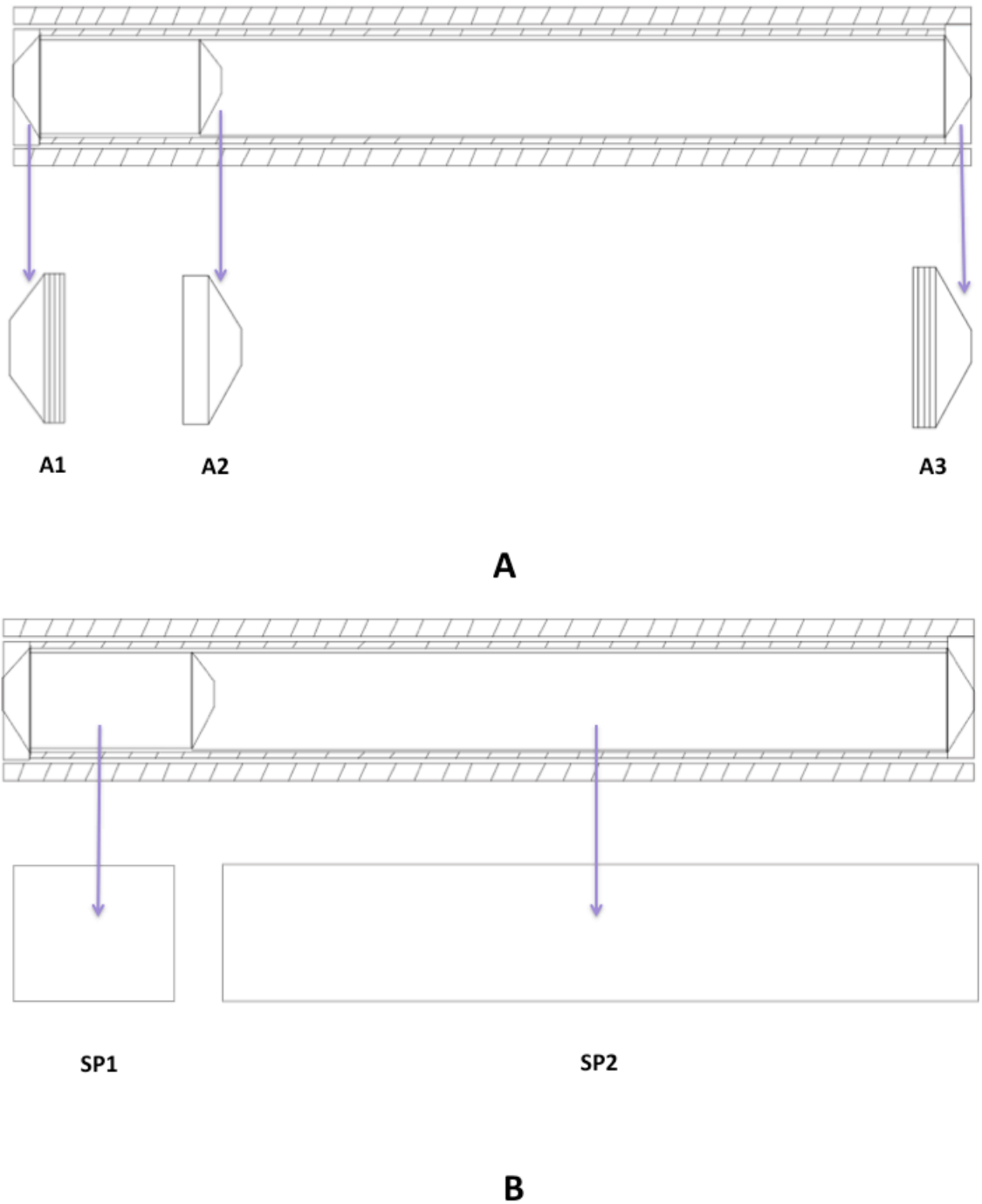


Figure 2.34: Schematic of the old light baffle that used to be in the machine. Note that the output baffle is symmetric to the input baffle. **A)** This shows the orientation of the internal apertures, which vary in the diameter size of the center hole. Apertures A1 and A3 are threaded whereas A2 is not. The diameters of the

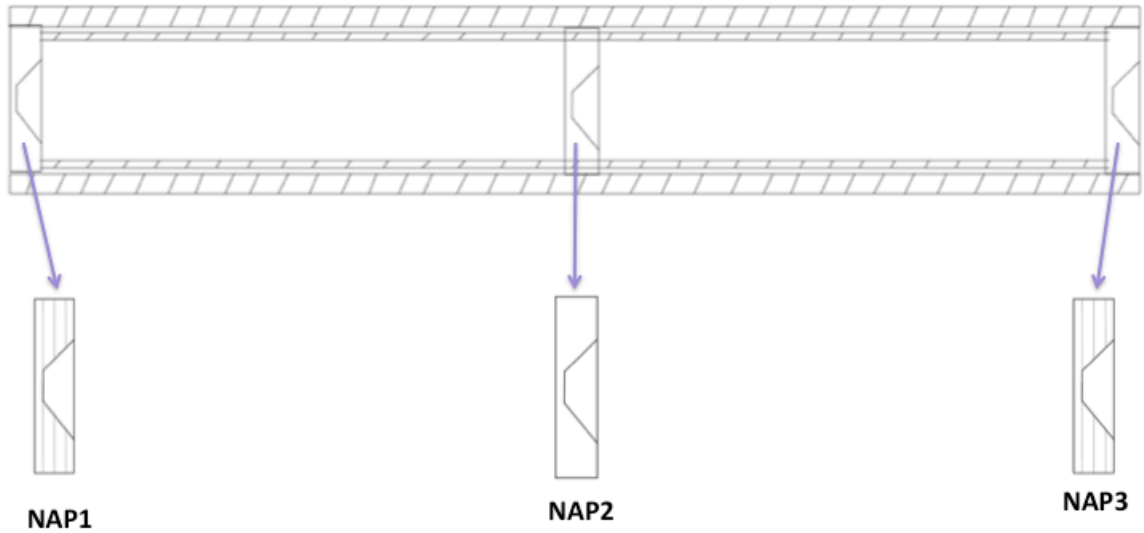


apertures were: A1 (.52"), A2 (.275"), and A3 (.236"). **B)** Here, the spacers are shown, and since aperture A2 is not threaded, the spacers hold it in place. The lengths of the spacers were: SP1 (2.196") and SP2 (14.825").

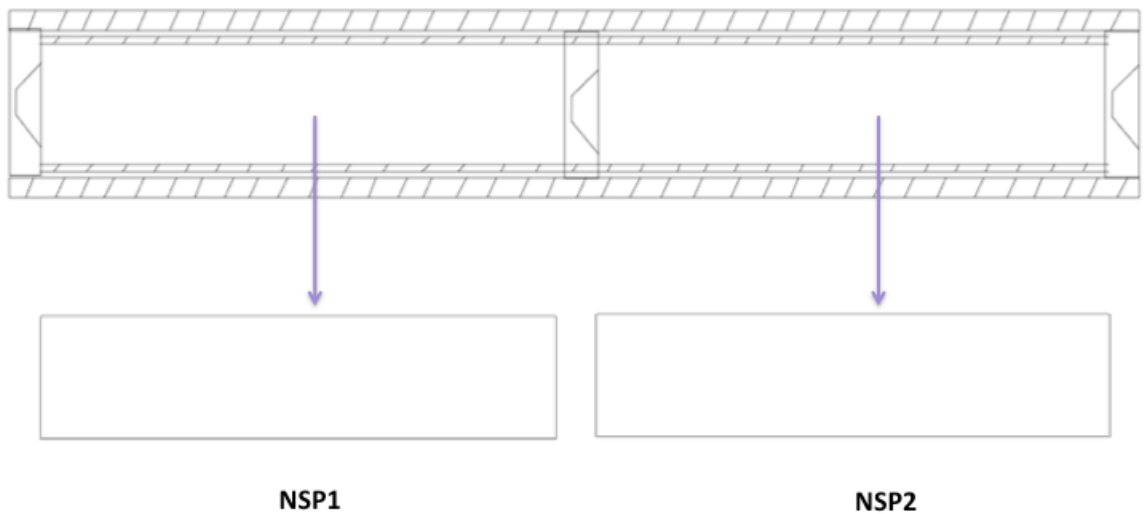
As previously stated, the external parts, specifically the outer cylindrical tubes and mounts, were kept the same. Thus, the apertures and spacers were modified and refabricated. There were three main factors considered in the design process: first, optimization of the aperture center hole size; second, optimization of the aperture shape; and third, the length of the spacers, which is essentially the distance between the apertures. In keeping with the original design, two apertures on each side, four in total, were threaded, and one on each side, two in total, are not threaded and held in place by spacers. The preferred design of the apertures is to use a knife-edge, which reduces scattering from the edge of the apertures. The size of the aperture center hole was optimized to be 0.18". Whereas the old apertures were designed to resemble a skimmer, the new apertures are designed with the "cone" facing inwards at a 115°. NAP1, NAP2, and NAP3 all have the same dimensions. NAP1 and NAP3 are threaded whereas NAP2 is not.

Additionally, the new light baffles are designed so the internal apertures are equally spaced along the outer cylindrical tube. The input baffle assembly has welded pieces to the outer cylindrical tube resulting in a groove on the inside where the apertures and spacers are positioned. This complication was crucial because the spacers can no longer be identical; one must be 0.023" less in outer diameter than the other three to fit over the groove. Finally, to further minimize scattered light, the apertures and spacers were coated with colloidal graphite. The figure below

illustrates all these design factors implemented in the new light baffle. They are drawn such that the laser beam enters the input baffle on the NAP1 side. The input and output baffle are still symmetric.



**A**



**B**

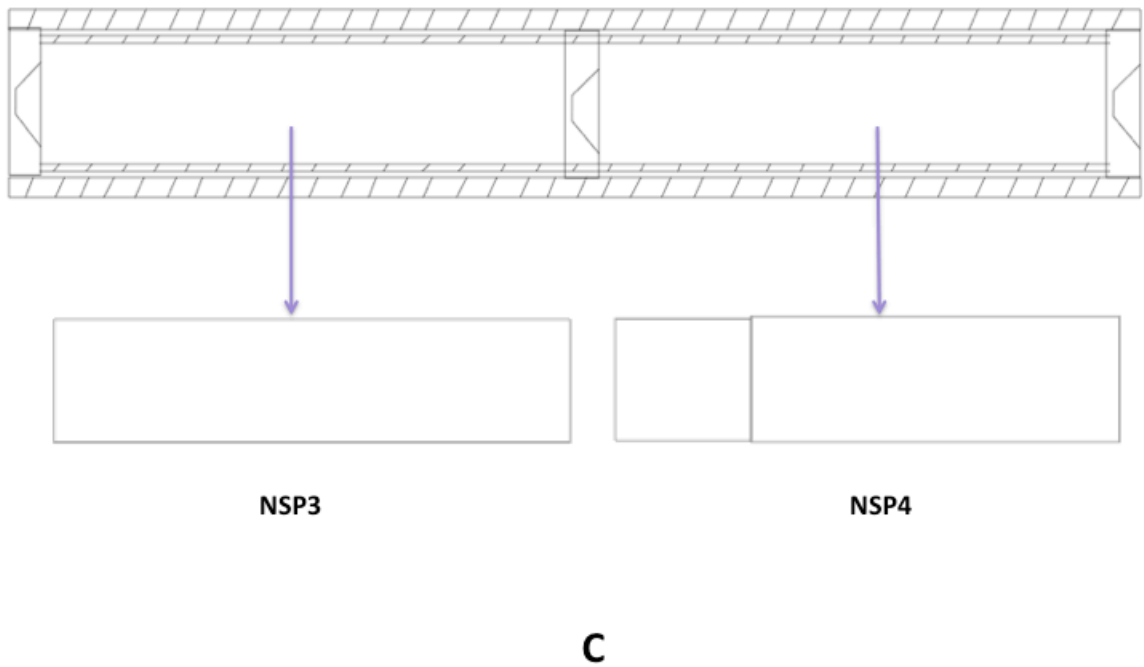


Figure 2.35: This is a schematic of the new light baffle where NAP1 is the input aperture. **A)** This shows the design of the new apertures used. The diameter of the center hole is 0.18" and is the same on all three apertures. NAP1 and NAP3 are threaded whereas NAP2 is not. The location of the apertures is the same in both the input and output baffle. **B)** This shows the spacers on the output baffle side. The spacers are identical with each having an outer diameter of 1.479", and inner diameter of 1.4", and a total length of 8". They are made from stainless steel **C)** This shows the spacers on the input light baffle. The inner diameter of the stainless steel tubes is the same. The outer diameter of most of the tube is 1.497", identical to the output baffle side; the length of that portion is 6.25". The other, smaller region has an outer diameter of 1.474" and a length of 1.75".

## REFERENCES

1. M. A. Duncan. *Rev. Sci. Instr.*, **83** (4), 1101 (2012).
2. G. Ganteför, H. R. Siekmann, H. O. Lutz, and K. H. Meiwes-Broer. *Chem. Phys. Lett.*, **165** (4), 293 (1990).
3. M. Yamashita and J. B. Fenn. *J. Phys. Chem.*, **88** (20), 4451 (1984).
4. M. Yamashita and J. B. Fenn. *J. Phys. Chem.*, **88** (20), 4671 (1984).
5. L.-S. Wang and X.-B. Wang. *J. Phys. Chem. A*, **104** (10), 1978 (2000).
6. L.-S. Wang, C.-F. Ding, and X.-B. Wang. *Rev. Sci. Instr.*, **70**, 1957 (1999).
7. X.-B. Wang and L.-S. Wang. *Rev. Sci. Instr.*, **79** (7), 3108 (2008).
8. M. Z. Kamrath, R. A. Relph, T. L. Guasco, C. M. Leavitt, M. A. Johnson. *Int'l. J. Mass Spec.*, **300** (2), 91 (2011).
9. C. Yiu-Ng and M. Baer. *Adv. Chem. Phys. Ser.*, **82**, 1 (1992).
10. J. Q. Searcy and J. B. Fenn. *J. Chem. Phys.*, **61**, 5282 (1974).
11. R. E. Smalley, L. Wharton, and D. H. Levy. *Acc. Chem. Res.*, **10** (4), (1977).
12. P. Auroy, Y. Mir, and L. Auvray. *Phys. Rev. Lett.*, **69**, 93 (1992).
13. M. Hartmann, R. E. Miller, J. P. Toennies, and A. Vilesov. *Phys. Rev. Lett.*, **75**, 1566 (1995).
14. W. H. Robertson, J. A. Kelley, and M. A. Johnson. *Rev. Sci. Instr.*, **71**, 4431 (2000).
15. E. C. Fest. *Stray Light Analysis and Control*, SPIE Press (2013).

### **CHAPTER 3: ON THE PHOTOIONIZATION SPECTRUM OF PROPYNE**

On the Photoionization Spectrum of Propyne: A Fully ab Initio Simulation  
of the Low-Energy Spectrum Including the Jahn-Teller Effect and the Spin-Orbit  
Interaction

Sara A. Marquez,\* Joseph Dillon\* and David R. Yarkony\*  
Department of Chemistry, Johns Hopkins University  
Baltimore, MD 21218  
United States

–Abstract:

The low energy photoionization spectrum of propyne ( $\text{CH}_3\text{-CCH}$ ) which reveals the vibronic structure of the propyne cation, is simulated using vibronic coupling theory. The spin-orbit interaction is included using an intensity borrowing approach, enabling determination of the ( $\tilde{X}^2E_{1/2,3/2}, v = 0$ ) splitting and the relative photoionization intensity of these closely spaced levels. The results are compared with recent experimental studies and misstatements are corrected.

## I. INTRODUCTION

Propyne, methyl acetylene,  $\text{CH}_3\text{-C}\equiv\text{C-H}$ , plays an important role in combustion processes where it is known to contribute to the formation of polycyclic aromatic hydrocarbons.<sup>1</sup> Ground state spectra<sup>2,3</sup> and photodissociation measurements<sup>4</sup> of propyne have been reported. Photoionization studies,<sup>5-8</sup> which reveal the spectrum of the propyne cation, have also been reported, as have high resolution pulsed-field ionization (PFI) zero-kinetic-energy (ZEKE) photoelectron spectra<sup>9</sup> and vacuum ultraviolet (VUV) laser pulsed field ionization-photoelectron (PFI-PE) measurements.<sup>10</sup>

The ground electronic state of neutral propyne is well described as a closed shell  $^1A_1$  state with  $C_{3v}$  symmetry.<sup>10</sup> The highest occupied molecular orbital (HOMO) is an e orbital, corresponding to the  $\pi$ -orbitals of the C-C triple bond. Consequently, the cation, is a  $^2E$  state, which is subject to a first order Jahn-Teller<sup>11</sup> distortion and spin-orbit induced splitting of the  $^2E$  state<sup>9,10</sup> into Kramers' doublets.<sup>12</sup> The PFI measurements, by Matsui et al., denoted MZG below, resolved spin-orbit structure in the rotational profile of the origin band in the nonresonant two-photon threshold photoionization of propyne. MZG report that this band is well simulated by a simple model that uses the spin-orbit splitting of the acetylene cation ( $A = -30.9 \text{ cm}^{-1}$ , ref 13) and a propyne cation structure that is very close to that of the neutral ground state, implying minimal impact of the Jahn-Teller interaction. More recently, Xing et al., denoted XBRLN below, have obtained rotationally resolved spectra for  $\text{C}_3\text{H}_4^+$  ( $\tilde{X}^2E_{3/2,1/2}, v_1^+ = 1$ ). They find the best fit spin-orbit constant to be  $A = -13.0 \pm 0.2 \text{ cm}^{-1}$  and the ratio of the photoionization cross-sections to be  $E_{1/2}/E_{3/2} = 4:1$ . The

acetylenic  $A$  constant and the small Jahn-Teller distortion, used by MZG although self-consistent, are at odds with  $A = -13.0 \text{ cm}^{-1}$  of XBRLLN. The contradiction arises since the observed  $A = -13.0 \text{ cm}^{-1}$  of XBRLLN implies significant Ham reduction<sup>14</sup> of the pure acetylene-like  $A$  of  $-30 \text{ cm}^{-1}$  utilized in MZG, which implies a consequential Jahn-Teller effect.

Thus the work of MZG and XBRLLN on propyne photoionization reach fundamentally different conclusions concerning the importance of the Jahn-Teller effect in the electronic structure of the propyne cation. In this work, we will address these differences. The ground electronic state of propyne, and the  $1,2^2A$  states of the propyne cation will be determined using single reference and multireference configuration interaction (MRCI) wave functions, respectively. These results will be used to simulate the photoionization spectrum of propyne using the vibronic coupling model espoused by Köppel, Domcke and Cederbaum,<sup>15-18</sup> denoted KDC theory, with the spin-orbit effect included within the Breit-Pauli approximation<sup>19</sup> using an intensity borrowing approach.<sup>20</sup> The simulated photoelectron spectrum provides information concerning the coupling of the spin-orbit and Jahn-Teller effects that cannot be obtained from a pure electronic structure calculation and will allow us to address the discrepancies between the works of MZG and XBRLLN. Section II reviews our theoretical approach. Section III presents the computational results, the propyne electronic structure, and its photoionization spectrum. Section IV summarizes and discusses directions for further research.

## II. THEORETICAL APPROACH

Since the spin-orbit interaction to be included in these calculations is a



relativistic effect, we will refer to calculations that include (do not include) the spin-orbit interaction as relativistic (nonrelativistic). In this work, the relativistic simulation of the spectrum is obtained from a two step procedure, which starts with a nonrelativistic simulation and then obtains the relativistic spectrum using an intensity borrowing approach.<sup>18,20</sup> An alternative single step approach has been introduced by Poluyanov, Domcke, and co-workers.<sup>21-34</sup> In this approach, symmetry is directly incorporated into both the spin and orbital bases, leading to significant formal insights. Particularly relevant to the current work are the recent studies of transition metal trifluorides,<sup>23,24</sup> which are  $C_3$  Jahn-Teller molecules. Also relevant in the present context is the excellent review of the Jahn-Teller effect by Barckholtz and Miller.<sup>35</sup>

In this section, the two step procedure is reviewed to facilitate the discussion in section III.

### **A. Simulating a Photoionization Spectrum: Nonrelativistic Treatment.**

The nonrelativistic spectral intensity distribution function for photoionization is given by<sup>15</sup>

$$I(E) = 2\pi \sum_f |A_f^i|^2 \delta(E - (E_f - E_i)) \quad A_f^i = \langle f | \mu | i \rangle \quad (1)$$

Here  $|i\rangle$ , the initial state, is assumed to be well described by an adiabatic electronic state, in its ground vibrational level;  $|f\rangle$ , the final state, is a nonadiabatic, vibronically coupled state; and  $\mu$  is a transition moment operator.

The initial state,  $|i\rangle$  has the form

$$|i\rangle = \Psi_0^a(\mathbf{r}^{N^{el}+1}; \mathbf{Q}) \theta_{\mathbf{I}}^0(\mathbf{w}') \quad (2)$$

where  $\Psi_0^a$  is an adiabatic electronic state for a molecule with  $N^{el} + 1$  electrons, satisfying the nonrelativistic electronic Schrödinger equation

$$[H^{e,0}(\mathbf{r}^{N^{el}+1}, \mathbf{Q}) - E^{a,0}(\mathbf{Q})] \Psi_0^a = 0, \text{ and } H^{e,0} \text{ is the electronic Hamiltonian in the}$$

nonrelativistic or Coulomb approximation. The vibrational wave function,  $\theta_{\mathbf{I}}^0(\mathbf{w}')$ ,

is given by the multimode product,

$$\theta_{\mathbf{I}}^0(\mathbf{w}') = \prod_{j=1}^{N^{int}} \chi_{I_j}^{0,j}(w_j') \quad (3)$$

where  $\mathbf{w}' = \mathbf{T}'(\mathbf{Q} - \mathbf{Q}^{a,min})$  are the normal modes of the harmonic potential for the initial state, with equilibrium geometry  $\mathbf{Q}^{a,min}$  and  $Q_k, 1 \leq k \leq N^{int}$  are a set of  $N^{int} = 3N^{at} - 6$  internal coordinates.  $\chi_m^{0,j}$  denotes the  $m^{\text{th}}$  harmonic oscillator function corresponding to the  $j^{\text{th}}$  mode of the harmonic potential generated by  $\Psi_0^a$ . The vibrational levels are represented by an  $N^{int}$  dimensional vector  $\mathbf{I} = (I_1, I_2, \dots, I_{N^{int}})$ , where  $I_m$  indicates the number of phonons in the  $m^{\text{th}}$  mode, and  $\mathbf{I} = \mathbf{0}$  is the ground vibrational state.

The wave function for the final state, which satisfies the Schrödinger equation

$$(H^{T,nr} - E_f^{T,nr})|f\rangle = \mathbf{0} \quad (4)$$

where  $H^{T,nr} = T^{nuc} + H^{e,0}(\mathbf{r}^{N^{el}}, \mathbf{Q})$  and  $T^{nuc}$ , the nuclear kinetic energy operator, is expanded as a sum of vibronic products, that is

$$|f\rangle = \sum_{\alpha=1}^{N^{state}} \Psi_{\alpha}^d(\mathbf{r}^{N^{el}}; \mathbf{Q}) \Theta_{\alpha}^f(\mathbf{w}) \quad (5)$$

where  $\Psi_{\alpha}^d$  are diabatic electronic states and  $\mathbf{w} = \mathbf{T}(\mathbf{Q}-\mathbf{Q}^0)$ . The vibrational wave functions  $\Theta_{\alpha}^f(\mathbf{Q})$  in eq 5 are expanded as a sum of the multimode products, that is

$$\Theta_{\alpha}^f(\mathbf{w}) = \sum_{\mathbf{m}} d_{\alpha,\mathbf{m}}^f \theta_{\mathbf{m}}^{\alpha}(\mathbf{w}) = \sum_{\mathbf{m}} d_{\alpha,\mathbf{m}}^f \prod_{i=1}^{N^{int}} \chi_{m_i}^i(w_i) \quad 0 \leq m_i < M_i \quad (6)$$

The same multimode basis will be used for each electronic state, that is  $\chi_m^{0,j}$  is independent of  $\alpha$ , for  $\alpha > 0$ , an approximation that is essential to the efficiency of the computational approach.

Inserting eqs 5 and 6 into eq 4, multiplying by  $\Psi_{\alpha}^d(\mathbf{r}^{N^{el}}; \mathbf{Q}) \theta_{\mathbf{m}}^{\alpha}(\mathbf{w})$ , and integrating successively with respect to  $\mathbf{r}^{N^{el}}$  and  $\mathbf{w}$ , we get<sup>18</sup>

$$\begin{pmatrix} \mathbf{H}_{1;1}^{vib,nr} & \mathbf{H}_{1;2}^{vib,nr} & \dots & \mathbf{H}_{1;N^{state}}^{vib,nr} \\ \mathbf{H}_{2;1}^{vib,nr} & \mathbf{H}_{2;2}^{vib,nr} & & \mathbf{H}_{2;N^{state}}^{vib,nr} \\ \cdot & & \cdot & \cdot \\ \mathbf{H}_{N^{state};1}^{vib,nr} & \mathbf{H}_{N^{state};2}^{vib,nr} & \dots & \mathbf{H}_{N^{state};N^{state}}^{vib,nr} \end{pmatrix} \begin{pmatrix} \mathbf{d}_1^f \\ \mathbf{d}_2^f \\ \cdot \\ \mathbf{d}_{N^{state}}^f \end{pmatrix} = E_k^{T,nr} \begin{pmatrix} \mathbf{d}_1^f \\ \mathbf{d}_2^f \\ \cdot \\ \mathbf{d}_{N^{state}}^f \end{pmatrix} \quad (7)$$

where each  $\mathbf{H}^{vib,nr}$  is an  $N^{vib} \times N^{vib}$  matrix given by

$$H_{\gamma,\mathbf{m};\gamma',\mathbf{m}'}^{vib,nr} = \left\langle \theta_{\mathbf{m}}^{\gamma}(\mathbf{w}) \middle| H_{\gamma,\gamma'}^d(\mathbf{Q}) \middle| \theta_{\mathbf{m}'}^{\gamma'}(\mathbf{w}) \right\rangle_{\mathbf{w}} \quad (8)$$

each  $\mathbf{d}_j^f$  is a  $N^{vib}$  dimensional vector,  $N^{vib} = \prod_{i=1}^{N^{int}} M_i$ ,

$$H_{\alpha,\beta}^d(\mathbf{Q}) = \left\langle \Psi_{\alpha}^d(\mathbf{r}^{N^{el}}; \mathbf{Q}) \middle| H^0(\mathbf{r}^{N^{el}}, \mathbf{Q}) \middle| \Psi_{\beta}^d(\mathbf{r}^{N^{el}}; \mathbf{Q}) \right\rangle_{\mathbf{r}^{N^{el}}} \quad (9)$$

and we have used the (approximate) diabaticity of  $\Psi_\alpha^d(\mathbf{r}^{N^{el}}; \mathbf{Q})$  in deriving eq 7.

The construction of  $H_{\alpha\beta}(\mathbf{Q})$  from ab initio electronic structure data is a significant issue in the spectral simulation and is discussed in section III.  $N^{vib}$  is routinely in the tens to hundreds of millions and can often exceed  $10^9$ . The techniques required to treat such large expansions are discussed in refs 16 and 36.

Using eqs 2 and 7, the amplitude for the transition,  $f \leftarrow \mathbf{I}$ , reduces to

$$A_f^{\mathbf{I}} = \sum_\gamma \langle \Theta_\gamma^f(\mathbf{w}) | \mu^{\gamma,0} | \Theta_{\mathbf{I}}^0(\mathbf{w}') \rangle \approx \sum_\gamma \mu^{\gamma,0} \langle \Theta_\gamma^f(\mathbf{w}) | \Theta_{\mathbf{I}}^0(\mathbf{w}') \rangle$$

$$| \Theta_{\mathbf{I}}^0(\mathbf{w}') \rangle = \sum_{\mathbf{m}, \gamma} d_{\gamma, \mathbf{m}}^f [\mu^{\gamma,0} o(\mathbf{m}, \mathbf{I})] = \mathbf{s}^\dagger \mathbf{d}^f \quad (10)$$

where

$$\mu^{\gamma,0} = \langle \Psi_0^a | \mu | \Psi_\gamma^d \rangle_{\mathbf{r}^{N^{el}+1}}, \quad s_{\gamma, \mathbf{m}} = \mu^{\gamma,0} o(\mathbf{m}, \mathbf{I})$$

$$o(\mathbf{m}, \mathbf{I}) = \left\langle \prod_{i=1}^{N^{int}} \chi_{m_i}^{\alpha, i}(Q_i) \middle| \prod_{j=1}^{N^{int}} \chi_{I_j}^{0, j}(Q'_j) \right\rangle \quad (11a)$$

and

$$s_{\alpha, \mathbf{m}} = \mu^{\alpha, 0} o(\mathbf{m}, \mathbf{I}). \quad (11b)$$

The approximate equality in eq 10 makes the standard assumption that  $\mu^{\gamma,0}(\mathbf{Q})$  is independent of  $\mathbf{Q}$ . The vector of Franck-Condon factors  $o(\mathbf{m}, \mathbf{I})$  has length  $N^{vib}$ . The  $o(\mathbf{m}, \mathbf{I})$  are evaluated using a fine grained parallel algorithm<sup>37,38</sup> based on well-known recursion relations.<sup>39-42</sup> As discussed in ref 16, the evaluation of  $\mathbf{s}^\dagger \mathbf{d}^f$ , the dot product of two vectors of dimension  $N^{state} N^{vib}$ , is readily determined if  $\mathbf{s}$  is used as the seed or initial guess vector in the Lanczos procedure used to determine  $\mathbf{d}^f$ .

Finally note that  $|f\rangle$  is a  $N^{el}$ , rather than  $N^{el}+1$  electron wave function.

Therefore, although the wave function can provide a correct description of the

photoionized species, it cannot accurately describe  $\mu^{\gamma,0}(\mathbf{Q})$  since the outgoing electron is ignored. This limitation will not affect the present calculations since the  $\mu^{\gamma,0}(\mathbf{Q})$ ,  $\gamma = 1, 2$ , are equal by symmetry and we only require relative intensities.

## B. Simulating a Photoionization Spectrum: Relativistic Effects, Intensity Borrowing.

The relativistic eigenstates  $|m^{so}\rangle$ , which satisfy the total relativistic Schrödinger equation

$$(H^{T,so} - E_m^{T,so})|m^{so}\rangle = 0 \quad (12a)$$

are expanded in the nonrelativistic eigenbasis,  $|f\rangle$ . Here

$$H^{T,so} = [T^{nuc} + H^{e,0}(\mathbf{r}^{N^{el}}; \mathbf{Q})] + H^{so}(\mathbf{r}^{N^{el}}; \mathbf{Q}) \equiv H^{T,nr} + H^{so}(\mathbf{r}^{N^{el}}; \mathbf{Q}) \quad (12b)$$

where  $H^{so}$  is the spin-orbit operator in the Breit-Pauli approximation<sup>43</sup>

$$H^{so}(\mathbf{r}^{N^{el}}; \mathbf{Q}) = \sum_{i=1}^{N^{el}} \mathbf{h}^{so,l-2}(\mathbf{r}_i, \mathbf{Q}) \cdot \mathbf{s}_i \quad (13)$$

and  $\mathbf{h}^{so,l-2}$  includes the one (spin-orbit) and two electron (spin-same orbit and spin-other orbit) parts of the Breit-Pauli spin-orbit operator.<sup>43</sup>

In order to explain the form of the eigenstates, the spin quantum numbers of  $\Psi_{\alpha}^d(\mathbf{r}^{N^{el}}; \mathbf{Q})$  must be specified. Since we are concerned with photoionization from singlet states, the  $\Psi_{\alpha}^d$  are doublets, which we denote  $\Psi_{\alpha}^{d, M_s}$  where  $M_s = \pm 1/2$ . We work in the time reversal adapted electronic basis<sup>44,45</sup>

$$\Psi_{\alpha}^{d, \pm} = \frac{\pm 1}{\sqrt{2}} (\Psi_{\alpha}^{d, 1/2} \pm i \Psi_{\alpha}^{d, -1/2}) \quad (14)$$

which is briefly reviewed in ref 18. Replacing  $\Psi_\alpha^d$  in eq. (7) with  $\Psi_\alpha^{d,\pm}$ , the eigenstates of  $H^{T,nr}$  can be written as

$$\left| f^p \right\rangle = \sum_{\mathbf{m}, \alpha} \Psi_\alpha^{d,p}(\mathbf{r}^{N^{el}}; \mathbf{Q}) d_{\alpha, \mathbf{m}}^f \prod_{i=1}^{N^{int}} \chi_{m_i}^i(Q_i) \quad p = \pm \quad (15)$$

Since the nonrelativistic energies are independent of  $p$ , these states come in degenerate pairs, Kramers' doublets. Using the lowest  $N^{eig}$  nonrelativistic eigenstates (of  $H^{T,nr}$ ) as the basis, the  $|m^{so}\rangle$  are expanded as

$$\left| m^{so} \right\rangle = \sum_{\substack{p=\pm \\ k=1-N^{eig}}} c_{p,k}^m \left| k^p \right\rangle \quad (16)$$

By inserting eqs 15 and 16 into eq 12a, we find for the case of two electronic states, after some tedious but straightforward algebra,

$$\begin{pmatrix} \mathbf{E}^{T,nr} + i\mathbf{H}_Y^{A,so} & i\mathbf{H}_Z^{A,so} + \mathbf{H}_X^{A,so} \\ i\mathbf{H}_Z^{A,so} - \mathbf{H}_X^{A,so} & \mathbf{E}^{T,nr} - i\mathbf{H}_Y^{A,so} \end{pmatrix} \begin{pmatrix} \mathbf{c}_+^m \\ \mathbf{c}_-^m \end{pmatrix} = E_m^{T,so} \begin{pmatrix} \mathbf{c}_+^m \\ \mathbf{c}_-^m \end{pmatrix} \quad (17)$$

where  $E_{k,l}^{T,nr} = \delta_{k,l} E_k^{T,nr}$ ,  $\mathbf{c}_\pm^m = \mathbf{c}_\pm^{m,R} + i\mathbf{c}_\pm^{m,I}$

$$\mathbf{H}_\lambda^{A,so} = \mathbf{O} \mathbf{H}_Y^{rso} \quad (18)$$

$$H_\lambda^{rso} = i \left\langle \Psi_1^{d,1/2} \left| \sum_{i=1}^{N^{el}} h_\lambda^{so,1-2}(\mathbf{r}_i) S_Z(i) \right| \Psi_2^{d,1/2} \right\rangle_{r^{N^{el}}} \quad \lambda = X, Y, Z \quad (19)$$

$$O_{f,l} = \sum_{\mathbf{m}} (d_{1,\mathbf{m}}^f d_{2,\mathbf{m}}^l - d_{2,\mathbf{m}}^f d_{1,\mathbf{m}}^l) \quad 1 \leq f, l \leq N^{eig} \quad (20)$$

and we have neglected the  $\mathbf{Q}$  dependence of  $H_\lambda^{rso}$ . Note that the relativistic Schrödinger equation, eq 12a has become a  $2N^{eig}$  Hermitian matrix eigenvalue problem, eq 17, where the eigenvectors,  $\mathbf{c}^m$  are complex-valued. See ref 18 for details. Since  $|O_{k,l}|$  is less than 1, it has the effect of reducing the effective spin-orbit

interaction (eq 18), and hence, is referred to as a generalized Ham reduction factor.<sup>14</sup>

The only assumptions in eq 17 are that we can neglect the  $\mathbf{Q}$  dependence of  $H_{\lambda}^{rs0}$ ; the interactions with the excluded nonrelativistic vibronic eigenstates in eq 16 ( $f > N^{eig}$ ); and the interactions with the remaining nonrelativistic electronic states. The fact that only one combination of the  $M_s$  values is required in eq 19 is a consequence of the Wigner-Eckart theorem.<sup>43,46,47</sup> As explained in ref 18, inserting eq 16 into eq 1 and assuming, as usual, that the electronic transition moment is independent of  $\mathbf{Q}$ , the relativistic intensity factor,  $A_m^{so,\mathbf{I}}$ , is found to be

$$2 |A_m^{so,\mathbf{I}}|^2 = |\mu^{so,m,\mathbf{I},+}|^2 + |\mu^{so,m,\mathbf{I},-}|^2 \quad (21)$$

where

$$\mu^{so,m,\mathbf{I},\pm} = \sum_{f=1}^{N^{eig}} c_{\mp,f}^m \sum_{\mathbf{m}',\gamma} d_{\gamma,\mathbf{m}'}^f \mu^{\gamma,0} o(\mathbf{m}',\mathbf{I}) = \sum_{f=1}^{N^{eig}} c_{\mp,f}^m \mathbf{s}^{\dagger} \mathbf{d}^f \quad (22)$$

Equation 22, which will be used in this work to determine the relativistic intensity factors, evinces the promised intensity borrowing (sum on  $f$ ) from the nonrelativistic amplitudes  $A_f^{\mathbf{I}} = \mathbf{s}^{\dagger} \mathbf{d}^f$  (see eq. 10).

### III. PHOTOIONIZATION SPECTRUM OF PROPYNE

**A. Electronic Structure Calculations.** Propyne, pictured in Figure 3.1, can be viewed as acetylene with a hydrogen replaced by a methyl ( $\text{CH}_3$ ) group. Both propyne and its cation will be described using cc-p-VTZ bases on carbon and hydrogen. The neutral is well described by a single closed shell reference

configuration, while for the cation a two orbital, three electron complete active space (CAS) is used. As a consequence of the different active spaces, the ionization potential will not be computed here. The CAS describes the  $e^3$  shell in the propyne cation, which originates from the  $\pi^3$  shell of the acetylene cation. The orbitals for the cation were determined from a state averaged multiconfiguration self-consistent field procedure, which averaged two states with equal weights. Dynamic correlation was included at the second order configuration interaction level. These calculations were performed using the COLUMBUS suite of electronic structure programs.<sup>48-50</sup>

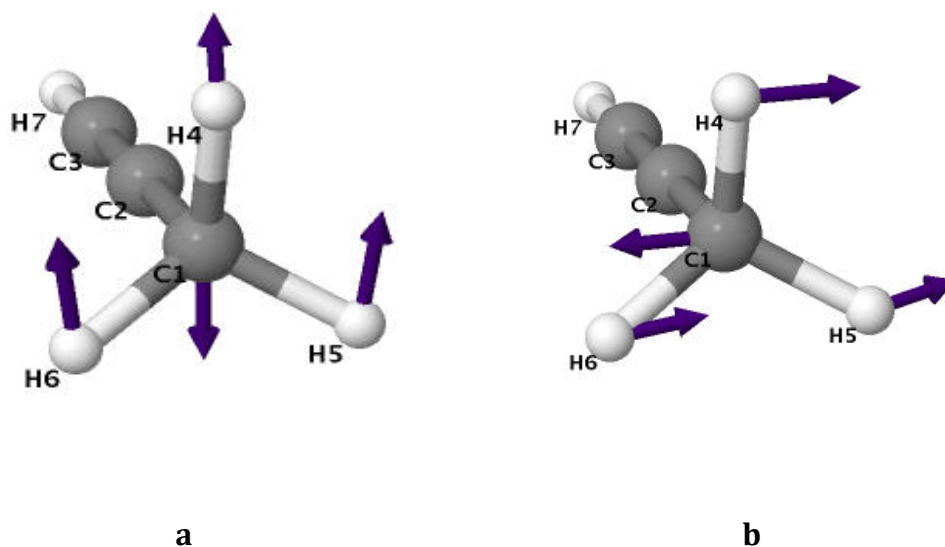


**Figure 3.1.** Propyne cation **g** (a) and **h** (b) vectors, with atom numbering used in this work.

The spin-orbit interaction between the  $1^2A$  and  $2^2A$  states of the propyne cation was obtained using the above-noted wave functions with a Dunning double- $\zeta$  polarized basis on the carbons and hydrogens. These calculations were carried



out with a program,<sup>51</sup> which uses the full one and two electron microscopic Breit-Pauli spin-orbit operator<sup>19,43</sup> (eq 16) and is based on the symbolic matrix element method.<sup>52</sup> Using this methodology  $\mathbf{H}^{rso}$  (eq 19) was found to be (0,0, -14.17) cm<sup>-1</sup>. When the calculation is repeated for the acetylene cation, virtually the same value was obtained for  $\mathbf{H}^{rso}$ , (0,0,-13.8). The acetylene cation result is in good accord with the experimental value  $A^{so}(\text{acetylene}^+) = -30.9$  cm<sup>-1</sup>, ref 13, since  $||\mathbf{H}^{rso}|| \approx A^{SO}/2$ .

**B. Extrema.** Using the wave functions described above, the minimum on the ground state potential energy surface of the neutral, denoted  $min(^1A_1)$ , a cation minimum denoted  $min(^2A')$ , and a transition state, denoted  $ts(^2A'')$ , were located. Also located was the minimum energy conical intersection point, denoted  $mex(^2E_x - ^2E_y)$ , which is taken as the zero of energy for the electronic structure calculations. The geometries, denoted  $\mathbf{Q}(min(^1A_1))$ ,  $\mathbf{Q}(min(^2A'))$ ,  $\mathbf{Q}(ts(^2A''))$ , and  $\mathbf{Q}(mex(^2E_x - ^2E_y))$ , and the energies of these extrema are given in Table 1. From this table, it is evident that the minimum and transition state have  $C_s$  symmetry, while  $mex(^2E_x - ^2E_y)$  and  $min(^1A_1)$  have  $C_{3v}$  symmetry. The  $C_s$  symmetry of  $min(^2A')$  is consistent with the result of XBRLLN. The  $min(^1A_1)$  and  $min(^2A')$  structures are seen to be similar, with changes in the bond length less than 0.05Å, despite the distortion of the cation due to the static Jahn-Teller effect.<sup>11</sup> As a consequence of this  $C_{3v}$  symmetry,  $min(^2A')$  and  $ts(^2A'')$  are each one of three symmetry equivalent structures on the ground state potential energy surface. See Figure 3.2, which depicts the  $^2E$  coupled potential energy surfaces, including the effect of the spin-orbit interaction. This figure clearly evinces the spin-orbit modified conical intersection and three symmetry equivalent minima and transition states.

**Table 3.1. Energies in cm<sup>-1</sup> and Structures of Extrema for C<sub>3</sub>H<sub>4</sub> and C<sub>3</sub>H<sub>4</sub><sup>+a</sup>.**

	<i>min</i> (1 <sup>2</sup> A')		<i>ts</i> (1 <sup>2</sup> A'')		<i>mex</i> (1 <sup>2</sup> E <sub>x</sub> -1 <sup>2</sup> E <sub>y</sub> )		<i>min</i> (1 <sup>1</sup> A <sub>1</sub> )
	ab initio	H <sup>d</sup>	ab initio	H <sup>d</sup>	ab initio	H <sup>d</sup>	ab initio
energy	-117.18	-116.95	-102.94	-102.71	0.00	0.00	
R(C <sup>1</sup> -C <sup>2</sup> )	1.428	1.428	1.428	1.428	1.430	1.430	1.460 [1.454]
R(C <sup>2</sup> -C <sup>3</sup> )	1.241	1.241	1.241	1.241	1.241	1.241	1.194[1.207]
R(C <sup>3</sup> -H <sup>7</sup> )	1.069	1.069	1.069	1.069	1.069	1.069	1.056[1.065]
R(C <sup>1</sup> -H <sup>4</sup> )	1.097	1.097	1.082	1.082	1.088	1.088	1.084[1.094]
R(C <sup>1</sup> -H <sup>5</sup> )	1.085	1.085	1.092	1.092	1.088	1.088	1.084
∠C <sup>2</sup> C <sup>1</sup> H <sup>4</sup>	105.8	105.8	111.7	111.7	109.2	109.2	110.6[119.0]
∠C <sup>2</sup> C <sup>1</sup> H <sup>5</sup>	110.8	110.9	107.9	108.0	109.2	109.2	110.6
∠H <sup>7</sup> C <sup>3</sup> C <sup>2</sup>	179.84	179.85	179.81	179.82	180.00	180.00	180.00

<sup>a</sup> For C<sub>s</sub> symmetry H<sup>5</sup> and H<sup>6</sup> are equivalent. Bond distances in Å; angles in degrees. Density functional results from ref. 8 are in brackets.

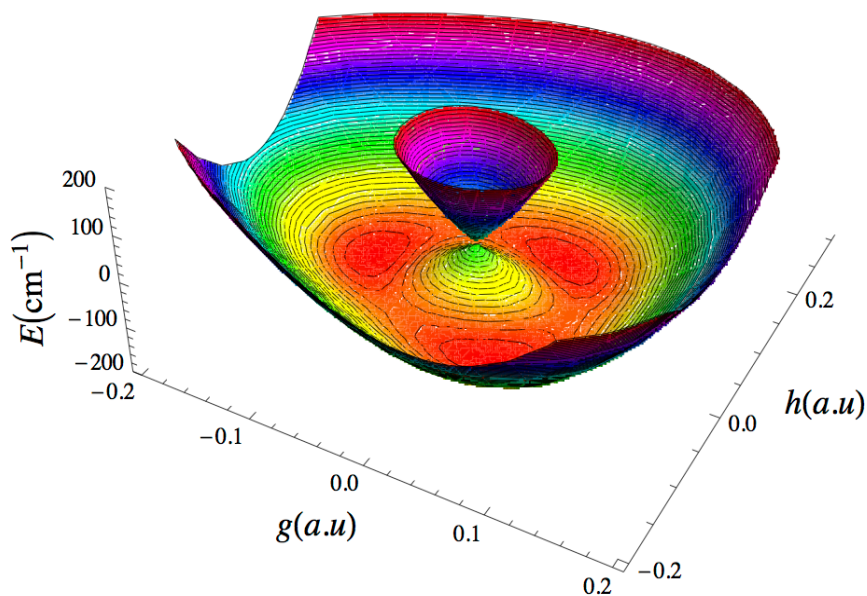


**Figure 3.2.** Three-dimensional plot of the coupled potential energy surfaces used in this work in the **g-h** plane, including the spin-orbit interaction.

Table 3.2 reports the harmonic frequencies at  $min(^1A_1)$ ,  $min(^2A')$ , and  $ts(^2A'')$ , obtained from ab initio Hessians, determined using centered differences of analytic gradients. The harmonic frequency of the acetylenic CH stretch, the  $2a'$  mode in Table 3.2, 3163 (3217)  $cm^{-1}$  is in good accord with the value determined by XBRLLN given parenthetically.

**Table 3.2. Harmonic Frequencies in cm<sup>-1a</sup>**

mode	<i>min</i> (1 <sup>2</sup> A)		<i>ts</i> (1 <sup>2</sup> A)		<i>min</i> (1 <sup>1</sup> A <sub>1</sub> )	
	ab initio	H <sup>d</sup>	ab initio	H <sup>d</sup>	ab initio	
1 a'	3433.5	3431.7	3433.5	3431.7	3565.4	(1a <sub>1</sub> )
2a'	3163.4	3140.1	3234.4	3185.5	3209.1	(1e)
3a'	3048.2	3080.1	3073.6	3094.7	3135.3	(2a <sub>1</sub> )
4a'	2130.4	2125.5	2130.1	2125.5	2300.5	(3a <sub>1</sub> )
5a'	1492.7	1554.3	1480.2	1529.1	1538.4	(2e)
6a'	1395.6	1377.2	1387.0	1360.6	1469.2	(4a <sub>1</sub> )
7a'	1000.1	970.5	1074.2	1102.3	1100.3(1036.1)	(3e)
8a'	906.8	911.1	926.9	922.8	966.3 (930.3)	(5a <sub>1</sub> )
9a'	748.1	784.7	674.2	641.8	713.7 (633.3)	(4e)
10a'	362.0	345.5	354.3	372.9	361.3 (327.5)	(5e)
1a''	3194.3	3169.7	3060.7	3080.0	3209.1	
2a''	1359.1	1354.0	1393.2	1406.4	1538.4	
3a''	701.0	721.3	764.9	791.8	1100.3	
4a''	672.6	631.6	463.9	440.3	713.7	
5a''	319.5	344.1	-446.2	-502.6	361.3	

<sup>a</sup>Results in parentheses are from ref 9. C<sub>3v</sub> labels are in the far right column.

**C. Jahn-Teller Parameters.** The Jahn-Teller parameters are obtained from Table 1. The Jahn-Teller stabilization energy is  $E^{JTS} = E^{a,1,(ab)}(\mathbf{Q}(mex(2E_x - 2E_y))) - E^{a,1,(ab)}(\mathbf{Q}(min(2A')))) = 117.2 \text{ cm}^{-1}$ , and the barrier to pseudo rotation,  $E^{BSR} = E^{a,1,(ab)}(\mathbf{Q}(ts(2A''))) - E^{a,1,(ab)}(\mathbf{Q}(min(2A')))) = 14.24 \text{ cm}^{-1}$ . The latter implies small quadratic Jahn-Teller couplings. Concerning the linear Jahn-Teller coupling, Figure

1 reports the **g** and **h** internal motions, the E-type motions that lift the degeneracy linearly. These are seen to involve principally displacements of the methyl group. All E-type coordinates perpendicular to **g** and **h** lift the degeneracy at quadratic order. The  $\|\mathbf{g}\| = g = 3528 \text{ cm}^{-1}/a_0$ .

**D. Representing the Coupled Potential Energy Surfaces.** As noted in section II, a key step in determining the vibronic states of the cation is the construction of a coupled quasi-diabatic state  $\mathbf{H}^d$ , eq 9, required to build  $\mathbf{H}^{vib,nr}$ , in eq 8. Here, the attribute quasi, or approximate, is used since it is well-known that rigorous diabatic representations do not exist.<sup>53,54</sup> The coupled quasi diabatic state Hamiltonian has the form:

$$H_{\alpha,\beta}^d(\mathbf{w}) = E^{a,J,(ab)}(\mathbf{Q}^0)\delta_{\alpha,\beta} + \sum_{k=1}^{N^{int}} V_k^{(1),\alpha,\beta} w_k + 1/2 \sum_{k,l=1}^{N^{int}} V_{k,l}^{(2),\alpha,\beta} w_k w_l \quad . \quad (23)$$

This  $\mathbf{H}^d$  gives rise to the full quadratic KDC model for photoionization spectra simulations.<sup>15</sup> The unknown coefficients,  $V^{(n),\alpha,\beta}$ , are determined by requiring the adiabatic energies  $E^{a,J,(m)}$  (the  $(m)$  stands for model) and the eigenstates,  $\mathbf{e}^J$  of  $\mathbf{H}^d$ , obtained from

$$\left[ \mathbf{H}^d(\mathbf{Q}) - \mathbf{I}E^{a,J,(m)}(\mathbf{Q}) \right] \mathbf{e}^J(\mathbf{Q}) = \mathbf{0} \quad , \quad (24)$$

to reproduce as well as possible the ab initio energies,  $E^{a,J,(ab)}(\mathbf{Q})$ , energy gradients  $\nabla_k E^{a,J,(ab)}(\mathbf{Q})$ , and derivative coupling vector

$$f_k^{a,J,K,(ab)}(\mathbf{Q}) = \langle \Psi_J^{a,(ab)}(\mathbf{r}^{N^{el}}, \mathbf{Q}) | \nabla_k \Psi_K^{a,(ab)}(\mathbf{r}^{N^{el}}, \mathbf{Q}) \rangle_{\mathbf{r}^{N^{el}}} , \quad 1 \leq k \leq N^{int} ,$$

at a selected set of points,  $\mathbf{Q}^n$ ,  $1 \leq n \leq N^{pnt}$ . Since derivative coupling information is included in the construction of  $\mathbf{H}^d$ , it is quantifiably quasi-diabatic.

Using  $C_{3v}$  symmetry, there are only 4 unique classes of quadratic elements of  $\mathbf{H}^d$  (see ref 55-57):  $\langle ex | O(a_1, a_1) | ex \rangle$ ,  $\langle ex | O(a_1, x) | ex \rangle$ ,  $\langle ex | O(x, x) | ex \rangle$ , and  $\langle ex | O(y, y) | ex \rangle$ . Here, the brackets denote the diabatic electronic states, and  $O(i, j)$  denotes a displacement that transforms as  $i \times j$ . The remaining nonzero elements of the diagonal blocks,  $H_{ey, ey}^d$  and  $H_{ex, ex}^d$  are obtained from the following symmetry relations:

$$\begin{aligned}
 \langle ex | O(a_1, a_1) | ex \rangle &= \langle ey | O(a_1, a_1) | ey \rangle \\
 \langle ex | O(a_1, x) | ex \rangle &= - \langle ey | O(a_1, x) | ey \rangle \\
 \langle ex | O(y, y) | ex \rangle &= \langle ey | O(x, x) | ey \rangle \\
 \langle ex | O(x, x) | ex \rangle &= \langle ey | O(y, y) | ey \rangle
 \end{aligned} \tag{25a}$$

while the nonzero elements of  $H_{ex, ey}^d$  block are obtained from

$$\begin{aligned}
 (\langle ex | O(a_1, x) | ex \rangle &= - \langle ex | O(a_1, y) | ey \rangle \\
 \langle ex | O(x, x) | ex \rangle - \langle ey | O(x, x) | ey \rangle &= 2 \langle ex | O(y, x) | ey \rangle = 2 \langle ex | O(x, y) | ey \rangle
 \end{aligned} \tag{25b}$$

More details concerning the fitting procedure can be found in refs 38 and 58.

In this work,  $N^{\text{pnt}} = 23$ , and includes  $\text{min}(^2A')$ ,  $\text{ts}(^2A'')$  and  $\text{mex}(^2E_x - ^2E_y)$  together with 20 points, arising from  $C_s$  symmetry preserving displacements centered at  $\mathbf{Q}(\text{mex}(^2E_x - ^2E_y))$ . The Supporting Information provides the Cartesian coordinates of these points and describes how they were selected. The data at  $\mathbf{Q}(\text{mex}(^2E_x - ^2E_y))$ , taken as the origin of  $\mathbf{H}^d$ , determine the linear parameters,  $\mathbf{V}^{(1)}$ . The remaining 22  $\mathbf{Q}''$  give 704 symmetry unique equations, for the 70 unique second order parameters,  $\mathbf{V}^{(2)}$ . Since the origin of the fit is  $\mathbf{Q}(\text{mex}(^2E_x - ^2E_y))$ , the energy, energy gradients, and singular part of the derivative coupling at this point are

described exactly. The root-mean-square (rms) energy error for the remaining 22 points included in the fit is  $0.199 \text{ cm}^{-1}$  for the ground state and  $0.737 \text{ cm}^{-1}$  for the excited state. Table 1 (2) compares the ab initio bond distances and bond angles (harmonic frequencies) with those obtained from  $\mathbf{H}^d$ . The agreement is seen to be quite good with the largest error in the bond distance (bond angle) [harmonic frequency] being  $0.009 \text{ \AA}$  ( $0.11^\circ$ ) [ $62 \text{ cm}^{-1}$ ]. Note that the  $\mathbf{H}^d$  determined harmonic frequencies, obtained from divided differences of gradients, require electronic structure data at points not included in the fitting procedure. Another figure of merit is the (degenerate) energy of the cation evaluated at  $\mathbf{Q}(\min(^1A_1))$ , the equilibrium geometry of the neutral, a point again not included in the fit data. The value obtained from  $\mathbf{H}^d$ ,  $E_{a,2,(m)} = E_{a,1,(m)} = 1067 (1145) \text{ cm}^{-1}$  is in good accord with the ab initio result given parenthetically.

**E. Parameters Defining the Nonrelativistic Vibronic Wave Function for the Cation.** To define the nonrelativistic wave function, three things must be specified; (i) the origin of the expansion,  $\mathbf{Q}^0$ , (ii) the normal coordinates for that origin ( $\mathbf{w}$ ), and (iii) the vector  $\mathbf{M}$  that specifies the number of harmonic oscillator functions for each mode included in eq 6. The normal coordinates determined from the Hessian matrix at  $\mathbf{Q}(\min(^1A_1))$  and the corresponding harmonic oscillator functions will be used. The  $\mathbf{M}$ , given in Tables 3 and 4, were chosen so that the reported spectral lines are converged with respect to the harmonic oscillator basis. To help demonstrate the validity of our intensities, two choices for the origin,  $\mathbf{Q}^0$ , were used in this work, the equilibrium geometry of neutral propyne  $\mathbf{Q}^0 = \mathbf{Q}(\min(^1A_1))$  and the minimum energy crossing point  $\mathbf{Q}^0 = \mathbf{Q}(\text{mex}(^2E_x - ^2E_y))$ , both of

which have  $C_{3v}$  symmetry. The resulting bases are denoted the neutral and hybrid bases, respectively. For the neutral basis,  $o(\mathbf{m}, \mathbf{I}) = \delta_{\mathbf{m}, \mathbf{I}}$ . For the hybrid basis,  $\sum_{\mathbf{m}} o(\mathbf{m}, \mathbf{I}) \equiv O_V(\mathbf{I})$ , measures the ability of the basis to describe the initial state and should be  $\sim 1$ . Owing to the choice of origin, the hybrid basis is expected to yield a somewhat more compact vibronic expansion,<sup>37</sup> as defined by  $\mathbf{M}$ . Here, for notational simplicity, we have used the same notation for the origin ( $\mathbf{Q}^0$ ) and normal coordinates ( $\mathbf{w}$ ) to construct  $\mathbf{H}^d$  and for the expansion of  $|f\rangle$  in eq 6. In practice, this is not the case, and the two coordinates systems are interconverted by a linear transformation.

**F. Photoionization Spectra.** The focus of this work is the origin band, the ( ${}^2E, v^+ = 0$ ) levels. However, we will also briefly comment on the near threshold vibrationally excited levels, which will be carefully analyzed in a more complete study of the low energy photoionization spectrum, the subject of a future publication.

Tables 3 and 4 report the nonrelativistic photoionization spectrum of propyne using the hybrid and neutral bases, respectively. See columns labeled NR-converged. The six lowest energy levels are reported. As expected, the converged hybrid basis is much smaller than the converged neutral basis. Here, it is approximately a third the size. This reduction in  $N^{\text{vib}}$  can be understood as follows. Note that the reduction is achieved in large part by the change in  $M_3$  from 6 in the neutral basis to 3 in the hybrid basis. Note too that the  $3_{a1}$  mode is a carbon-carbon triple bond stretch. This change in  $M_3$  is then seen to reflect the fact that in the



hybrid representation the value of  $R(C^2\equiv C^3)$  at the origin  $max(^2E_x - ^2E_y)$  and is equal to its value at  $min(^2A')$ , but in the neutral basis the value of  $R(C^2\equiv C^3)$  at the origin  $min(^1A_1)$  is  $\sim 0.047$  Å shorter than the value at  $min(^2A')$  (see Table 1).

**Table 3.3. Hybrid Basis: M= 3,2,3,2,2; 3,4,6,3,4; 3,4,6,3,4, (2,2,3,2,2; 2,3,5,2,4; 2,3,5,2,4);  $N^{vib}N^{state} = 107,495,424$  (5,529,600);  $Ov(0) = 0.992042(0.992013)$ ; Reduced Basis Parameters Given Parenthetically; in M, the Modes Are in the Order (1 - 5a<sub>1</sub>; 1 - 5e<sub>x</sub>; 1 - 5e<sub>y</sub>); Reported Rel-Reduced Simulation Based on  $N^{eig} = 100$ ; Energies in cm<sup>-1</sup>**

level	NR-Converged		NR-Reduced		Rel-Reduced	
	energy	intensity	energy	intensity	energy	intensity
1	0.000	1.00	0.00	1.00	0.0	1.00
2	0.002	1.00	0.014	1.00	18.57	0.99
3	327.9	0.00	328.0	0.00	333.15	0.00
4	339.8	0.0	339.7	0.00	353.20	0.00
5	377.7	0.05	377.6	0.05	378.99	0.06
6	377.8	0.05	377.7	0.05	395.01	0.05

**Table 3.4. Neutral Basis: M = 2,2,6,3,3; 3,4,6,3,4; 3,4,6,3,4 (2,1,4,3,3; 2,4,4,3,4; 2,4,4,3,4);  $N^{\text{vib}}N^{\text{state}} = 322,486,272$  ( 21,233,664); in M the Modes Are in the Order(1 - 5a<sub>1</sub>; 1 - 5e<sub>x</sub>; 1 - 5e<sub>y</sub>); Reduced Basis Parameters Given Parenthetically; Reported Rel-Reduced Simulation Based on  $N^{\text{eig}} = 100$ ; Energies in cm<sup>-1</sup>**

level	NR-converged		NR-reduced		Rel-reduced	
	energy	intensity	energy	intensity	energy	intensity
1	0.000	1.00	0.00	1.00	0.0	1.00
2	0.049	1.00	0.222	1.00	18.65	0.99
3	331.839	0.00	332.803	0.00	337.90	0.00
4	344.325	0.00	344.603	0.00	358.07	0.00
5	381.951	0.05	381.766	0.05	383.02	0.06
6	382.005	0.05	381.849	0.05	399.20	0.05

(i). ( ${}^2E, v^+ = 0$ ) Levels. The most intense lines in Tables 3 and 4 are the ( ${}^2E, v^+ = 0$ ) ground state levels, which are degenerate by symmetry in the absence of spin-orbit coupling. In the present calculations, the degeneracy is computed, using the hybrid (neutral) basis, to be 0.002 (0.049) cm<sup>-1</sup>. Considering the size of the spin-orbit interaction, the stringent degeneracy of these levels is essential for a convincing analysis of the relativistic simulation, which follows. The inconsequential approximately 5 cm<sup>-1</sup> systematic difference in roots 3-6 for the two bases is most likely due to the approximate treatment of the kinetic energy in the time-independent KDC method.<sup>15</sup>

We now turn to the effect of the spin orbit interaction on the ( ${}^2E, v^+ = 0$ ) levels of the photoionization spectrum. There are two issues to be addressed: the relative intensity and spacing of the two lowest energy levels in the spectrum. As noted above, in the nonrelativistic spectrum these two levels form the degenerate components of a vibronic  ${}^2E$  state and are of equal intensity symmetry. When the spin-orbit interaction is included, the  ${}^2E$  state splits into two Kramers' doublets, usually denoted  ${}^2E_{3/2}$  and  ${}^2E_{1/2}$ , with the coupling among the nonrelativistic levels, eq 22, providing the mechanism for intensity borrowing. Differential mixing of the nonrelativistic levels can remove the original degeneracy of the nonrelativistic intensities. The state labels  ${}^2E_{3/2}$  and  ${}^2E_{1/2}$ , are a little misleading since these states are actually the  $E'_1$  and  $E'_2$  representation of the  $C_{3v}$  double group.  $E'_2$  is a true two-dimensional representation, while  $E'_1$  is composed of two one-dimensional irreducible representations<sup>59</sup> degenerate by time reversal symmetry.

To carry out the requisite relativistic calculation, it is computationally convenient to use an expansion with reduced  $N^{\text{vib}}$  for the nonrelativistic spectrum since the eigenvectors are required; see eqs 18 and 20. The results of the reduced dimensional expansion are reported in columns labeled NR-reduced in Tables 3 and 4. By comparing columns NR-converged and NR-reduced in Tables 3 and 4, it is seen that this truncation has a small effect on the calculated energy levels.

The relativistic spectral intensity distribution function for the photoionization spectrum of propyne is also reported in Tables 3 and 4; see column Rel-reduced. Here, we use  $N^{\text{eig}} = 100$ , but the attributes of the reported levels do not change if  $N^{\text{eig}}$  is increased. The splitting of the first two levels is seen to be only  $A^{\text{so}}$

= -18.6 cm<sup>-1</sup>, considerably reduced from the pure electronic splitting, which has magnitude  $2 || \mathbf{H}^{rs0} || = 28.2$  cm<sup>-1</sup>. This result is in reasonable accord with the result of XBRLLN who found  $A^{so} = -13.2$  cm<sup>-1</sup>.

It is clear, however, from Table 3 that the intensities of the <sup>2</sup>E<sub>3/2</sub> and <sup>2</sup>E<sub>1/2</sub> states are essentially equal. Reference to the nonrelativistic spectrum provides a clear explanation for this. The two lowest nonrelativistic levels are separated from the remaining levels by, at least, ~330 cm<sup>-1</sup>. Since the Ham reduced spin-orbit interaction, eq 18, is < 15 cm<sup>-1</sup>, sufficient differential mixing, eq 22, does not exist to produce a photoionization cross section ratio  $E_{1/2}/E_{3/2} = 4:1$  for the ground vibrational level as reported by XBRLLN.

Consequently, we communicated a preprint of this work to C. Y. Ng, the N in XBRLLN. He pointed out that the reported 4:1 ratio is inconsistent with Figure 1 in XBRLLN, which expresses the observed ground state spectrum in terms of  $C_3H_4^+(^2E_{3/2}, \nu^+ = 0)$  and  $C_3H_4^+(^2E_{1/2}, \nu^+ = 0)$  contributions. From that figure, he concluded that the ratio 1:1 predicted here is quite reasonable.

(ii). (<sup>2</sup>E,  $\nu^+ > 0$ ) Levels. MZG report little evidence for photoionization terminating at excited vibronic levels of propyne cation. However, ref 7, denoted HLWC below, used synchrotron radiation to measure vibronic energies for the photoionization transitions, (<sup>2</sup>E,  $\nu^+$ ) ← (<sup>1</sup>A<sub>1,ν</sub>) for  $\nu = 0$  and for an extended range of  $\nu^+$ , as well as a hot band with  $\nu^+ = 0$  and  $\nu_{5e} = 1$ . The hot band line 347 (361) cm<sup>-1</sup> below threshold, is in good agreement with the harmonic frequency (<sup>1</sup>A<sub>1,ν<sub>5e</sub>=1</sub>) from Table 2 given parenthetically.

The remainder of this discussion considers the two lowest levels above threshold reported by HLWC. The analysis uses the results of Tables 3 or 4 and a related theoretical analysis of Barckholtz and Miller<sup>35</sup> and focuses on the line intensities rather than positions. The levels in question are reported by HLWC at 177 and 314  $\text{cm}^{-1}$  above threshold and are attributed to Jahn-Teller multiplets of  $\nu_{5e^+} = 1$ . In the nonrelativistic approximation, since  $\nu_{5e^+}$  is an e mode, ( ${}^2E, \nu_{5e^+} = 1$ ) gives rise to three vibronic levels with symmetry  $a_1$ ,  $a_2$ , and e. A small splitting of  $a_1$  and  $a_2$  levels is expected since these levels are degenerate in the absence of quadratic coupling,<sup>35</sup> and as noted previously, the quadratic coupling is small in the propyne cation. More significantly only the photoionization intensity of the e levels is expected to be nonzero (see ref 35 Figure 14). These expectations are borne out in the nonrelativistic results for levels 3-6 in Tables 3 and 4. The incorporation of spin-orbit coupling could give intensity to the  $a_1$  and  $a_2$  modes and would be expected to split the e mode. Indeed, Tables 3 and 4 show that incorporation of the spin-orbit interaction increases the splitting of the e levels (levels 5 and 6) by  $\sim 16 \text{ cm}^{-1}$  consistent with the reduced spin-orbit coupling discussed above but does not change the computed intensities. Thus, on the basis of this analysis, we assign, in agreement with HLWC, the measured line at 314  $\text{cm}^{-1}$  to the spin-orbit split e levels originating from ( ${}^2E, \nu_{5e^+}$ ) calculated to be at 378–395  $\text{cm}^{-1}$ . However, on the basis of the expected intensities, the line at 177  $\text{cm}^{-1}$  is likely part of a hot-band sequence, originating at ( ${}^1A_1, \nu_{5e} = 1$ ), for which the intensity of the  $a_1$  line is expected to be significant.<sup>35</sup> Simulation of photoionization spectrum reported by HLWC will

require a very accurate treatment of the vibronic coupling problem and will be undertaken as part of a future study.

As reported by XBRLN, the ( ${}^2E$ ,  $\nu_1^+ = 1$ ) level of the propyne cation's acetylenic CH stretch occurs at  $3217\text{ cm}^{-1}$ .<sup>10</sup> At this energy, a much higher density of states and differential intensity borrowing for the ( ${}^2E_{3/2}$ ,  $\nu_1^+ = 1$ ) and ( ${}^2E_{1/2}$ ,  $\nu_1^+ = 1$ ) levels are possible. However, our current calculations are not sufficiently accurate to address this issue.

#### IV. SUMMARY AND CONCLUSIONS

The electronic structure of the  $1,2^2A$  states (a  ${}^2E$  state for  $C_{3v}$  structures) of the propyne cation has been determined using multireference configuration interaction wave functions. Three symmetry equivalent minima and saddle points, all with  $C_s$  symmetry, were shown to exist on the ground state potential energy surface. The  $C_s$  symmetry of the ground state and the saddle point are manifestations of the static Jahn-Teller effect. Determination of the minimum energy conical intersection of the  $1,2^2A$  states, which has  $C_{3v}$  symmetry, enabled description of this effect. The ground electronic state of the neutral was also determined. Harmonic frequencies were established for all determined critical points on the neutral and the cationic potential energy surfaces, as was the spin-orbit interaction coupling of the  ${}^2E$  state at the minimum energy crossing. Also determined was a coupled quasi diabatic representation of the  $1,2^2A$  states of the cation using the fully quadratic vibronic coupling approximation.

The coupled quasi diabatic representation of the  $1,2^2A$  states,  $\mathbf{H}^d$ , was used, in the context of KDC vibronic coupling theory, to simulate the threshold region of

the photoionization spectrum of propyne at the relativistic (that is, including spin-orbit coupling) and nonrelativistic (that is, excluding the spin-orbit interaction) levels. The relativistic analysis predicts an 18.7 (13.2)  $\text{cm}^{-1}$  splitting of the  ${}^2E_{3/2}$  –  ${}^2E_{1/2}$  states a 36 (57) percent Ham reduction of the spin-orbit coupling in the absence of the Jahn-Teller effect. These results are in reasonable accord with the experimental results of XBRLLN, given parenthetically. However, the cross-sections for producing  $\text{C}_3\text{H}_4^+({}^2E_{3/2}, v^+ = 0)$  and  $\text{C}_3\text{H}_4^+({}^2E_{1/2}, v^+ = 0)$  by ionizing propyne, which are equal by symmetry in the nonrelativistic limit, are calculated to be equal when the spin-orbit interaction is included. This result is attributed to the large, greater than  $327 \text{ cm}^{-1}$ , separation of these levels in the nonrelativistic approximation from potential perturbers, which could modify the nonrelativistic absorption cross-sections through intensity borrowing. This result is at odds with the published conclusion of XBRLLN that the cross section ratio is  $({}^2E_{1/2}, v^+ = 0)/({}^2E_{3/2}, v^+ = 0) = 4:1$ . However, discussions with Cheuk Ng, based on a preprint of this work, have determined that that conclusion of XBRLLN is incorrect and that the predicted 1-1 ratio is quite reasonable.

Finally, we have considered the lowest vibronic levels in the photoionization spectrum reported by HLWC. Our analysis suggests the possibility of additional hot-bands in that spectrum, a detailed study which will be the subject of a future report.

- **ASSOCIATED CONTENT**

- **S – Supporting Information**

Construction of  $\text{H}^{\text{d-}}$  in more detail. This material is available free of charge via the Internet at <http://pubs.acs.org>.

- **AUTHOR INFORMATION**

- **Corresponding Author**

\*Phone: 410-516-4663. E-mail: [yarkony@jhu.edu](mailto:yarkony@jhu.edu) (D.R.Y.); [smarque3@jhu.edu](mailto:smarque3@jhu.edu) (S.M.); [jdillon5@jhu.edu](mailto:jdillon5@jhu.edu) (J.D.).

- **Notes**

The authors declare no competing financial interest.

- **ACKNOWLEDGMENTS**

This work was supported by Department of Energy, Basic Energy Sciences grant DE-FG02-91ER1489 to D.R.Y.

Illuminating conversations with C. Y. Ng are gratefully acknowledged.



## REFERENCES

- (1) Fitzgerald, F.; Decomposition of Methyl Acetylene *Nature(London)* **1960**, *186*, 386-387.
- (2) Go, J.; Cronin, T. J.; Perry, D. S.; A free-jet infrared double resonance study of the threshold region of IVR. The  $\nu_6$ ,  $\nu_1 + \nu_6$ , and  $2\nu_1$  bands of propyne. *Chem. Phys.* **1993**, *175*, 127-145.
- (3) Gambogi, J. E.; Kerstel, E. R. T.; Lehmann, K. K.; Scoles, G.; Eigenstate resolved infrared/infrared double resonance spectroscopy of the  $3\nu_1$  overtone band of 1-propyne: Intramolecular vibrational energy redistribution into a Coriolis-coupled bath. *J. Chem. Phys.* **1994**, *100*, 2612-2622.
- (4) Alnama, K.; Boyé-Péronne, S.; Douin, S.; Fabrizio Innocenti, J. O. R.; Roche, A.-L.; Shafizadeh, N.; Zuin, L.; Gauyacq, D.; Photolysis of allene and propyne in the 7–30 eV region probed by the visible fluorescence of their fragments. *J. Chem. Phys.* **2007**, *126*, 044304
- (5) Baker, C.; Turner, D. W.; High resolution molecular photoelectron spectroscopy. III. Acetylenes and azaacetylenes. *Proc. R. Soc. London A* **1968**, 19-37.
- (6) Ensslin, W.; Bock, H.; Becker, G.; Photoelectron spectra and molecular properties. XXX.  $\pi$ -Interactions in silyl- and methyl-substitute acetylenes. *J. Am. Chem. Soc.* **1974**, *96*, 2757-2762.
- (7) Ho, G. H.; Lin, M. S.; Wang, Y. L.; Chang, T. W.; Photoabsorption and photoionization of propyne. *J. Chem. Phys.* **1998**, *109*, 5868-5879.
- (8) Shieh, J.-l.; Chang, J.-l.; Wu, J.-C.; Li, R.; Mebel, A. M.; Handy, N. C.; Chen, Y.-T.; Rydberg states of propyne at 6.8–10.5 eV studied by two-photon ionization spectroscopy and theoretical calculation. *J. Chem. Phys.* **2000**, *112*, 7384-7393.

- (9) Matsui, H.; Zhu, Y.-F.; Grant, E. R.; High-resolution non-resonant two-photon threshold photoionization of propyne. *Laser Chem.* **1996**, *16*, 161.
- (10) Xing, X.; Bahng, M.-K.; Reed, B.; Lam, C. S.; Lau, K.-C.; Ng, C. Y.; Rovibrationally selected and resolved pulsed field ionization-photoelectron study of propyne: Ionization energy and spin-orbit interaction in propyne cation. *J. Chem. Phys.* **2008**, *128*, 094311.
- (11) Jahn, H. A.; Teller, E.; Stability of Polyatomic Molecules in Degenerate Electronic States. I. Orbital Degeneracy. *Proc. R. Soc. London A* **1937**, *161*, 220-235.
- (12) Kramers, H.; *Proc. Acad. Sci. Amsterdam* **1930**, *33*, 959.
- (13) Pratt, S. T.; Dehmer, P. M.; Dehmer, J. L.; Zero-kinetic-energy photoelectron spectroscopy from the  $a\ 1\text{Au}$  state of acetylene: Renner-Teller interactions in the trans-bending vibration of  $\text{C}_2\text{H}_2$ . *J. Chem. Phys.* **1993**, *99*, 6233-6244.
- (14) Ham, F. S.; Dynamical Jahn-Teller Effect in Paramagnetic Resonance Spectra: Orbital Reduction Factors and Partial Quenching of Spin-Orbit Interaction. *Phys. Rev.* **1965**, *138*, A1727-A1740.
- (15) Köppel, H.; Domcke, W.; Cederbaum, L. S.; Multimode Molecular Dynamics Beyond the Born-Oppenheimer Approximation. *Adv. Chem. Phys.* **1984**, *57*, 59-246.
- (16) Köppel, H.; Domcke, W.; Cederbaum, L. S. In *Conical Intersections*; Domcke, W., Yarkony, D. R., Köppel, H., Eds.; World Scientific: New Jersey, 2004; Vol. 15, pp 323-368.
- (17) Ichino, T.; Gianola, A. J.; Lineberger, W. C.; Stanton, J. F.; Nonadiabatic Effects in the photoelectron spectrum of the pyrazolide-d<sub>3</sub> anion.

- Three-state interactions in the pyrazolyl d3 radical. *J. Chem. Phys.* **2006**, *125*, 084312.
- (18) Schuurman, M. S.; Yarkony, D. R. In *Conical Intersections: Theory, Computation and Experiment*; Domcke, W., Yarkony, D. R., Köppel, H., Eds.; World Scientific: Singapore, 2010.
- (19) Bethe, H. A.; Salpeter, E. E. *Quantum Mechanics of One and Two Electron Atoms*; Plenum/Rosetta: New York, 1977.
- (20) Schuurman, M. S.; Weinberg, D. E.; Yarkony, D. R.; On the determination of photoelectron spectra in molecules with conical intersections and spin-orbit coupling. The vibronic spectrum of CH<sub>3</sub>S. *J. Chem. Phys.* **2007**, *127*, 104309.
- (21) Mishra, S.; Poluyanov, L. V.; Domcke, W.; Spin-orbit vibronic coupling in 3 $\pi$  states of linear triatomic molecules. *J. Chem. Phys.* **2007**, *126*, 134312.
- (22) Mishra, S.; Vallet, V.; Domcke, W.; Calculation of the vibronic structure of the X 2 $\pi$  photoelectron spectra of XCN, X = F, Cl, and Br. *J. Chem. Phys.* **2006**, *124*, 044317.
- (23) Mondal, P.; Opalka, D.; Poluyanov, L. V.; Domcke, W.; Jahn-Teller and spin-orbit coupling effects in transition-metal trifluorides. *Chem. Phys.* **2011**, *387*, 56-65.
- (24) Mondal, P.; Opalka, D.; Poluyanov, L. V.; Domcke, W.; Ab initio study of dynamical X E Jahn-Teller and spin-orbit coupling effects in the transition-metal trifluorides TiF<sub>3</sub>, CrF<sub>3</sub>, and NiF<sub>3</sub>. *J. Chem. Phys.* **2012**, *136*, 084308.
- (25) Opalka, D.; Segado, M.; Poluyanov, L. V.; Domcke, W.; Relativistic Jahn-Teller effect in tetrahedral systems. *Phys. Rev. A* **2010**, *81*, 042501.

- (26) Poluyanov, L. V.; Domcke, W.; The relativistic Renner-Teller effect revisited. *Chem Phys.* **2004**, 301, 111-127.
- (27) Poluyanov, L. V.; Domcke, W.; Two-channel semiclassical s-matrix for the E X E Jahn-Teller problem including spin-orbit coupling. *Chem. Phys.* **2006**, 322, 349-353.
- (28) Poluyanov, L. V.; Domcke, W.; Relativistic ext Jahn-Teller effect in tetrahedral systems. *J. Chem. Phys.* **2008**, 129, 224102.
- (29) Poluyanov, L. V.; Domcke, W.; The E-3 X E, E-4 and E-5 X E Jahn-Teller Hamiltonians of trigonal systems. *Chem. Phys.* **2008**, 352, 125-134.
- (30) Poluyanov, L. V.; Domcke, W.; Relativistic T X T and T X E Jahn-Teller coupling in tetrahedral systems. *Chem. Phys.* **2010**, 374, 86-93.
- (31) Poluyanov, L. V.; Domcke, W.; Jahn-Teller, pseudo-Jahn-Teller, and spin-orbit coupling Hamiltonian of the D electron in an octahedral environment. *J. Chem. Phys.* **2012**, 137, 114101.
- (32) Poluyanov, L. V.; Domcke, W.; Jahn-Teller and pseudo-Jahn-Teller couplings in D-2d systems. *Chem. Phys.* **2012**, 407, 1-8.
- (33) Poluyanov, L. V.; Mishra, S.; Domcke, W.; Quasiclassical theory of the dynamical E X E Jahn-Teller effect including spin-orbit interaction. *Mol. Phys.* **2007**, 105, 1471-1485.
- (34) Poluyanov, L. V.; Mishra, S.; Domcke, W.; Quasistationary upper-well states of E X E Jahn-Teller systems with spin-orbit coupling. *Chem. Phys.* **2007**, 332, 243-248.
- (35) Barckholtz, T. A.; Miller, T. A.; Quantitative insights about molecules exhibiting Jahn-Teller and related effects. *Int. Rev. Phys. Chem.* **1998**, 17, 435-524.

- (36) Schuurman, M. S.; Young, R. A.; Yarkony, D. R.; On the Multimode Quadratic Vibronic Coupling Problem: An Open-ended Solution Using a Parallel Lanczos Algorithm. *Chem. Phys.* **2008**, *347*, 57-64.
- (37) Schuurman, M. S.; Yarkony, D. R.; A Method to Reduce the Size of the Vibronic Basis Employed in the Simulation of Spectra Using the Multimode Vibronic Coupling Approximation. *J. Chem. Phys.* **2008**, *128*, 044119.
- (38) Dillon, J. J.; Yarkony, D. R.; Schuurman, M. S.; On the Construction of Quasi Diabatic State Representations of Bound Adiabatic State Potential Energy Surfaces Coupled by Conical Intersections. Incorporation of Higher Order Terms. *J. Chem. Phys.* **2011**, *134*, 044101.
- (39) Doktorov, E. V.; Malkin, I. A.; Man'ko, V. I.; Dynamical Symmetry of Vibronic Transitions in Polyatomic Molecules and the Franck-Condon Principle. *J. Mol. Spec.* **1975**, *56*, 1-20.
- (40) Doktorov, E. V.; Malkin, I. A.; Man'ko, V. I.; Dynamical Symmetry of Vibronic Transitions in Polyatomic Molecules and the Franck-Condon Principle. *J. Mol. Spec.* **1977**, *64*, 302-326.
- (41) Hazra, A.; Nooijen, M.; Derivation and Efficient Implementation of a Recursion Formula to Calculate Harmonic Franck-Condon Factors for Polyatomic Molecules. *Int. J. Quantum Chem.* **2003**, *95*, 643-657.
- (42) Kupka, H.; Cribb, P. H.; Multidimensional Franck-Condon integrals and Duschinsky mixing effects. *J. Chem. Phys.* **1986**, *85*, 1303-1315.
- (43) Langhoff, S. R.; Kern, C. W.; In *Modern Theoretical Chemistry*; Schaefer, H. F., Ed.; Plenum: New York, 1977; Vol.4, p 381.

- (44) Mead, C. A.; The noncrossing rule for electronic potential energy surfaces. The role of time reversal invariance. *J. Chem. Phys.* **1979**, *70*, 2276-2285.
- (45) Truhlar, D. G.; Mead, C. A.; Brandt, M. A.; Time-Reversal Invariance, Representations for Scattering wavefunctions, symmetry of scattering matrices and differential cross-sections. *Adv. Chem. Phys.* **1975**, *33*, 295.
- (46) McWeeny, R.; On the Origin of Spin-Hamiltonian Parameters. *J. Chem. Phys.* **1965**, *42*, 1717-1725.
- (47) Furlani, T. R.; King, H. F.; Theory of spin-orbit coupling. Application to singlet-triplet interaction in the trimethylene biradical. *J. Chem. Phys.* **1985**, *82*, 5577-5583.
- (48) Lischka, H.; Shepard, R.; Shavitt, I.; Pitzer, R.; Dallos, M.; Müller, T.; P.G.Szalay; Brown, F. B.; Alhrichs, R.; Böhm, H. J.; Chang, A.; Comeau, D. C.; Gdanitz, R.; Dachsels, H.; Erhard, C.; Ernzerhof, M.; Höchtel, P.; Irle, S.; Kedziora, G.; Kovar, T.; Parasuk, V.; Pepper, M.; Scharf, P.; Schiffer, H.; Schindler, M.; Schüler, M.; Zhao, J.-G. A Program. COLUMBUS, An ab initio Electronic Structure Program, 2003.
- (49) Dallos, M.; Lischka, H.; Szalay, P.; Shepard, R.; Yarkony, D. R.; The analytic evaluation of nonadiabatic coupling terms at the MR-CI level II; Determination of minima on the crossing seam. *J. Chem. Phys.* **2004**, *120*, 7330-7339.
- (50) Lischka, H.; Dallos, M.; Szalay, P.; Yarkony, D. R.; Shepard, R.; The analytic evaluation of nonadiabatic coupling terms at the MR-CI level I: Formalism. *J. Chem. Phys.* **2004**, *120*, 7322-7329.

- (51) Yarkony, D. R.; On the Use of the Breit-Pauli Approximation of Evaluating Line Strengths for Spin-Forbidden Transitions, II The Symbolic Matrix Element Method. *J. Chem. Phys.* **1986**, *84*, 2075-2078.
- (52) Liu, B.; Yoshimine, M.; The alchemy configuration interaction method. I. The symbolic matrix method for determining elements of matrix operators. *J. Chem. Phys.* **1981**, *74*, 612-616.
- (53) Top, Z. H.; Baer, M.; Adiabatic and diabatic representations for atom-diatom collisions: treatment of the three-dimensional case. *Chem. Phys.* **1976**, *15*, 49-57.
- (54) Mead, C. A.; Truhlar, D. G.; Conditions for the definition of a strictly diabatic basis. *J. Chem. Phys.* **1982**, *77*, 6090-6098.
- (55) Einfeld, W.; Viel, A.; Higher order (A+E)xe Pseudo Jahn-Teller coupling. *J. Chem. Phys.* **2005**, *122*, 204317.
- (56) Viel, A.; Einfeld, W.; Effects of higher order Jahn-Teller coupling on the nuclear dynamics. *J. Chem. Phys.* **2004**, *120*, 4603-4613.
- (57) Papas, B. N.; Schuurman, M. S.; Yarkony, D. R.; The Simulated Photoelectron Spectrum of 1-propynide. *J. Chem. Phys.* **2009**, *130*, 064306.
- (58) Papas, B. N.; Schuurman, M. S.; Yarkony, D. R.; Determining quasi diabatic coupled electronic state Hamiltonians using derivative couplings. A normal equations based method. *J. Chem. Phys.* **2008**, *129*, 124104.
- (59) Hamermesh, M.; *Group Theory and Its Application to Physical Problems*; Addison-Wesley: Reading, MA, 1962.

# Sara Anne Marquez

---

smarque3@jhu.edu  
2300 N. Calvert St. Apt 401, Baltimore, MD 21218

## EDUCATION

---

**Doctor of Philosophy** Chemistry – Johns Hopkins University (Baltimore, MD) (2018)

Thesis: *Experimental and Theoretical Explorations of Anion Photoelectron Spectroscopy and Photoionization*

Advisor: Dr. Kit Bowen

**Masters of Arts** - Johns Hopkins University (Baltimore, MD) (2013)

**Major:** Chemistry

**Bachelors of Science** - Montana State University (Bozeman, MT) (2011)

**Major:** Chemistry, Biochemistry

**Honors:** Cum Laude

**Bachelors of Science** - Montana State University (Bozeman, MT) (2011)

**Major:** Chemical Engineering

**Honors:** Cum Laude

## RESEARCH EXPERIENCE

---

**Graduate Research Assistant**, Johns Hopkins University, Baltimore, MD (8/2015-Present)

- ◆ Devised experiments to isolate and investigate size-selected negative ion molecules and clusters in the gas phase
- ◆ Established a thorough knowledge of ion beams and high-vacuum systems in a team environment by designing, fabricating, and rebuilding a time-of-flight (TOF) mass spectrometer, a magnetic bottle photoelectron spectrometer, and cryostat coupled to an electrospray ionization source
- ◆ Developed a LabVIEW program to collect mass spectrometry data and photoelectron spectroscopy data through the interface with an oscilloscope
- ◆ Fabricate customized vacuum equipment using a lathe, mill, band saw, and drill press

**Graduate Research Assistant**, Johns Hopkins University, Baltimore, MD (8/2013-8/2015)

- ◆ Developed computer programs to simulate experiments
- ◆ Created computer scripts to transpose data to spreadsheets and perform calculations
- ◆ Used various computer programs to analyze experimental data
- ◆ Initiated, manage, and execute all data collection and analysis of my project
- ◆ Constructed 3D plots and other plots to clearly depict analyzed data for colleagues and superiors
- ◆ Independently planned future experiments based on analyzed results
- ◆ Performed research in Nuclear Magnetic Resonance (NMR) Spectroscopy
- ◆ Manipulated nuclear spins using strong magnetic fields created by superconducting magnets
- ◆ Teaching Assistant to the Physical Chemistry Instrumentation Laboratory II & III courses during the Spring and Fall semesters
  - ◇ Included assessment of lab performances, grading all lab work, providing feedback to student, calibration of instruments, and simple instrument repairs when necessary

**Graduate Research Assistant**, Johns Hopkins University, Baltimore, MD (8/2011-7/2013)

- ◆ Devised computational experiments
- ◆ Independently analyzed all data collected using scripts written in various languages
- ◆ Performed research in theoretical chemical physics
- ◆ Used Lagrange multipliers and Newton-Raphson methods to identify conical intersections and construct potential energy surfaces



- ◆ Simulated both relativistic and non-relativistic spectrum for publication
- ◆ Teaching Assistant to the Physical Chemistry Instrumentation Laboratory II & III courses and Introductory Chemistry Laboratory II course during Spring and Fall semesters
  - ◇ Included assessments of student lab performances, graded all lab work, provided feedback to students, and instructed my own sub-section

**Undergraduate Research Assistant**, Montana State University (Bozeman, MT) (5/2010-7/2011)

- ◆ Performed research in surface dynamics as well as photochemistry
- ◆ Performed surface analysis on samples retrieved from the Materials International Space Station Experiment 6 (MISSE 6)
- ◆ Managed and analyzed all data using spreadsheets
- ◆ Exposed polymer films to conditions found in Low Earth Orbit (LEO)
- ◆ Obtained clean room training

---

### TEACHING EXPERIENCE

**Johns Hopkins University** (Baltimore, MD)

Spring 2015	Teaching Assistant for Physical Chemistry Laboratory II
Fall 2014	Teaching Assistant for Physical Chemistry Laboratory III
Spring 2014	Teaching Assistant for Physical Chemistry Laboratory II
Fall 2013	Teaching Assistant for Physical Chemistry Laboratory III
Spring 2013	Teaching Assistant for Physical Chemistry Laboratory II
Fall 2012	Teaching Assistant for Physical Chemistry Laboratory III
Spring 2012	Teaching Assistant for Introductory Chemistry Laboratory II
Fall 2011	Teaching Assistant for Physical Chemistry Laboratory III

---

### PUBLICATIONS & POSTERS

- ◆ Single Spin Inversion by J-driven Selective Cross Polarization with Application to measurement of 1H-1H couplings. Poster session presented at: 56th Experimental Nuclear Magnetic Resonance Conference, Pacific Grove, CA, April 2015.
- ◆ "On the Photoionization Spectrum of Propyne: A Fully Ab Initio Simulation of the Low-Energy Spectrum Including the Jahn-Teller Effect and the Spin-Orbit Interaction." *The Journal of Physical Chemistry A* 117 (2013): 12002-2010.
- ◆ "Atomic Oxygen Effects on POSS Polyimides in Low Earth Orbit." *ACS Applied Material & Interfaces* 4 (2012): 492-502.
- ◆ "Oxygen-Atom Reactivity with Polyimide and POSS-Polyimide Surfaces." Poster session presented at: 241st ACS National Meeting, Anaheim, CA, March 2011.

---

### COMPUTER AND LANGUAGE SKILLS

- ◆ Microsoft Office Suite (Word, Excel, PowerPoint, Outlook), Endnote, Mathematica, GAMESS, Jmol, COLUMBUS, Fortran, Perl, Microsoft Visual Studio, Solid Works, SIMION, Bash, Adobe Illustrator, C++, C#, MatLab, and LabView